sid.inpe.br/mtc-m21d/2021/08.02.15.09-TDI

METHOD FOR MAPPING DEFORESTATION IN CERRADO BASED ON DEEP LEARNING USING LANDSAT AND SENTINEL IMAGE TIME SERIES

Bruno Menini Matosak

Master's Dissertation of the Graduate Course in Remote Sensing, guided by Drs. Leila Maria Garcia Fonseca, and Marcos Adami, approved in July 29, 2021.

URL of the original document:
<http://urlib.net/8JMKD3MGP3W34T/4578TM2>

INPE
São José dos Campos
2021

PUBLISHED BY:

Instituto Nacional de Pesquisas Espaciais - INPE
Coordenação de Ensino, Pesquisa e Extensão (COEPE)
Divisão de Biblioteca (DIBIB)
CEP 12.227-010
São José dos Campos - SP - Brasil
Tel.:(012) 3208-6923/7348
E-mail: pubtc@inpe.br

sid.inpe.br/mtc-m21d/2021/08.02.15.09-TDI

METHOD FOR MAPPING DEFORESTATION IN CERRADO BASED ON DEEP LEARNING USING LANDSAT AND SENTINEL IMAGE TIME SERIES

Bruno Menini Matosak

Master's Dissertation of the Graduate Course in Remote Sensing, guided by Drs. Leila Maria Garcia Fonseca, and Marcos Adami, approved in July 29, 2021.

URL of the original document:
<http://urlib.net/8JMKD3MGP3W34T/4578TM2>

INPE
São José dos Campos
2021

Cataloging in Publication Data

Matosak, Bruno Menini.

M428m Method for mapping deforestation in Cerrado based on deep learning using Landsat and Sentinel image time series / Bruno Menini Matosak. – São José dos Campos : INPE, 2021.

xxii + 83 p. ; (sid.inpe.br/mtc-m21d/2021/08.02.15.09-TDI)

Dissertation (Master in Remote Sensing) – Instituto Nacional de Pesquisas Espaciais, São José dos Campos, 2021.

Guiding : Drs. Leila Maria Garcia Fonseca, and Marcos Adami.

1. Deforestation. 2. Time series. 3. Change detection. 4. LSTM. 5. U-Net. I.Title.

CDU 504.122:528.8

MINISTÉRIO DA CIÊNCIA, TECNOLOGIA E INOVAÇÕES

INSTITUTO NACIONAL DE PESQUISAS ESPACIAIS

Serviço de Pós-Graduação - SEPGR

DEFESA FINAL DE DISSERTAÇÃO DE BRUNO MENINI MATOSAK
BANCA Nº 196/2021, REG 739747/2019

No dia 29 de julho de 2021, as 08h00min, por teleconferência, o(a) aluno(a) mencionado(a) acima defendeu seu trabalho final (apresentação oral seguida de arguição) perante uma Banca Examinadora, cujos membros estão listados abaixo. O(A) aluno(a) foi APROVADO(A) pela Banca Examinadora, por unanimidade, em cumprimento ao requisito exigido para obtenção do Título de Mestre em Sensoriamento Remoto. O trabalho precisa da incorporação das correções sugeridas pela Banca Examinadora e revisão final pelo(s) orientador(es).

Título: "METHOD FOR MAPPING DEFORESTATION IN CERRADO BASED ON DEEP LEARNING USING LANDSAT AND SENTINEL IMAGE TIME SERIES"

Membros da banca:

Dr. Thales Sehn Körting - Presidente - INPE
Dra. Leila Maria Garcia Fonseca - Orientadora - INPE
Dr. Marcos Adami - Orientador - INPE
Dr. Sidnei João Siqueira Sant'Anna Membro Interno - INPE
Dr. Raul Queiroz Feitosa - Membro Externo - PUC/RIO

Documento assinado eletronicamente por **Marcos Adami**, **Pesquisador**, em 03/08/2021, às 08:16 (horário oficial de Brasília), com fundamento no § 3º do art. 4º do Decreto nº 10.543, de 13 de novembro de 2020.

Documento assinado eletronicamente por **Thales Sehn Korting**, **Pesquisador**, em 03/08/2021, às 08:13 (horário oficial de Brasília), com fundamento no § 3º do art. 4º do Decreto nº 10.543, de 13 de novembro de 2020.

Documento assinado eletronicamente por **Leila Maria Garcia Fonseca**, **Tecnologista**, em 03/08/2021, às 08:48 (horário oficial de Brasília), com fundamento no § 3º do art. 4º do Decreto nº 10.543, de 13 de novembro de 2020.

Documento assinado eletronicamente por **Sidnei João Siqueira SantAnna**, **Tecnologista**, em 03/08/2021, às 16:08 (horário oficial de Brasília), com fundamento no § 3º do art. 4º do Decreto nº 10.543, de 13 de novembro de 2020.

Documento assinado eletronicamente por **Raul Queiroz Feitosa (E)**, **Usuário Externo**, em 03/08/2021, às 18:06 (horário oficial de Brasília), com fundamento no § 3º do art. 4º do Decreto nº 10.543, de 13 de novembro de 2020.

A autenticidade deste documento pode ser conferida no site http://sei.mctic.gov.br/verifica.html, informando o código verificador **7920904** e o código CRC **EE9A58DE**.

"Não fosse meu despoder, por azias e reumatismo, aí eu ia. Eu guiava o senhor até tudo. Lhe mostrar os altos claros das Almas: rio despenha de lá, num afã, espuma próspero, gruge; cada cachoeira, só tombos. O cio da tigre preta na Serra do Tatu – já ouviu o senhor gargaragem de onça? A garoa rebrilhante da dos-Confins, madrugada quando o céu embranquece – neblim que chamam de xererém. Quem me ensinou a apreciar essas as belezas sem dono foi Diadorim... A da-Raizama, onde até os pássaros calculam o giro da lua – se diz – e canguçu monstra pisa em volta. Lua de com ela se cunhar dinheiro. Quando o senhor sonhar, sonhe com aquilo. Cheiro de campos com flores, forte, em abril: a ciganinha, roxa, e a nhiíca e a escova, amarelinhas...".

João Guimarães Rosa
in *"Grande Sertão: Veredas"*, 1956

To my loved ones.

ACKNOWLEDGEMENTS

I would like to thank my family: my parents for their support in all steps until we reached this stage and also my sister and nieces, for being an emotional anchor for all the times things started to lose sense.

I would also like to thank my previous advisors: Selma, for teaching me that hard work is very welcome to research, as well as patience, and also Nilcilene, for giving me opportunities, being kind and patient, and advising me so wisely not only regarding research.

I would also like to thank my current advisors, Leila and Adami, that besides all the help and support provided in the making of a master's dissertation, believed in my potential, listened to my ideas, and helped me become a better researcher. I am really grateful to both of them.

Also I am really grateful for all the amazing friends that I met at INPE, who carried this dream with me, contributing directly or indirectly to this work, especially Raian, Evandro, Hugo, Sabrina, Edson, Tati, Ana, and Cândida.

I would like to thank the National Council for Scientific and Technological Development (CNPq), the Coordination for the Improvement of Higher Education Personnel (CAPES) - Finance Code 001, and Environmental Monitoring of the Brazilian Biomes project (Amazonia Fund), managed by *Fundação de Apoio para Projetos de Pesquisa de Ciência e Tecnologia Espacial* (FUNCATE), for the financial support in many different phases of my research to produce this work.

Lastly, I would like to thank God.

ABSTRACT

Cerrado is the second largest biome in Brazil, covering about 2 million km^2. It is considered a global biodiversity hotspot and it is essential for Brazil's water security. This biome has experienced land use and land cover changes at high rates in the last three decades so that 50.51% of its natural vegetation has been already removed. Thus, it is crucial to provide technologies capable to control and monitor the Cerrado vegetation suppression in order to undertake the environmental conservation policies. Therefore, this work aims to develop a methodology to detect deforestation in Cerrado, combining two deep learning architectures, LSTM and U-Net, and using Landsat and Sentinel image time series. In the proposed method, the LSTM evaluates the time series in relation to the time axis to create a deforestation probability map, which is spatially analyzed by the U-Net algorithm alongside the terrain slope to finally produce deforestation maps. To evaluate the potential of the proposed methodology two study areas were defined, one in Bahia and other in Mato Grosso. Besides, three strategies for training samples selection and also two time series based on Landsat and Sentinel imagery were considered. The resultant maps were validated through a stratified random sampling approach, using Sentinel time series as reference. The results achieved high accuracy metrics, peaking at an overall accuracy and F1-Score of $99.81\% \pm 0.21$ and 0.8795 ± 0.1180, respectively, for the Bahia study area and Sentinel time series. The validation tests showed that the proposed methodology can provide accurate Cerrado deforestation maps, and besides it has potential to be scalable to the entire Cerrado biome, after implementing some improvements.

Keywords: Deforestation. Time Series. Change Detection. LSTM. U-Net. Landsat. Sentinel.

MÉTODO PARA O MAPEAMENTO DE DESMATAMENTO NO CERRADO BASEADO EM DEEP LEARNING USANDO SÉRIES TEMPORAIS DE IMAGENS LANDSAT E SENTINEL

RESUMO

O Cerrado é o segundo maior bioma do Brasil, cobrindo uma área de aproximadamente 2 milhões km^2. Ele é considerado um *hotspot* de biodiversidade global e é essencial para a segurança hídrica do Brasil. Este bioma vem apresentando altas taxas de mudanças de uso e cobertura do solo nas últimas três décadas, de forma que $50,51\%$ de toda a sua vegetação natural já foi removida. Deste modo, é crucial que tecnologias capazes de controlar e monitorar a supressão da vegetação natural do Cerrado sejam desenvolvidas, para que políticas de conservação ambiental sejam empreendidas. Portanto, este trabalho visa o desenvolvimento de uma metodologia para a detecção de desmatamento no Cerrado, combinando duas arquiteturas de *deep learning*, LSTM e U-Net, e usando séries temporais de imagens Landsat e Sentinel. Nos métodos propostos, a LSTM avalia as séries temporais no eixo do tempo para criar um mapa de probabilidade de desmatamento, o qual é analisado pela U-Net junto à declividade do terreno para finalmente produzir o mapa de desmatamento. Para avaliar o potencial da metodologia proposta, duas áreas de estudos foram definidas, uma na Bahia e outra no Mato Grosso. Ademais, três estratégias para a seleção de amostras de treinamento foram consideradas, além de séries temporais diferentes baseadas em imagens Landsat e Sentinel. Os mapas obtidos foram validados através de uma amostragem aleatória estratificada, usando séries temporais Sentinel como referência. Os resultados apresentaram altas métricas de precisão, alcançando os valores máximos para a precisão global e *F1-Score* de $99,81\% \pm 0.21$ e $0,880 \pm 0,118$, respectivamente, para a área de estudos da Bahia e usando séries temporais Sentinel. A validação dos resultados mostrou que a metodologia proposta pode ser usada para gerar mapas de desmatamento para o Cerrado com uma alta precisão, e que além disso tem o potencial de ser escalonada para todo o Cerrado, após a implementação de algumas melhorias.

Palavras-chave: Desmatamento. Séries Temporais. Detecção de Mudanças. LSTM. U-Net. Landsat. Sentinel.

LIST OF FIGURES

Page

LIST OF TABLES

Page

LIST OF ABBREVIATIONS

AE	–	Autoencoders
ARD	–	Analysis Ready Data
AWFI	–	Wide Field Imager Camera
BIP	–	Brazilian Investment Plan
BDC	–	Brazil Data Cube
CNN	–	Convolutional Neural Networks
DETER	–	Near Real-time Deforestation Detection System
DL	–	Deep Learning
ESA	–	European Space Agency
EVI	–	Enhanced Vegetation Index
FIP	–	Forest Investment Program
QGIS	–	Quantum Geographic Information System
GIZ	–	German Corporation for International Cooperation
GMES	–	Global Monitoring for Environment and Security
INPE	–	National Institute for Space Research
KfW	–	Credit Institute for Reconstruction
LDCM	–	Landsat Data Continuity Mission
LSTM	–	Long-Short Term Memory
LULC	–	Land Use and Land Cover
MCTI	–	Brazilian Ministry of Science, Technology and Innovation
ML	–	Machine Learning
MMA	–	Ministry of the Environment
MODIS	–	Moderate Resolution Imaging Spectroradiometer
MSI	–	MultiSpectral Instrument
MUX	–	Regular Multispectral Camera
NASA	–	National Aeronautics and Space Administration
NDVI	–	Normalized Difference Vegetation Index
NIR	–	Near Infrared
OLI	–	Operational Land Imager
PRODES	–	Satellite Deforestation Monitoring Project
PROBIO	–	Conservation and Sustainable Use of Brazilian Biological Diversity Project
REDD+	–	Reducing Emissions from Deforestation and Forest Degradation
RNN	–	Recurrent Neural Networks
RS	–	Remote Sensing
SIAD	–	Integrated System of Deforestation Alerts
SRTM	–	Shuttle Radar Topography Mission
SWIR	–	Short Wave Infrared
TIRS	–	Thermal Infrared Sensor
TOA	–	Top of Atmosphere
UNFCCC	–	United Nations Framework Convention on Climate Change
USGS	–	United States Geological Survey

CONTENTS

1 INTRODUCTION

The Cerrado is the second largest biome within the Brazilian territory, with an area of approximately 2 million km^2. Also known as Brazilian Savanna, this biome composes 23% of the national territory, and covers areas of 11 states and the Federal District. With more than 4,800 endemic species of plants and vertebrate animals, it is a global hotspot for biodiversity conservation, as it is under severe human-induced threats (STRASSBURG et al., 2017; MITTERMEIER et al., 2011). Besides, the Cerrado biome preservation is also crucial for the country's water security due to the presence of headwaters and springs of important rivers, like the Tocantins-Araguaia, São Francisco, and Paraná (IBGE, 2021; ANA, 2018).

Cerrado presents high degradation rates since the decade of 1960, in spite of its large species diversity and importance for water supply (STRASSBURG et al., 2017; RADA, 2013). The conversion of Cerrado vegetation to anthropic areas occurs at high rates and 50.51% of its natural vegetation has been changed mainly into agriculture and pasture (ROCHA et al., 2012; SCARAMUZZA et al., 2017; INPE, 2020). Projections indicate that 31% to 34% of the remaining area will be affected until the year of 2050 (SOARES-FILHO et al., 2016). This projection also adverts that 480 species of endemic plants are likely to be extinct, resulting in profound consequences to the local fauna and flora (STRASSBURG et al., 2017).

Studies have shown that it is possible to increase agriculture production in Cerrado through agricultural intensification and sustainable practices, among other actions to protect the remaining natural vegetation (SPERA, 2017; SANO et al., 2019). These practices could be encouraged by public environment conservation policies, but to correctly direct them it is necessary to monitor the Cerrado native vegetation conversion to understand the land occupation dynamic in this region (SANO et al., 2019).

Attempts to monitor deforestation and forest degradation in the Cerrado are relatively recent, unlike the Amazon that began in 1988 (MAURANO et al., 2019b; BRITO et al., 2018). Some initiatives started to monitor vegetation in the decade of 2000, with the Conservation and Sustainable Use of Brazilian Biological Diversity Project (PROBIO) creating a mapping of Cerrado's vegetation cover (SANO et al., 2008), along with deforestation alerts created by the Integrated System of Deforestation Alerts (SIAD) (FERREIRA et al., 2007).

Cerrado deforestation maps were produced between 2010-2013 and 2013-2015 by the National Institute for Space Research (INPE), which were the basis for submitting

a request for payments by avoided emissions. The production of this database received financial support from the Ministry of Science, Technology, Innovation and Communications (MCTIC), Ministry of the Environment (MMA) and the World Bank, in addition to the German institutions Credit Institute for Reconstruction (KfW) and German Corporation for International Cooperation (GIZ) (MAURANO et al., 2019a). In 2016 Brazil submitted the request to the United Nations Framework Convention on Climate Change (UNFCCC) as a first action for the biome in the implementation of its REDD+ policies (MMA, 2018). Based on this submission, MCTIC had approved the project "Development of Forest Fire Prevention Systems Vegetation Cover Monitoring in the Brazilian Cerrado" by the World Bank (MCTI, 2021; MMA, 2021a). This project, called FIP Monitoring, is part of the Brazilian Investment Plan (BIP) under the Forest Investment Program (FIP), which includes 6 other projects (MMA, 2021b). With support of FIP Monitoring, INPE started to produce yearly deforestation maps for Cerrado through the Satellite Deforestation Monitoring Project (PRODES) and Near Real-time Deforestation Detection System (DETER) systems in 2016 (BRITO et al., 2018; INPE, 2021a). Figure 1.1 presents the yearly deforestation rates from 2001 to 2020.

Figure 1.1 - Yearly deforestation of primary vegetation in Cerrado.

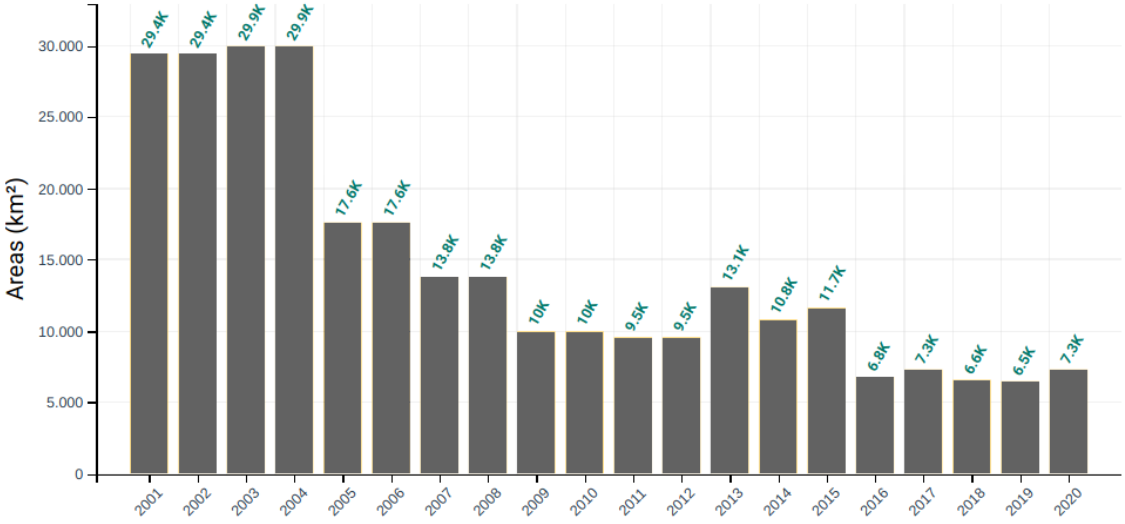

SOURCE: TerraBrasilis (2020).

PRODES aims to detect deforestation to calculate the annual deforested area increment, as well as its annual rates (SHIMABUKURO et al., 2012; BRITO et al., 2018). The PRODES methodology has been applied to Amazon and Cerrado since 1988 and

2016, respectively. This methodology is based on visual interpretation of Landsat imagery to detect deforestation areas in Cerrado, with an accuracy of 93.17%±0.89% for the year 2018 (PARENTE et al., 2021).

The PRODES methodology employs many trained human analysts to produce deforestation maps, which increases the project's cost. Besides, the analysts can represent a source of subjectivity in the detection process, although they have been trained to suppress this from the final product (BRITO et al., 2018; LUNETTA et al., 1991). Therefore, the development of automatic methods for deforestation detection can reduce the amount of specialists in the image interpretation, the subjectivity, and consequently, the project's cost (MA et al., 2019; BALL et al., 2017).

The Cerrado biome contains highly complex gradients of natural vegetation with important differences in herbaceous, woody, and forest layers, and it is also highly seasonal (FERREIRA et al., 2003). These factors make the detection of Land Use and Land Cover (LULC) changes in Cerrado a challenge (SANO et al., 2010; MÜLLER et al., 2015; REYNOLDS et al., 2016). In complex environments, such as Cerrado, state-of-the-art Remote Sensing (RS) procedures used to automate mapping often have been based on Deep Learning (DL) (MARETTO et al., 2020; MA et al., 2019; PARENTE et al., 2019; PETROVSKA et al., 2020; LI; HSU, 2020). The study of RS time series using DL has shown prominent results (INTERDONATO et al., 2019; XU et al., 2020b; DUTTA et al., 2020). Then, classification methods based on time series and DL techniques, such as the LSTM, take advantage of this temporal information to discriminate different classes (ZENG et al., 2020; RUSSWURM; KÖRNER, 2020).

Taquary (2019) proposed a classification method to detect deforestation in the Brazilian Cerrado by combining two different DL architectures: the Long-Short Term Memory (LSTM) (HOCHREITER; SCHMIDHUBER, 1997; GRAVES et al., 2013) and the U-Net (RONNEBERGER et al., 2015), regarding the time and spatial domains. The author used Planet images to compose a series of monthly mosaics for 1.5 year with spatial resolution of $3m$. Using such imagery for systematic Cerrado monitoring have many implications, such as the huge amount of data and the costs to acquire high spatial resolution images. Taken into account these barriers, current detection projects are driven to use medium spatial resolution images ($20m$ to $30m$) taken from Landsat and Sentinel platforms, which are cost-free and present good temporal resolution of 16 days and 5 days, respectively (BRITO et al., 2018; INPE, 2020; MAPBIOMAS, 2021). Besides, Sentinel and Landsat images can be integrated in a Data Cube in order to increase the temporal resolution.

In the development of change detection methods in a complex environment, such as Cerrado, it is important to consider the spatial patterns analysis (texture, shape, reflectance, etc.) and temporal patterns. In this analysis, the objects' features extracted from satellite images are used to discriminate classes taking into account the pixel information as well as its neighborhood (PARENTE et al., 2019; TORRES et al., 2020). Besides, to make the problem simpler, classification methods can create hierarchical levels of representation to handle the information in different scales (LECUN et al., 2015). All these points can improve the classification methods considerably, especially for DL methods based on fully convolutional networks.

Within this context, the main objective of this study is to develop a method to detect deforestation in the Cerrado biome based on the combination of two Deep Learning architectures, LSTM and U-Net, and time series generated from Landsat and Sentinel imagery. The hybrid classification based on LSTM and U-NET can produce deforestation maps faster than end-to-end DL architectures, which analyze time and spatial patterns at the same time, such as the ConvLSTM method (SHI et al., 2015; MARTINEZ et al., 2021). Moreover, the time and spatial analysis performed in two steps allows the analysis based on more contextual information extracted from larger neighborhood areas, which can provide better classification results. The Cerrado deforestation method proposed in this work is an adaptation of Taquary's method. Differently, the proposed method included topography data as auxiliary data and used free Landsat and Sentinel image time series instead of Planet high spatial resolution images. Besides, PRODES data was used as reference to generate training samples through three different approaches.

To perform this work, the following tasks will be implemented:

a) Creation of training samples based on existing data from PRODES;

b) Detection of Cerrado deforestation using DL methods LSTM and U-Net for two Cerrado areas;

c) Deforestation map evaluation, considering 3 different situations regarding the training samples acquired in space and time for each area to be mapped;

d) Maps accuracy assessment to evaluate the results.

2 THEORETICAL FOUNDATIONS

2.1 The Cerrado biome

The Brazilian Cerrado is the second largest biome in South America, with approximately 2 million km^2, corresponding to 23.9% of the country's territory (IBGE, 2021). Figure 2.1 shows its localization and ecoregions, within portions of the states of Maranhão, Piauí, Tocantins, Bahia, Mato Grosso, Goiás, Minas Gerais, Mato Grosso do Sul, São Paulo and Paraná, as well as the Distrito Federal. The majority of the biome is located in the Brazilian Highlands, between the latitudes of 3° and 22° South and between the longitudes of 36° and 65° West. The most present climate type is the Tropical Savanna Climate, according to the Köppen Climate Classification (ALBUQUERQUE; SILVA, 2008).

Figure 2.1 - The Cerrado Biome and its ecoregions in Brazil.

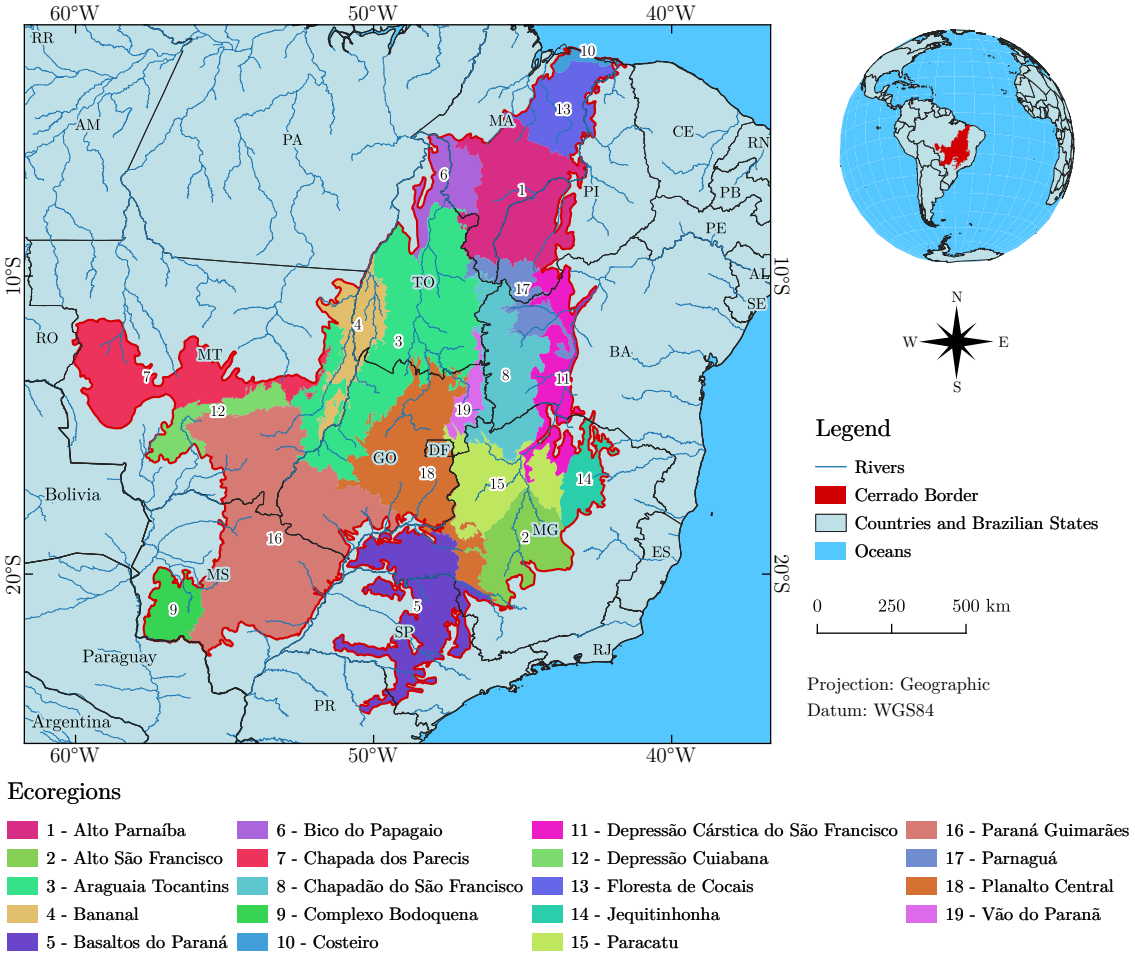

SOURCE: Adapted from IBGE (2021) and Sano et al. (2019).

Its large dimensions allow for a varied distribution of endemic species, in conditions that interactions among them are critical to long-term survival. The biome size also makes possible the existence of regions, where the ecosystems differ in terrestrial and aquatic components, setting apart ecoregions. In total, the biome can be divided into 19 distinct regions according to biophysical characteristics (Figure 2.1) that highlights Cerrado's environmental heterogeneity (SANO et al., 2019; STRASSBURG et al., 2017).

The native flora contains heterogeneous physiognomies that range from semi-arid to swamps, containing many different species adapted for such environments. One of the most adopted physiognomies definitions is described by Ribeiro and Walter (2008) (Figure 2.2), based on the vegetation form (structure, dominant growth forms, and possible stationary changes), environment aspects (edaphic factors) and floristic composition. This physiognomies classification has 14 main classes that can be grouped into 3 main formations: Forest, Savanna and Grassland.

Figure 2.2 - Physiognomies found in the Cerrado.

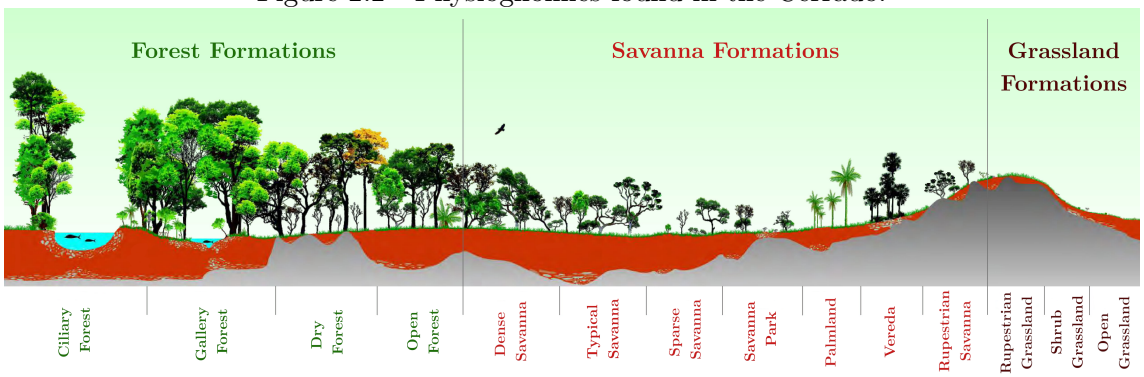

SOURCE: Adapted from EMBRAPA (2021).

Considering optical sensors, the 3 main formations present different spectral signatures, which change according to the dry and wet seasons, with a clear separation in the red spectral region ($600nm$ to $700nm$), for example. These differences can be identified in satellite optical images, but the differentiation becomes harder as one tries to map the vegetation types with more details since the physiognomies present nearly identical spectral responses, depending on the spectral interval (FERREIRA et al., 2003). Discrimination between some Cerrado vegetation types can be difficult to make even in the field, considering that several Cerrado vegetation covers do not

present evident transitions between them (RIBEIRO; WALTER, 2008; BENDINI et al., 2020; NEVES et al., 2020).

Sano et al. (2010) reported difficulties in separating areas predominantly composed of shrubs and forests, and also between cultivated pastures and Open Grassland. Müller et al. (2015) mentioned difficulties for discriminating Grassland Formations and agriculture, and Reynolds et al. (2016) pointed out the native vegetation heterogeneity as the main cause for omission and commission errors in the Cerrado vegetation mapping.

2.1.1 Cerrado deforestation

The Cerrado biome presents a late drastic transformation. Since the decade of 1960 the biome experienced a rapid conversion of its native vegetation into anthropized areas. Recent occupation at high deforestation rates was the main cause for huge amounts of native vegetation loss, implying a big impact on biodiversity (STRASSBURG et al., 2017). Going ahead, we consider deforestation as the complete removal of native vegetation, caused by human activities that aim to change the LULC.

As for 2020, 50.51% of the biome's area was already covered by some anthropic activity (Figure 2.3), an increment of 4.38% since the previous decade. The biome is currently seriously threatened by changes in vegetation cover, whose extremely high rate in recent decades was even higher than that recorded in the Amazon itself. Less than 50% of the total area is native vegetation (around 1 million km^2), compared to 82% in the Amazon (INPE, 2020).

Figure 2.3 - Cerrado's natural and anthropic vegetation map, in 2020.

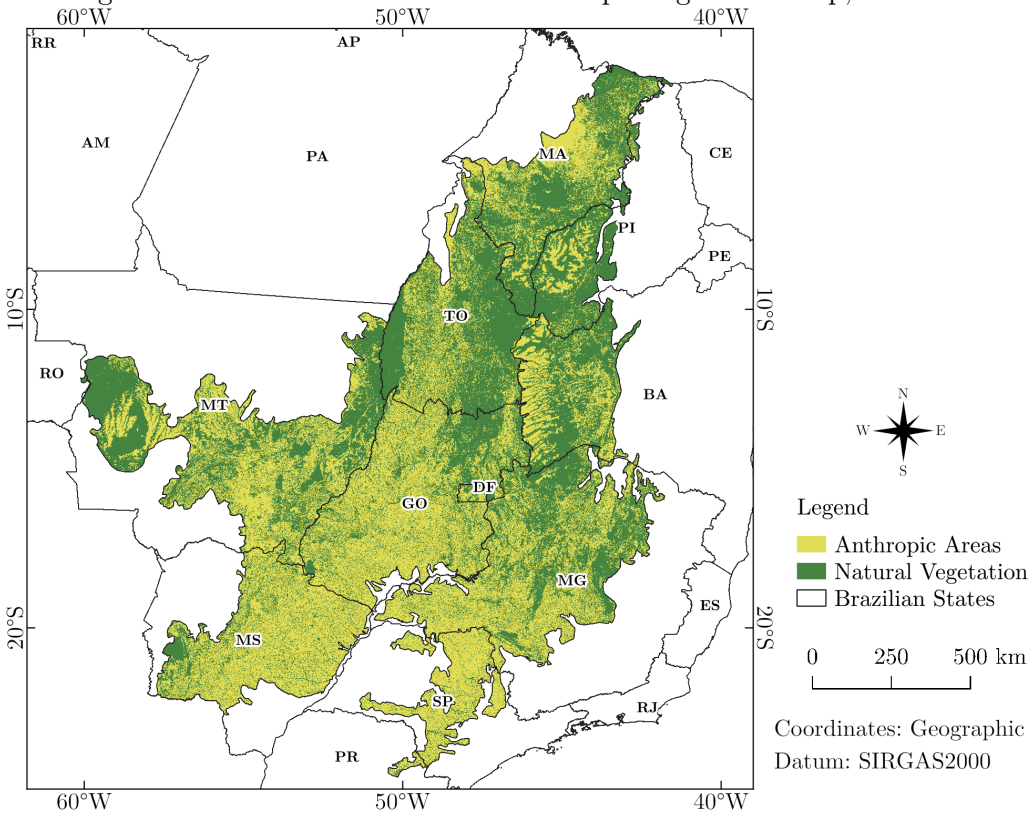

SOURCE: Adapted from INPE (2020) and IBGE (2021).

Given the Cerrado's dimension, different drivers act pushing the boundaries of agriculture. Espírito-Santo et al. (2016) evaluated the north of Minas Gerais, between 2000 and 2015, showing a decrease in coal production areas (associated with deforestation) and an increase in cultivated pastures and soy areas. This deforestation found was attributed to the expansion of the road network. On the other hand, Garcia and Ballester (2016) evaluated the region defined by the river Guariroba watershed in Mato Grosso, between 1975 and 2011. They observed a high rate of conversion from native vegetation to cultivated pastures, and pointed out higher scale opportunities as reason for such change.

Despite the different drivers for Cerrado deforestation, some of them are common in the most regions of this biome. Rocha et al. (2012) reported that most of the native vegetation conversion tends to occur in areas with dense vegetation (favorable climate and soil conditions) and flat terrains (suitable for mechanized farming).

2.1.2 PRODES Cerrado

Considering the importance to monitor the Cerrado vegetation, some initiatives to map Cerrado LULC have been performed, which include MapBiomas (MAPBIOMAS, 2021), Probio (SANO et al., 2010), TerraClass Cerrado (SCARAMUZZA et al., 2017) and PRODES Cerrado (INPE, 2020; FONSECA et al., 2021). INPE estimates deforestation rates in the Brazilian Amazon biome since 1988, through the PRODES project, on an annual basis (INPE, 2021b). This project has been used together with DETER, playing an important role in the reduction of deforestation rates in the Brazilian Amazon in the early 2000s (BOUCHER et al., 2013). PRODES and DETER methodologies were adapted, in order to be applied to the Cerrado biome, generating a very consistent temporal series of natural vegetation suppression since 2018 (FONSECA et al., 2021).

The PRODES methodology follows the steps illustrated in Figure 2.4, to estimate the annual deforestation rate for a given year. The mapping process starts with the selection of Landsat and CBERS images, during the dry season, which are downloaded and stored in the project's database. After the images download, they are imported by the analysts and used to create colored compositions, applying histogram stretching, contrast enhancement and cloud detection algorithms in order to enhance and prepare them for visual interpretation. The following step is the interpretation of images, when data is created and edited by trained analysts that visually interpret the images in order to detect deforestation. The next step is to audit data that was created, when deforestation polygons are revised and homogenized. In case they are not approved, they return to the interpretation phase, but if approved, they are sent to the next step, which is data processing. In the data processing step, the deforestation data is used in topological analysis in order to guarantee the quality of deforestation polygons, which then are used to compute the total deforested area during the analyzed period. The last step of the PRODES methodology is the creation and publishing of reports, made by using the total area computed to calculate the deforestation increment rate. All PRODES data is also made openly available during this step (BRITO et al., 2018).

Figure 2.4 - Methodology used in PRODES Cerrado.

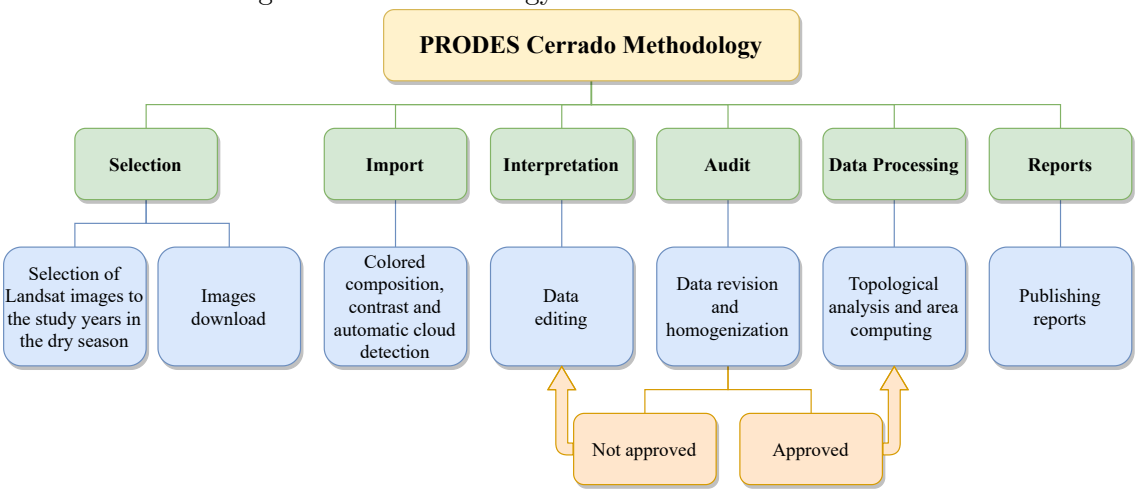

SOURCE: Brito et al. (2018).

The PRODES year, or calendar deforestation year, refers to the period that runs from 1st August of one year until 31st July of the subsequent year. For example, the rate published for the PRODES year 2018 estimates the deforestation that has occurred from 08/01/2017 to 07/31/2018. In order to produce an incremental mapping, PRODES uses a mask of exclusion, which covers areas deforested in previous years. The task of interpretation is done only on parts of the image taken in the reference year that still contains native vegetation. This mask is used to eliminate the possibility that old deforested areas are mapped again (BRITO et al., 2018; SOUZA et al., 2019). The PRODES Cerrado maps 3 classes (Table 2.1).

Table 2.1 - Interpretation classes used in PRODES Cerrado.

Class	**Description**
Anthropic	Anthropized area, where human intervention has significantly changed the natural vegetation
Water	Water bodies
Not Observed	Not observed due to cloud or cloud shadows
Natural (derived)	Natural vegetation, without major human interference (Derived from the areas not included in the previous 3 classes)

SOURCE: Brito et al. (2018).

The visual interpretation task is carried out by analysts, who consider the main

following criteria: color, tone, texture, shape and context. After producing the deforestation map, the exclusion mask is revised and audited for possible errors. A report about the results is elaborated and published with the data in `http://terrabrasilis.dpi.inpe.br` (BRITO et al., 2018; INPE, 2020; TERRABRASILIS, 2020).

2.2 Optical remote sensing time series

The first Landsat satellite was launched on 23 July 1972, which is considered an important milestone in orbital RS (BELWARD; SKØIEN, 2015). This satellite obtained images from the Earth's surface periodically, what allowed the creation of time series of RS images. Following the Landsat example, many initiatives from different countries aimed to place in orbit satellites that are also able to generate time series (Figure 2.5) (KUENZER et al., 2015).

Figure 2.5 - History of orbital earth observation programs between 1970 and 2019.

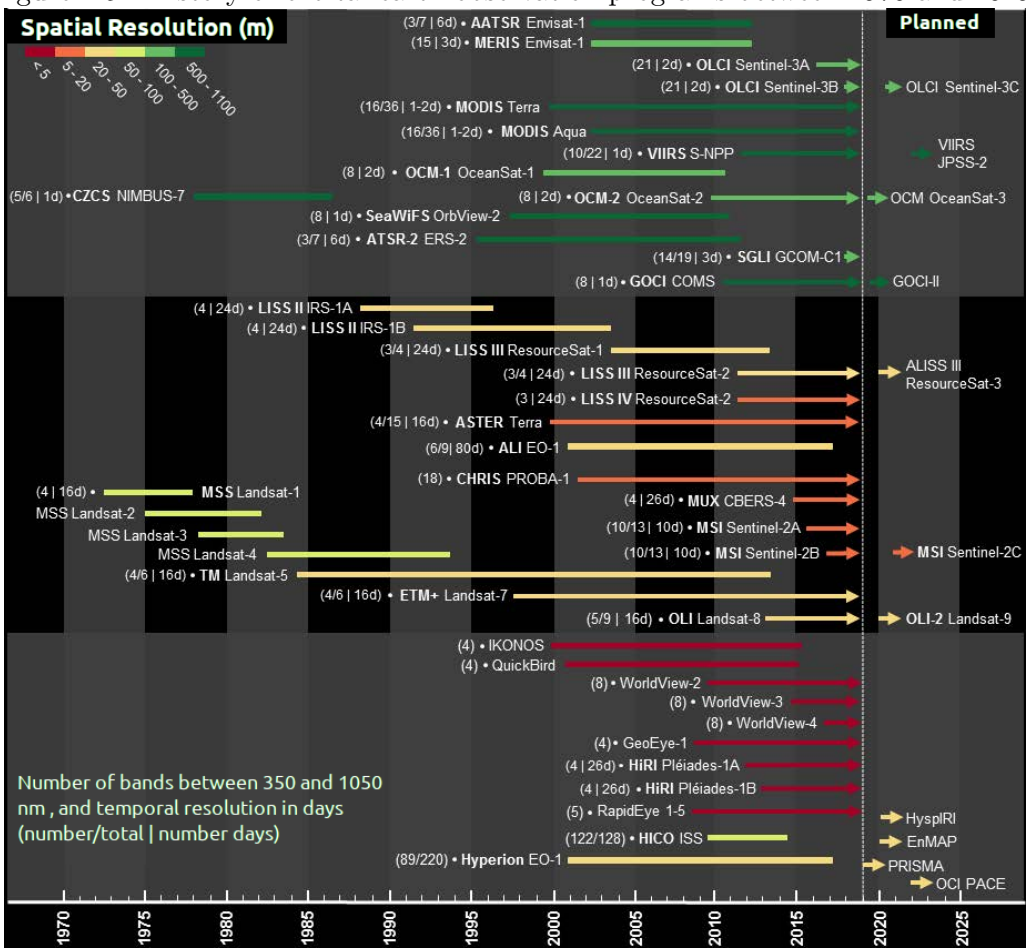

SOURCE: Barbosa et al. (2019).

A time series of RS images is created when organizing satellite images for the same region according to their order in time. In this context, the radiometric evolution of a pixel can be analyzed through time. Thus permitting the delineation of regions that undergo the same radiometric evolutions (PETITJEAN et al., 2012). These observations contain information that cannot be accessed through single-date analysis, like tendency and periodicity (EHLERS, 2009).

RS image time series provide information to study LULC change through time. In the case of vegetation, for example, phenology stages impact the spectral response, like budbreak, leaf out and leaf senescence of forest. These phenology stages can be associated with the radiometric evolution of the time series, and therefore be detected by time series based methodologies. This detection cannot be done using single date observations (BENDINI et al., 2020; ZENG et al., 2020).

The representation of phenological stages usually improves as time series more dense in the time axis are used. Studies like Bendini et al. (2019), Bendini et al. (2020), Müller et al. (2015), Matosak et al. (2020) and Ye et al. (2021) use dense time series to map vegetation, agriculture, pasture, or forest disturbances.

A problem that affects time series is data degradation due to cloud or cloud shadows, which create data gaps. When these are present, the information about the coverage is lost, resulting in missing values in the time series. Many applications rely on the series' completeness, so methods were developed in order to estimate the missing entries and fill these gaps. Simple algorithms, like cubic spline functions, interpolate missing values considering the pixel neighbors in time. Other approaches are more complex, using spatial information from similar areas on the same date to estimate the missing values, or combining machine learning techniques to achieve high accuracies for the estimation (VUOLO et al., 2017; MARUJO et al., 2020; HOU et al., 2019).

In order to create access to and easy use of time series (among other reason), the concept of data cube was created (LEWIS et al., 2017). Usually, data cube projects provide images from different sources, clipped to a fixed extent, with pixels from different dates exactly on the same location, which helps creating stacks to extract each pixel spectral behavior during time. In Figure 2.6, (a) is an image time series' stack, created from data cube images, followed by (b), which is the Normalized Difference Vegetation Index (NDVI) variation for a pixel. The NDVI is derived from MODIS MOD13Q1 data, in the Municipality of Mariana – MG, Brazil. One can notice a change in periodicity around 2016, when a mining dam broke, covering part

of the region with mining rejects.

Figure 2.6 - Satellite image time series.

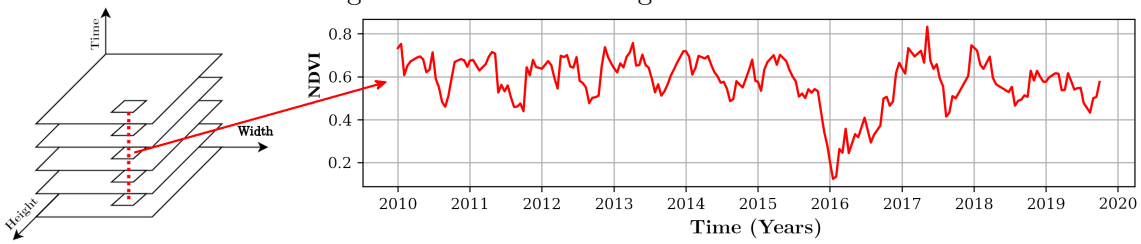

(a) Satellite image time series stack; (b) NDVI variation through time for a pixel.
SOURCE: Author's production.

2.2.1 Landsat-8 and Sentinel-2 satellites

Landsat-8

The satellite Landsat-8 was launched on 11 February 2013, as a successor of Landsat-7, both part of the Landsat Data Continuity Mission (LDCM). This project is a partnership between NASA and the United States Geological Survey (USGS) (LOVELAND; IRONS, 2016).

Landsat-8 is the 8th satellite of LDCM, the first was launched on 23 July 1972, making this project's data the longest multi-spectral time series for the Earth surface (BELWARD; SKØIEN, 2015; LOVELAND; IRONS, 2016). Landsat-8 has on-board the Operational Land Imager (OLI) and the Thermal Infrared Sensor (TIRS) cameras, and many improvements were implemented comparing to its predecessor (LOVELAND; IRONS, 2016), as follows:

- 11 imaging multi-spectral bands, with the sensors OLI and TIRS (Table 2.2);
- Improved on-board radiometric calibration, significantly improved signal-noise rate for each band and radiometric resolution improved from 8-bits to 12-bits;
- Improvement in the daily acquisition capacity, from 250 images per day to 400 images per day; and

- Enhancement in the collected images processing net, resulting in immediate processing and distribution to Landsat users.

Table 2.2 - Landsat-8: OLI and TIRS imaging bands.

Sensor	**Bands**	**Wavelength** (μm)	**Spatial Resolution** (m)
OLI	Band 1 - Coastal	0.433-0.453	30
	Band 2 - Blue	0.450-0.515	30
	Band 3 - Green	0.525-0.600	30
	Band 4 - Red	0.630-0.680	30
	Band 5 - NIR	0.845-0.885	30
	Band 6 - SWIR 1	1.560-1.660	30
	Band 7 - SWIR 2	2.100-2.300	30
	Band 8 - Panchromatic	0.500-0.680	15
	Band 9 - Cirrus	1.360-1.390	30
TIRS	Band 10 - Thermal 1	10.6-11.2	100
	Band 11 - Thermal 2	11.5-12.5	100

SOURCE: NASA (2013).

Landsat-8 operates in an heliosynchronous polar orbit, at an altitude of 705km at the Equator line. The platform was established to generate images with a temporal resolution of 16 days, with a swath of approximately 185km, following the same sequence of ground tracks defined by the WRS-2 (USGS, 2019).

Sentinel-2

Like in Landsat, Sentinel images are also available free of cost to the user. In this case, these images are obtained from a constellation of two satellites: Sentinel-2A and Sentinel-2B (ESA, 2021a). This monitoring program was created by the initiative Global Monitoring for Environment and Security (GMES), conducted by the European Union through the European Space Agency (ESA) (DRUSCH et al., 2012).

Sentinel-2A was launched on 23 June 2015 and Sentinel-2B on 7 March 2017. Both satellites are on heliosynchronous polar orbits and collect data with a swath of 290 km on Earth's surface, with a temporal resolution of 5 days at the Equator Line. The MultiSpectral Instrument (MSI) sensor on-board has 13 bands in different spectral intervals (Table 2.3) and its radiometric resolution is 12-bits (ESA, 2021a; ESA, 2021b; DRUSCH et al., 2012).

Table 2.3 - Sentinel-2A and Sentinel-2B bands configurations, from sensor MSI.

Bands	**Wavelength** (μm)	**Spatial Resolution** (m)
Band 1	0.432-0.453	60
Band 2	0.459-0.525	10
Band 3	0.541-0.577	10
Band 4	0.649-0.680	10
Band 5	0.696-0.712	20
Band 6	0.732-0.747	20
Band 7	0.771-0.791	20
Band 8	0.780-0.886	10
Band 8a	0.854-0.875	20
Band 9	0.934-0.954	60
Band 10	1.360-1.390	60
Band 11	1.566-1.658	20
Band 12	2.104-2.284	20

SOURCE: ESA (2021b).

The scientific community has utilized Sentinel-2 images in different scenarios (PAGEOT et al., 2020; BENDINI et al., 2019; ISAIENKOV et al., 2021). The advantages found in Sentinel-2, in comparison to Landsat-8, are the higher revisit time and spatial resolutions. These characteristics are responsible for more detailed information, however, potential has also been found in the combination of data from both platforms (CHASTAIN et al., 2019; MANDANICI; BITELLI, 2016).

2.2.2 Brazil Data Cube

In the context of RS, data cube projects have been important initiatives to aid the study of time series (XU et al., 2020a; BROOKE et al., 2017; NGUYEN et al., 2018; CHAVES et al., 2020). Some geoscience data cube initiatives are: the Swiss Data Cube (GIULIANI et al., 2017), the Australian Geoscience Data Cube (LEWIS et al., 2017) and the Brazil Data Cube (BDC) (FERREIRA et al., 2020b).

A data cube can be defined as a set of image time series, arranged in spatially aligned pixels (APPEL; PEBESMA, 2019). In this, each element (or image) of a data cube is composed of two spatial dimensions and one temporal dimension (FERREIRA et al., 2020b). The images are pre-processed to be Analysis Ready Data (ARD), which meet a minimum set of requirements to be used in immediate analysis without extra effort by the user (SIQUEIRA et al., 2019). In this sense, spectral ARD images are

the result of processing satellite images from their raw acquisition values to surface reflectance (GIULIANI et al., 2017).

Projects conducted by INPE have been exploiting freely available RS imagery, using cloud computing environments, big data technologies, and machine learning. One of these projects, the e-Sensing ran from 2015 to 2018 applying new methods to improve the extraction of LULC change information from big Earth Observation datasets. The BDC project was created based on the know-how acquired in the e-Sensing project and on national demands on LULC monitoring (FERREIRA et al., 2020b).

The BDC methodology to generate data cubes is illustrated in Figure 2.7. Data cubes are created using images from 4 main earth observation programs: the Landsat-8/OLI, Sentinel-2/MSI, Terra and Aqua/MODIS, and CBERS-4/MUX and AWFI (FERREIRA et al., 2020b).

Figure 2.7 - BDC data acquisition, ARD processing, and data cube generation.

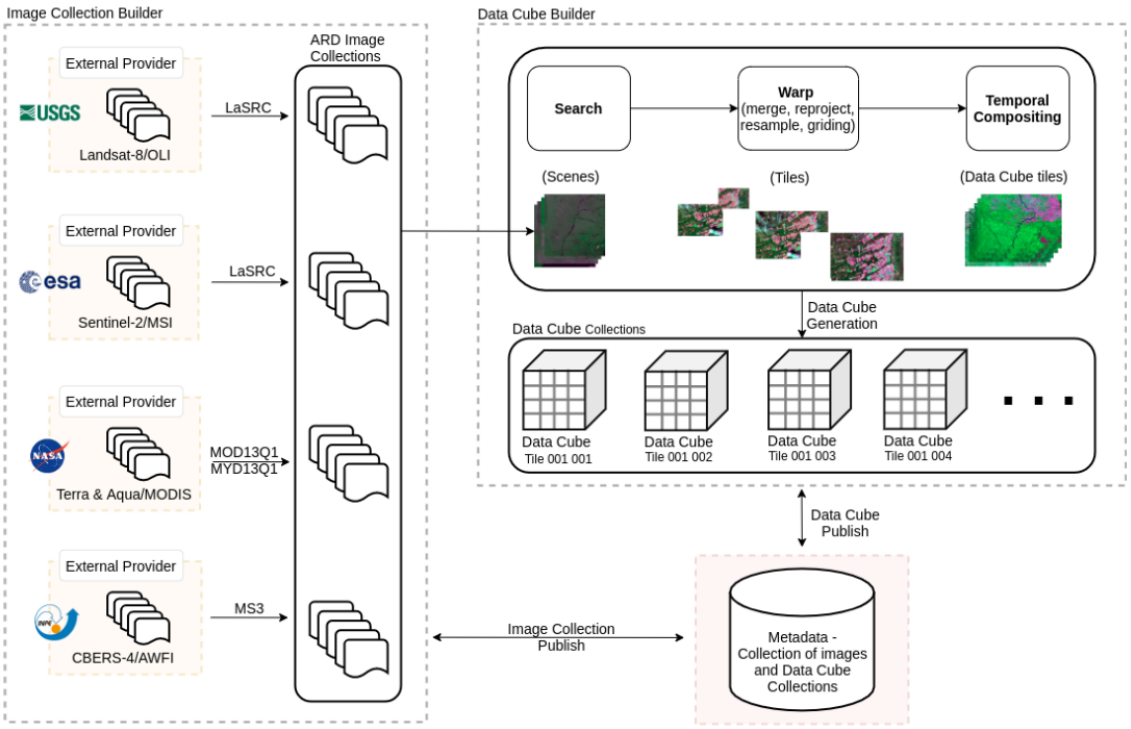

SOURCE: Ferreira et al. (2020b).

Sentinel, Landsat and CBERS images are first obtained as reflectance of Top of

Atmosphere (TOA) according to their official providers, then processed into surface reflectance. The atmospheric correction is performed by the MS3 (SILVA; ANDRADE, 2013) algorithm for CBERS-4/MUX and AWFI, and by the LaSRC (VERMOTE et al., 2016) algorithm for Sentinel-2/MSI and Landsat-8/OLI. For Terra and Aqua/MODIS, the images are already acquired as surface reflectance through the products MOD13Q1 and MYD13Q1.

A cloud and cloud shadow mask is provided for each image. The mask is produced by using the FMASK 4.2 (QIU et al., 2019) algorithm for Sentinel and Landsat, and the CMASK algorithm for CBERS. After this step, the images are used to create the data cubes.

The project publishes its cubes in their online portal[1], separated according to a specific tiling system. This system is defined by the 54° West longitude as the central reference, from which 3 different grids are generated according to the tile size: $6° \times 4°$ named BDC_LG (large), $3° \times 2°$ named BDC_MD (medium), and $1.5° \times 1°$ named BDC_SM (small). The datum used is the SIRGAS 2000 and the projection is a custom Albers equal area (FERREIRA et al., 2020b).

Despite being a project in development, the BDC has already provided data cubes to the RS scientific community, which have been used in many environmental monitoring applications (PICOLI et al., 2020; SOARES et al., 2020; MATOSAK et al., 2020; FERREIRA et al., 2020a). In Ferreira et al. (2020b) the BDC project goals and data are described, together with an example for the application of their data. In their example they used one tile of the CBERS-4 data cube to create a LULC map (Figure 2.8a). They used a DL approach to separate the classes, using the pixels spectral evolution in time (Figure 2.8b).

[1] http://brazildatacube.org/

Figure 2.8 - LULC classification made using the BDC CBERS-4 datacube.

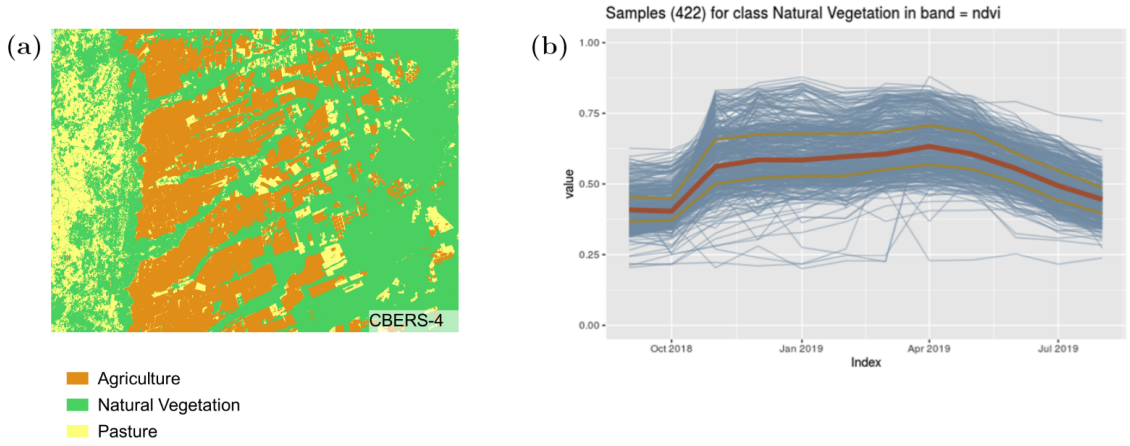

LULC map for one region in the western Bahia (a) and 422 training samples for the class "Natural Vegetation" (b).

SOURCE: Ferreira et al. (2020b).

2.3 Deep learning algorithms in remote sensing

Current DL algorithms have been widely used in different RS applications. Many DL works can be found in RS sub-areas, such as object detection, image segmentation, LULC classification, among others (SHI et al., 2020; BALL et al., 2017; MA et al., 2019).

DL algorithms are part of the Representation Learning algorithms. They can be defined as algorithms that allow the usage of raw data as input, and automatically discover the representations needed to recognize patterns or detect changes (LECUN et al., 2015).

The DL algorithms create different levels of representation, which can learn very complex functions. To find patterns in different detail scales, for example, lower layers detect the edges in an image, while higher layers learn the pattern of the amalgamation of such edges (LECUN et al., 2015). Figure 2.9 shows a DL model and the features identified by its layers, used to identify if there is a car, a person, or an animal in the image.

Figure 2.9 - Illustration of a deep learning model.

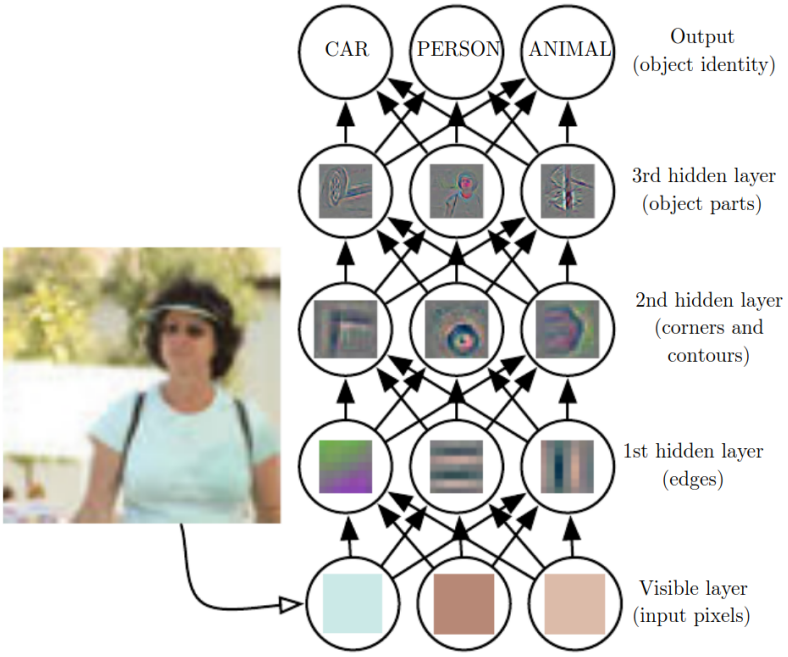

SOURCE: Goodfellow et al. (2016).

The main advantage of DL algorithms compared to other non-Representation Learning ones is their lower need of manual interference. DL algorithms can learn complex patterns from raw data and automatically find features that are highly correlated to the object of study (ALPAYDIN, 2014; LECUN et al., 2015).

DL algorithms are considered state-of-the-art methods for supervised classification procedures. As in common machine learning applications, training samples are used to adjust the DL model weights, in order to use it later in a prediction operation, i.e. applying the model to classify data. DL applications became popular because of its outstanding results, but many labeled samples are needed during the training phase to improve the classifications created by the model. The creation of numerous training samples is often impossible, due to data scarcity or high costs involved in the process, but strategies have been developed to counter act these limitations. Data augmentation, for example, is used to synthetically increase the sample quantity and diversity. In case the samples are composed of images or part of images, these can be rotated, flipped or transposed in order to create new samples (KATTENBORN et al., 2021; MA et al., 2019).

Typical neural networks DL models are based on *neurons*, which arrangements form

layers. The neurons between layers are connected through weights and bias, which during training are optimized for the classification task. The *activation function* determines if a neuron is active, if activated, the intensity of a neuron's output is determined by its weights an biases applied to the input. The weights and biases start with random values, these are adjusted during training by the *loss function* that minimize the errors when labeled samples are submitted through the model. The classification happens by transforming the input data with the model's layers.

Training a DL model is computationally expensive. The input normally has large dimensions, like image data, implying in a multitude of neurons associated with the layers that depict features and context at different scales. Usually, the model is trained with a huge amount of data that may not fit the system memory at once. To surpass this limitation, the training data is subdivided into *batches* that are sequentially fed to the model during training. The training samples are submitted to the model multiple times, called *epochs*, until the model is optimized.

The quality of training samples' labels is a factor that greatly influences a DL model. Mislabeled samples can drastically deteriorate the results obtained by a model during prediction, since the weights and biases are not correctly optimized (JIANG et al., 2017; LI et al., 2021). Another common problem related with DL training samples is the class imbalance. Difficulties in training are reported when the number of samples in one class is fewer than the others, resulting in a deterioration of the model's performance (RENDÓN et al., 2020).

Different DL algorithms have been used in the context of RS. Overall, these applications use one of the following architectures: Convolutional Neural Networks (CNN), Recurrent Neural Networks (RNN), Autoencoders (AE), Restricted Boltzmann Machines and Deep Belief Networks, and Generative Adversarial Networks (MA et al., 2019).

2.3.1 Long-Short Term Memory

RNN are a type of DL algorithm created specially to analyze correlations among different positions of a data sequence (GRAVES et al., 2013). This is possible due to the feedforward mechanism that connects the output to the input of the network, during the processing of the next element of the sequence (GOODFELLOW et al., 2016; OLAH, 2015). Figure 2.10 shows the unfolded computing graph of a feedforward RNN. In this scheme (before the equal sign), a chunk of neural network A looks at the input x_t, creating the output h_t. The feedforward RNN have a loop that pass

information from one step of the network to the next. This loop allows these RNN to be represented as multiple copies of the same network, with each one passing information to its successor. If we 'unroll' the loop, the RNN can be represented as in Figure 2.10 after the equal sign. Now, the input is x_0, x_1, ..., x_t, one for each 'copy' of the network, however each iteration of the network receives information from the previous one, resulting in h_0, h_1, ..., h_t respectively. The chain-like nature of RNN is easily used with data sequences, what makes RNN a DL architecture that works well with time series.

Figure 2.10 - Unfolded computing graph of an feedforward RNN.

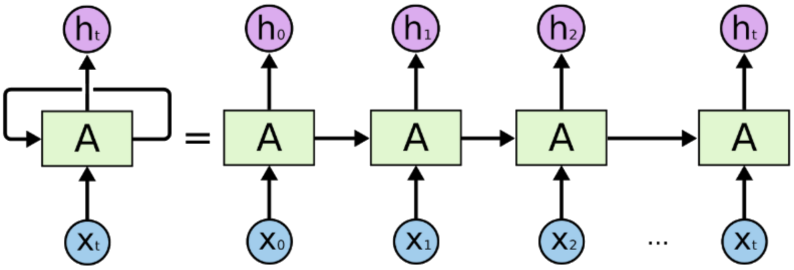

Input sequence: $x = (x_0, x_1, x_2, ..., x_t)$ and output h_t. "A" is the RNN.
SOURCE: Olah (2015).

The RNN have the form of a modules chain, composed of simple structures, like a single neural *tanh* layer inside A, for example (GOODFELLOW et al., 2016). However, this basic feedforward form presents problems during the learning process of long sequences, what makes them not suitable in the identification of long term dependencies (PASCANU et al., 2013).

The Long-Short Term Memory (LSTM) is an improvement on feedforward RNN, adapted to identify patterns in long sequences (HOCHREITER; SCHMIDHUBER, 1997; GRAVES et al., 2008). Observing the simple RNN implementation of Figure 2.11a, there is only a single *tanh* module inside the network, which uses the output of the previous iteration concatenated with its x_t value to generate an output that is directly passed to the next iteration of the RNN loop. In the LSTM (Figure 2.11b), multiple layers of neural networks are used in each module, interacting with channels responsible to regulate the flux of information through the network unfolding. The layers σ sort which information is passed forward by the model. Thus, meaningful information is kept in the 'time' axis of the sequence, while irrelevant information is

discarded, implementing a short memory of long term and selective (HOCHREITER; SCHMIDHUBER, 1997).

Figure 2.11 - Internal modules of a feedforward RNN and the LSTM.

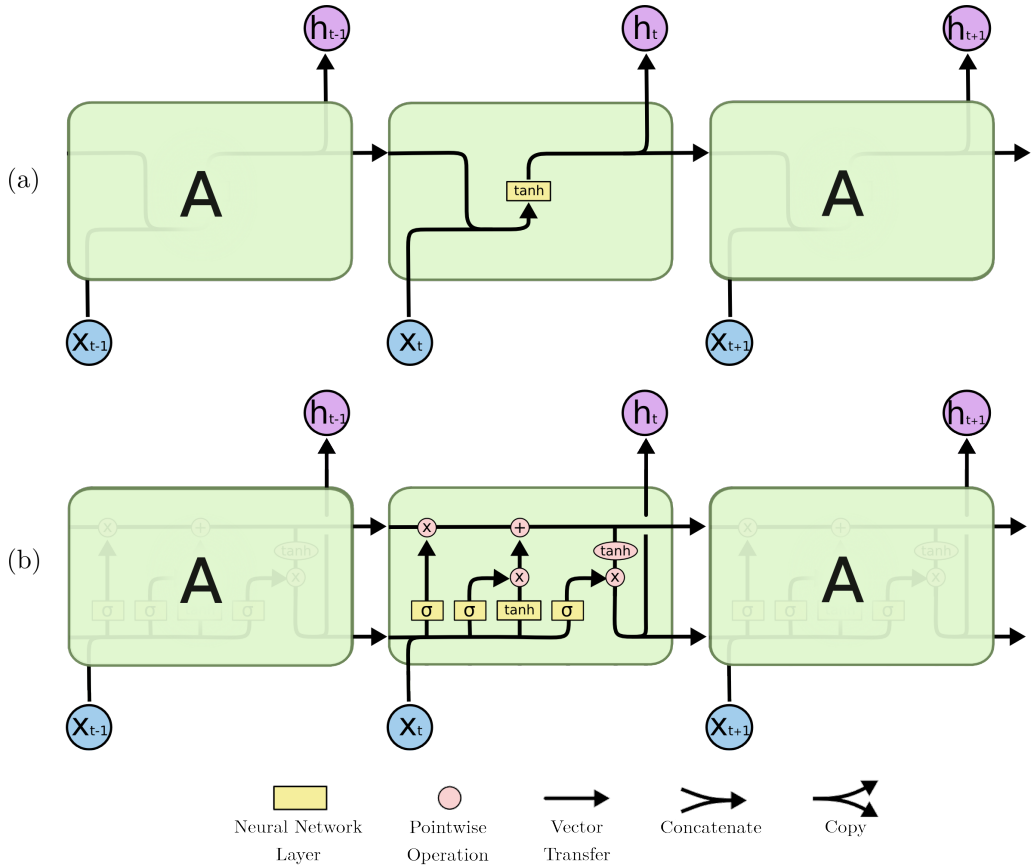

Components of a RNN feedforward module (a); Components of a LSTM module (b). SOURCE: Olah (2015).

Being an algorithm to analyze sequences, the LSTM is used in RS as a tool to study time series (PARENTE et al., 2019; TAQUARY, 2019; MATOSAK et al., 2020; CASTRO FILHO et al., 2020). In these cases, the most common strategy is to analyze the time series of each pixel separately, like the series in Figure 2.6. Each series is classified considering only its time axis, disregarding the pixel neighboring in space.

According to Tobler (1970), close entities tend to be more correlated than distant ones. When the LSTM application does not consider spatial axes, it does not take advantage of the RS data intrinsic spatial characteristics. However, there are other

DL architectures capable of using the spatial context of remote sensing data, like the U-Net.

2.3.2 U-Net

The CNN are a DL type of architecture focused on image classification (LECUN et al., 1999). Differently from RNN, they are composed of feature-extraction stages, with multiple layers containing neurons. Each stage is composed of 3 parts: a convolutional layer, a nonlinearity layer, and a pooling layer. A common CNN contains one, two, or three feature-extraction stages, followed by one or more fully-connected layers and one classifier (ZHANG et al., 2016). Many CNN architectures have been used widely in RS applications, given its outstanding results compared to less complex machine learning algorithms (KATTENBORN et al., 2021).

CNN make successive transformations in the raw data to extract relevant characteristics through sampling and convolution processes. These transformations reduce data dimensions, whilst it approximates to deeper layers to extract relevant information (TAQUARY, 2019). CNN were originally created to label images with a single class, therefore this reduction in data dimensions helps the method to eliminate not relevant information. However it also results in loss of spatial information along many layers. It is possible to make the pixel-wise classification with traditional CNN, but with reduced precision in location and context (MARMANIS et al., 2016).

To surpass this hindering aspect, alterations in the traditional CNN architecture were proposed, resulting in the U-Net (RONNEBERGER et al., 2015). This architecture is considered not only superior due to its higher spatial precision, but also for using less training samples. In the U-Net, while half of its layers reduce the data dimensions, the other half expand them, not reducing the output data dimensions. This construction aims to generate an output with dimensions of the same order as the input (RONNEBERGER et al., 2015).

In the U-Net architecture there are 4 main parts (Figure 2.12) (RONNEBERGER et al., 2015):

a) Convolution layers composed of filters arrays applied on the images, formed by neuron matrices;

b) Pooling layers to perform downsampling in the images to reduce their spatial dimensions;

c) Upsampling layers to increase images dimensions through transpose convolutions; and

d) Concatenate operations to combine the input and output of the Upsampling and Pooling layers in the same level.

Figure 2.12 - General scheme of an U-Net architecture.

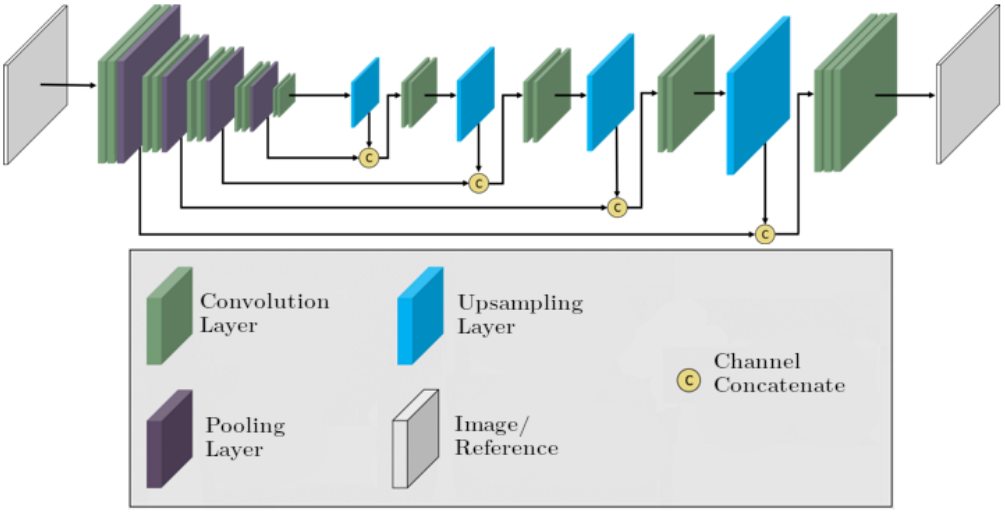

SOURCE: Li (2017).

The U-Net capacity to generate pixel-by-pixel semantic segmentation has been useful to the RS research community. Methodologies were developed to create LULC maps, clouds and cloud shadow masks, among other applications (KATTENBORN et al., 2021; MOHAJERANI et al., 2018; RAKHLIN et al., 2018; WAGNER et al., 2019; WIRATAMA et al., 2020; XU et al., 2018). Nevertheless, there is great potential to explore this algorithm, specially combining it with other methods applied to Earth Observation images.

2.4 Mapping accuracy measures

Systematic LULC mapping using satellite images and RS techniques is a challenging task. Errors can be obtained due to placing complex continuous conditions into discrete classes, or even the mapping process itself, the data used in the classification process, and also biases (FOODY, 2010). Accuracy estimation is important to provide the confidence levels to the final user (FOODY, 2010; OLOFSSON et al., 2014).

The confusion matrix is used to derive many measures that describe the map ac-

curacy, summarizing qualities or imperfections regarding specific contexts (FOODY, 2010). To create a confusion matrix, the map generated is compared to reference data, which shall be of higher quality than the data used to create the map (OLOFSSON et al., 2014). If reference data is available for the whole mapped area, a complete evaluation can be conducted. However, a complete reference is not always easy to obtain. In this case, a sampling approach can be performed by randomly selecting points over the resulting map, and acquiring reference corresponding to them. Considering a random sampling design, the number of points (n) for validation can be calculated in the following way (LOHR, 2009):

$$n = \frac{z_{\alpha/2}^2 \cdot \sigma^2 \cdot N}{e^2(N-1) + z_{\alpha/2}^2 \cdot \sigma^2} \tag{2.1}$$

where n is the sample size; $z_{\alpha/2}$ the $(1-\alpha/2)$th percentile of the normal distribution for the confidence level α; σ^2 is the variance; N is the population size (number of pixels); and e is the standard error.

2.4.1 Confusion matrix

The confusion matrix created for all the map classes provides a description of the classification accuracy. On the other hand, if the focus is on target detection, a binary confusion matrix can be constructed, which is tipically used in LULC change (FOODY, 2010), as presented in Table 2.4.

Table 2.4 - Binary Confusion Matrix model.

		Reference		
		Change	**No Change**	
Remote Sensing	**Change**	a_{11}	a_{12}	$a_{1+} = \sum a_{1j}$
	No Change	a_{21}	a_{22}	$a_{2+} = \sum a_{2j}$
		$a_{+1} = \sum a_{i1}$	$a_{+2} = \sum a_{i2}$	$n = \sum a_{ij}$

SOURCE: Foody (2010).

Usually, the *change* occurs less than *no change*, so Olofsson et al. (2014) recommend to increase the *change* sample proportion, in order to achieve accurate quality metrics. With unbalanced strata in relation to the class proportions, the authors also recommend a normalization of the resultant confusion matrix, which can be

achieved with:

$$\hat{a}_{ij} = W_i \frac{a_{ij}}{a_{i+}} \tag{2.2}$$

where $\hat{a}_{ij}$ is the term of the confusion matrix in term of area proportion, W_i is the proportion of area mapped for the class i, and i and j belong to the set {1,2} where 1 corresponds to *change* and *2* to no change. As $\hat{a}_{ij}$ is available for all confusion matrix elements, accuracy metrics derived from the confusion matrix can be estimated substituting $\hat{a}_{ij}$ for a_{ij}.

A first statistic that can be derived from the confusion matrix is the Overall Accuracy. Defined as:

$$Overall\ Accuracy = \frac{\sum a_{ii}}{n}. \tag{2.3}$$

In the Overall Accuracy assessment, the confidence interval provides a better understanding of this statistical parameter. One way to estimate this statistic is with $\pm Z_{\alpha/2}(SE_{OA})$. $Z_{\alpha/2}$ is obtained from the normal distribution, which corresponds to a determined significance level α (1.96 for a 95% significance level), and SE_{OA} is the standard error, defined as (FOODY, 2009).

$$SE_{OA} = \frac{\sqrt{a_{12} + a_{21} - (a_{12} - a_{21})^2/n}}{n} \tag{2.4}$$

In LULC change, the detection is often represented in terms of sensitivity and specificity, also known as the Producer's Accuracy (PA) for the "Change" and "No Change" classes, respectively (FOODY, 2010). They measure the proportion of the class that was correctly mapped, associated with the omission error. They are obtained by:

$$PA_{change} = \frac{a_{11}}{a_{+1}}; \tag{2.5}$$

$$PA_{no\,change} = \frac{a_{22}}{a_{+2}} \tag{2.6}$$

Likewise, there are the predicted positive and predicted negative values, which are also known as User's Accuracy (UA) for the "Change" and "No Change" classes, respectively. Associated with the commission errors, these values can be calculated as follows (FOODY, 2010):

$$UA_{change} = \frac{a_{11}}{a_{1+}}; and \tag{2.7}$$

$$UA_{no\,change} = \frac{a_{22}}{a_{2+}} \tag{2.8}$$

In order to obtain the User's Accuracy standard error (SE_{UA}), Olofsson et al. (2014) suggested the following equation:

$$SE_{UA_i} = \sqrt{\frac{UA_i(1 - UA_i)}{a_{i+} - 1}} \tag{2.9}$$

where i belong to the set {1,2}, where 1 corresponds to *change* and *2* to no change. On the other hand, the Producer's Accuracy standard error (SE_{PA}) is obtained by another means, as in the following equation:

$$SE_{PA_j} = \sqrt{\frac{1}{\hat{N}_{+j}^2}\left[\frac{N_{j+}^2 \cdot (1 - PA_j^2 \cdot UA_j(1 - UA_j))}{a_{j+} - 1} + PA_j^2 \cdot T\right]} \tag{2.10}$$

where i and j belong to the set {1,2}, where 1 corresponds to *change* and *2* to no change. The values for N are analogous to a in Table 2.4, where:

$$N_{ij} = \frac{a_{ij} \cdot tp}{n} \tag{2.11}$$

where tp is the total number of pixels in the classification. $\hat{N}_j$ and T are:

$$\hat{N}_j = \sum_{i=1}^{q} \frac{N_i}{a_i+} a_{ij} \tag{2.12}$$

$$T = \sum_{i \neq j} N_{i+}^2 \frac{a_{ij}}{a_{i+}} \left(1 - \frac{a_{ij}}{a_{i+}}\right) / (a_{i+} - 1) \tag{2.13}$$

A measure commonly used in DL classification is the F1-Score. This metric can be used to analyze the quality of classes of interest since it is calculated for a specific class. In the context of binary matrices, this value represents the harmonic mean between the Change Producer's Accuracy (Equation 2.5) and the Change User's Accuracy (Equation 2.7), also known as Precision (P) and Recall (R), respectively. The F1-Score can be obtained by:

$$F1\text{-}Score = 2\frac{P \cdot R}{P + R} \tag{2.14}$$

3 METHODOLOGY

3.1 Study areas

In this work, the evaluation tests were conducted in two main locations: (1) State of Bahia, and (2) State of Mato Grosso, as depicted in Figure 3.1.

Figure 3.1 - Study areas.

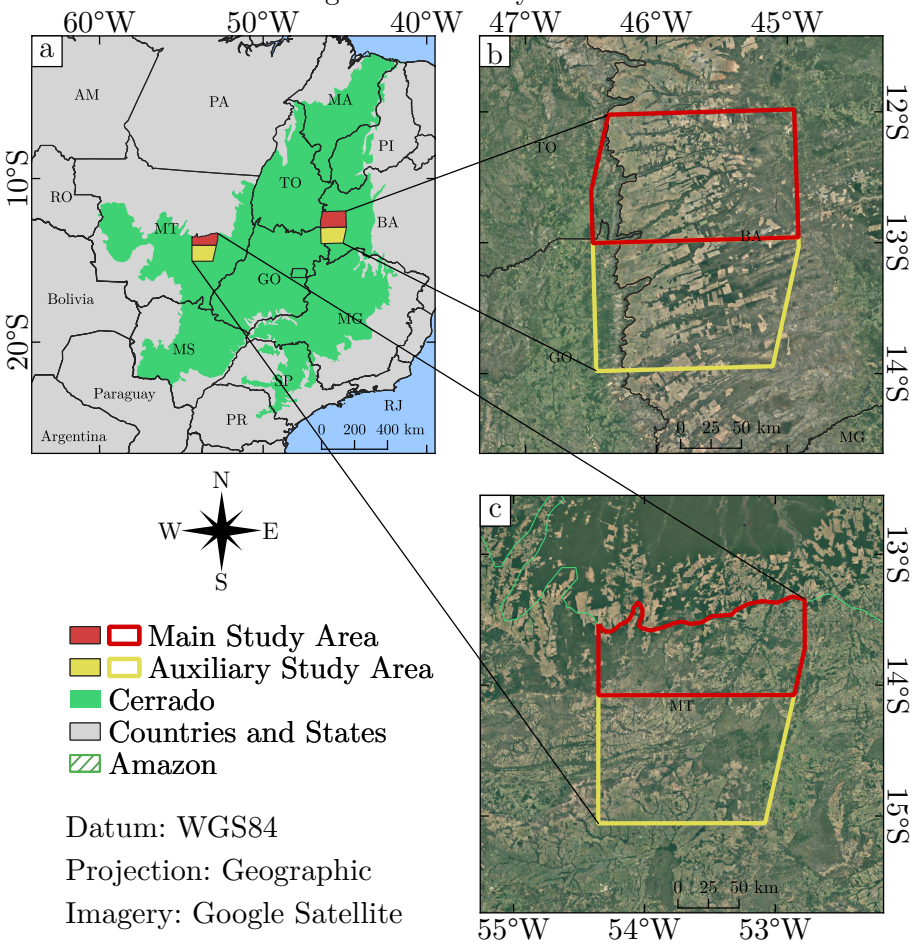

Study areas: (a) Bahia and (b) Mato Grosso.

SOURCE: Author's production.

The study areas have $35,167.910km^2$ in Bahia and $27,514.383km^2$ in Mato Grosso. Each location has two sub-areas: 'main' and 'auxiliary'. The latter is used only in the training samples creation for Approach 2, detailed in Section 3.2.

The locations were chosen to evaluate the proposed methodology in different scenar-

ios, where Bahia presents more favorable characteristics comparing to Mato Grosso. In Bahia, the study area belongs mainly to the Chapadão do São Francisco ecoregion (Figure 3.2a) and the main anthropic land occupation is agriculture, with crops in large fields due to terrain aptitude for mechanization. In Mato Grosso, the study area is situated in a transition area between Cerrado and Amazon, making it more complex and heterogeneous than in Bahia. The area in Mato Grosso also belongs to 3 ecoregions: Paraná Guimarães, Depressão Cuiabana, and Chapada dos Parecis (Figure 3.2b), granting it a higher level of patterns complexity, given its high heterogeneity. For the Mato Grosso area, agriculture and pastures are the main anthropic land occupations (MAPBIOMAS, 2021; SANO et al., 2019).

Figure 3.2 - Study areas and their ecoregions according to Sano et al. (2019).

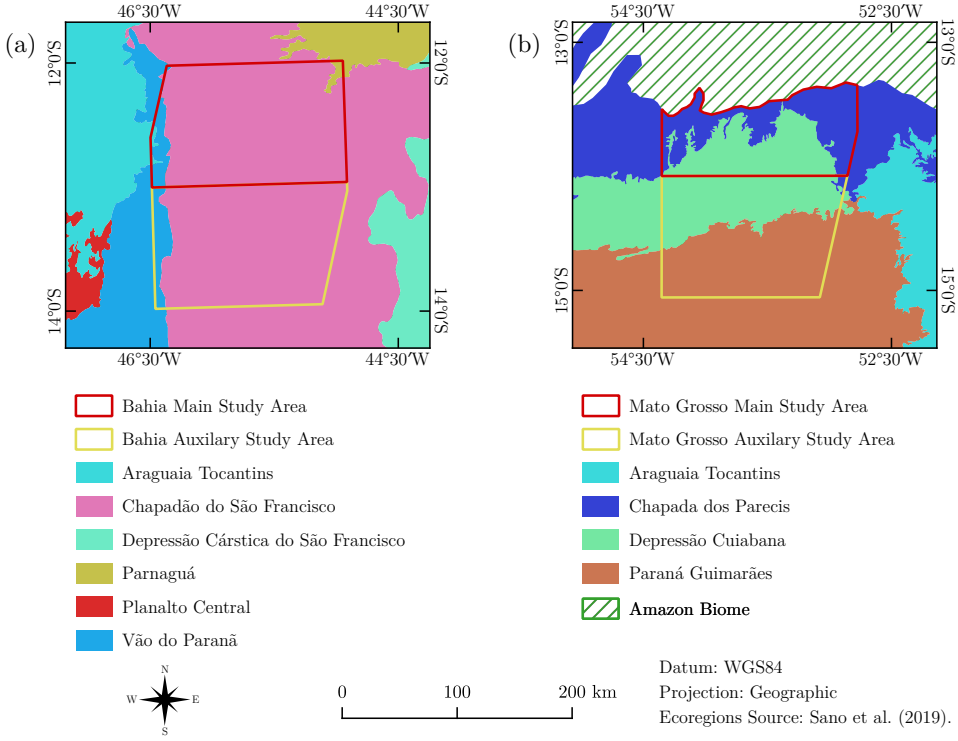

Ecoregions for the study area in Bahia (a) and in Mato Grosso (b).
SOURCE: Author's production.

Another important difference between them is the topography. The deforestation occurrence in Cerrado is correlated with the terrain slope, and the regions present distinct characteristics (ROCHA et al., 2012). The study area in Bahia is composed largely of slopes between 0% and 5% with few profound river valleys, in contrast

with the area in Mato Grosso, which is composed of slopes between 0% and 10% and occasional rocky outcrops (Figure 3.3).

Figure 3.3 - Terrain slope for the study areas in Bahia and Mato Grosso.

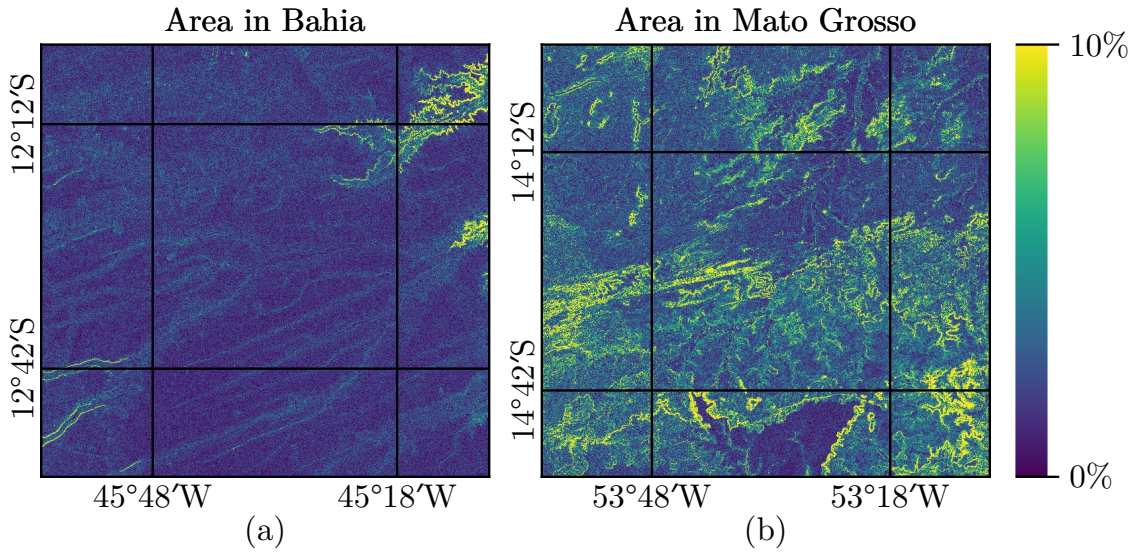

Slopes derived from Shuttle Radar Topography Mission (SRTM) in Google Earth Egine, with $30m$ spatial resolution. (a) for the Bahia study area and (b) for the Mato Grosso study area.

SOURCE: Author's production.

Different regions also present differences in the deforestation occurrence. In Bahia, the degradation occurs in large geometrical fields, while in Mato Grosso it is detected in a greater number of polygons of amorphous shapes. For 2019, the amount of PRODES polygons in Mato Grosso is higher, whilst the total deforestation area and the mean area per polygon are higher for Bahia, as presented in Table 3.1.

Table 3.1 - Deforestation statistics for 2019 in the study areas (main and auxiliary).

	Bahia	**Mato Grosso**
Total Area (ha)	$20,723.315$	$13,326.516$
Mean Polygon Area (ha)	61.676	18.929
Polygon Count	336	704

SOURCE: INPE (2020).

3.2 Approaches for training samples creation

The generation of appropriate training samples is as important as the detection algorithm architecture. One of the most costly and time consuming task is the creation of reference data. One way to reduce this cost is using pre-existing assets obtained for other areas or time periods. Therefore, this work evaluates 3 different approaches to create training samples, considering variations in space and time of the reference data, to better understand the limitations that may exist in each case. Figure 3.4 shows a diagram for these methods.

Figure 3.4 - Approaches to create training samples.

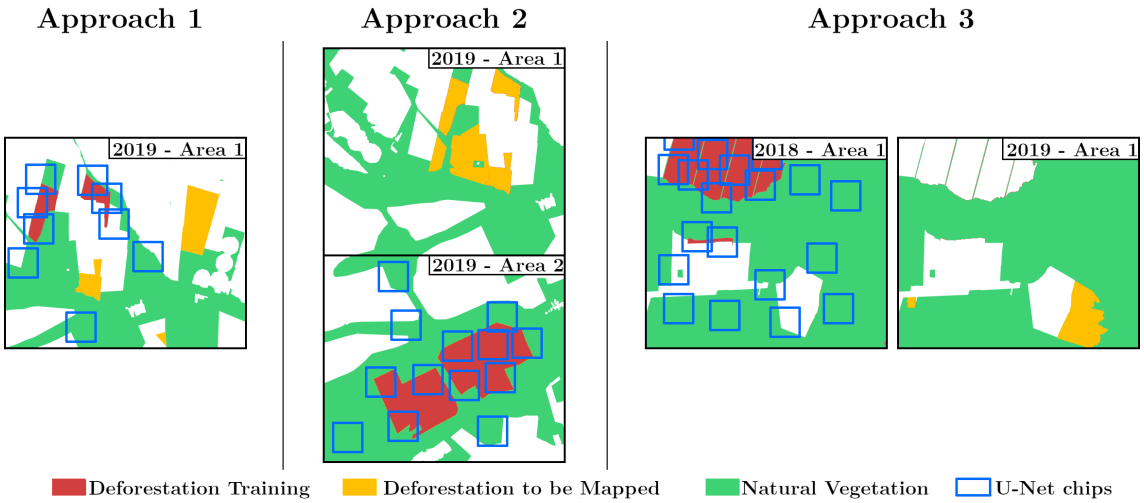

Areas in white color represent past deforestation.

SOURCE: Author's production.

Approach 1

The training samples were selected in some parts of the main study area in 2019. This scenario can be compared to a classification process, in which the training samples are created for a small portion of the study area, and the final product is a complete map for the entire region.

Approach 2

The training samples are created in a study area in 2019, adjacent to the area where the algorithm will be applied. In this case, the 'auxiliary' study areas shown in

Figure 3.1 were utilized to select the training samples. This approach replicates the classification procedure, in which there are good quality thematic maps at nearby study areas that can be used as reference data to train the classification algorithm.

Approach 3

The training samples were selected from the main study area in 2018 while the final classification was carried out for the main study area in 2019. This replicates the classification procedure, in which the thematic maps obtained in the past are utilized as reference data to classify images acquired in posterior data.

In the context of PRODES, the approaches can be ranked according to their applicability. Approach 1 presents the most disadvantages because the analysts would have to carry out visual interpretation, sometimes with aid of field work, to create training samples for all regions. Approach 2 is timidly better since the analysts would focus on classifying only part of the biome, while the rest could be made by the algorithm, reducing the human workload. Approach 3 presents the most advantages since the classification used as reference is already done for the prior PRODES years.

3.3 Deforestation detection

The flowchart in Figure 3.5 summarizes the methods used in the deforestation detection. Every combination between the time series type, approach for the training samples creation, and study area was submitted through this methods.

Figure 3.5 - Flowchart to describe the deforestation detection methodology.

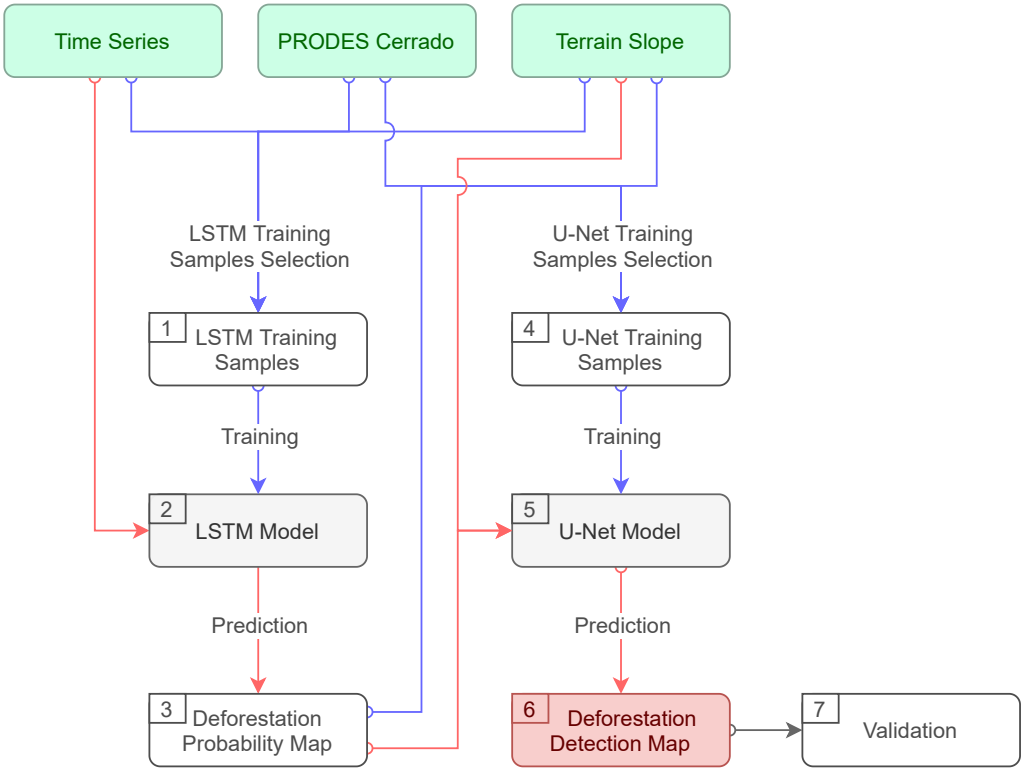

Rectangles: The input data, DL models, and final results are colored in green, gray, and red, respectively. The numbers indicate their order in the flowchart. Connections: operations regarding the models training, operations related to using the trained models to predict over data, and operations of validation are colored in blue, red, and gray, respectively.

SOURCE: Author's production.

In the proposed methodology, 3 main data sources were used: Landsat-8/OLI (NASA, 2013) or Sentinel-2/MSI (ESA, 2021b) time series, PRODES Cerrado deforestation data (INPE, 2020), and the Terrain Slope derived from SRTM (FARR et al., 2007). Section 3.3.2 discusses in detail the input data as well as their pre-processing.

These data sources were used to select training samples for the LSTM algorithm. After the training phase, this model was applied to the satellite image time series to create the deforestation probability map.

The deforestation probability map was then employed in association with PRODES and Slope data to generate training samples for the U-Net algorithm. After training, the U-Net was applied to create the deforestation detection map, from the LSTM result and Terrain Slope.

Afterwards, 12 deforestation maps were created considering all possible combinations of 2 satellite time series (Landsat-8/OLI or Sentinel-2/MSI), 3 training samples scenarios (Approaches 1, 2 and 3), and 2 study areas (Bahia and Mato Grosso). These maps were then validated using a random sampling approach and reference data, created by visual interpretation based on Sentinel-2 time series.

3.3.1 Mapping classes

Three classes were utilized in the detection phase of this work, presented in Table 3.2.

Table 3.2 - Mapping classes in deforestation detection.

Class	Description
Deforestation	Total removal of natural vegetation (change) caused directly by human activity in 2019.
Natural Vegetation	Natural vegetation without deforestation (no change) during 2019.
Past Deforestation	Deforestation detected by PRODES before 2019 (no change).

SOURCE: Author's production.

The "Deforestation" class definition follows the class "Anthropic" in PRODES Cerrado (BRITO et al., 2018). Activities like natural forest clearcut, non natural fires, among others are the main source for the LULC changes, disregarding the posterior use in the deforested area. Although the term "Deforestation" is associated with Forest suppression, the suppression of natural Savanna and Grassland formations is also included.

The class "Natural Vegetation" can be understood as the remaining natural vegetation, without the presence of deforestation throughout the analyzed period. On the other hand, the class "Past Deforestation" is defined as anthropized areas prior to the analyzed period. "Past Deforestation" is obtained from PRODES, which was not directly detected by the proposed algorithm.

3.3.2 Input data

As input data, 2 different sensors were used to create dense image time series: Landsat-8/OLI and Sentinel-2/MSI. Although they were employed separately, only bands with similar spectral intervals were considered for both sensors (Table 3.3). This was done to ignore differences among them related to spectral resolution since this work aims to evaluate the proposed methodology only in the spatial and time axis.

Table 3.3 - Landsat-8 and Sentinel-2 spectral bands used in the processing.

Landsat-8/OLI		**Sentinel-2/MSI**	
Band Num.	**Wavelength (μm)**	**Band Num.**	**Wavelength (μm)**
2	0.450-0.515	2	0.459-0.525
3	0.525-0.600	3	0.541-0.577
4	0.630-0.680	4	0.649-0.680
5	0.845-0.885	8a	0.854-0.875
6	1.560-1.660	11	1.566-1.658
7	2.100-2.300	12	2.104-2.284

SOURCE: Adapted from NASA (2013), ESA (2021b).

The satellite data were obtained from data cubes produced by the BDC project (FERREIRA et al., 2020b). In the context of this project, Landsat-8/OLI bands are composed of pixels with 30 m, while the Sentinel-2/MSI are composed of pixels with 10 m, even for bands 8a, 11, and 12, which are upsampled from 20 m. The proposed methodology also used image time series of 2 vegetation indices: the Normalized Difference Vegetation Index (NDVI) and the Enhanced Vegetation Index (EVI), provided by BDC.

PRODES data was used as reference to create training samples. Because PRODES is created using images from the dry season, the image time series were created to end at this period. Thus, the time series used in the detection are from July 2018 to August 2019 to match with the PRODES deforestation calendar. A temporal interpolation was applied to the time series in order to fill the gaps caused by clouds and cloud shadows, therefore, in order to interpolate the end of the series more precisely, the series were extended until the end of September. However this extension was used only for the interpolation, with the detection of deforestation

being made using images only until the end of August. The availability of surface reflectance images in the BDC repositories was analyzed to create the image time series (Figure 3.6).

Figure 3.6 - Landsat-8/OLI and Sentinel-2/MSI scenes availability for the study areas.

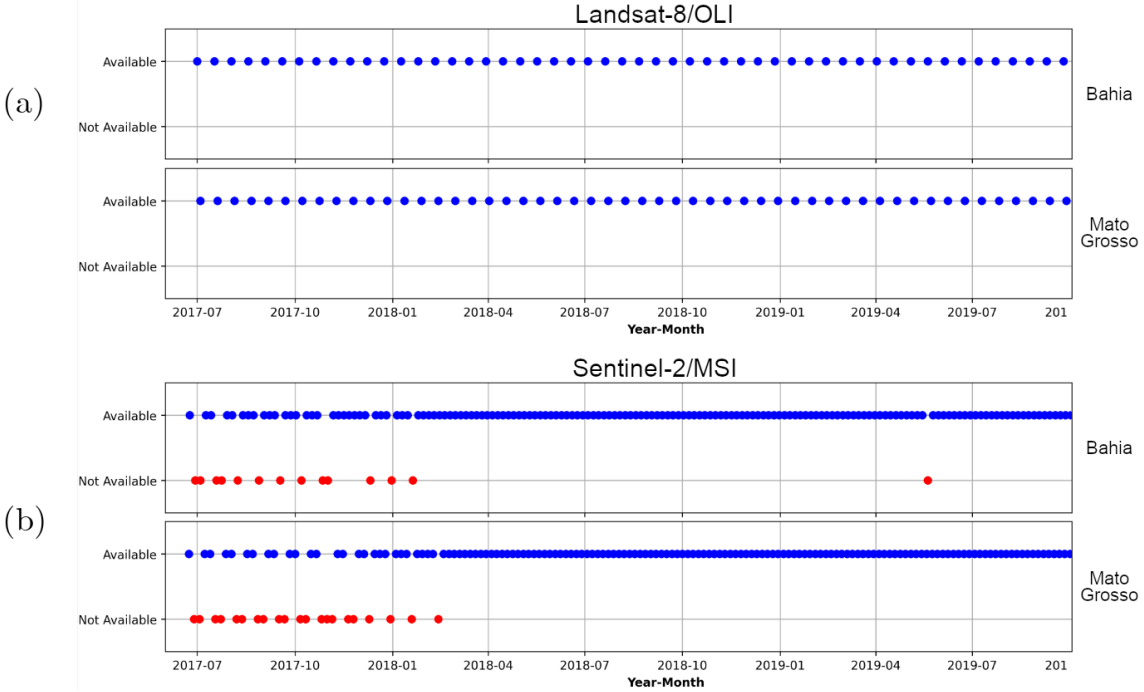

Images availability for the Landsat (a) and Sentinel (b) time series.
SOURCE: Author's production.

From the end of July 2017 to September 2019 there are 52 Landsat-8/OLI images available for the study areas in Bahia and in Mato Grosso. In the case of Sentinel-2/MSI, some images are not available mostly for 2017. Then, missing dates were interpolated in the process of filling data gaps in the images, with the gaps caused by clouds and cloud shadows. From the end of July 2017 to September 2019 there are 164 and 157 Sentinel images available for the Bahia and Mato Grosso study areas, respectively.

To facilitate the time series analysis, some pre-processing steps were conducted to construct and fill the gaps in the time series (Figure 3.7).

Figure 3.7 - Pre-processing steps to create the time series stacks.

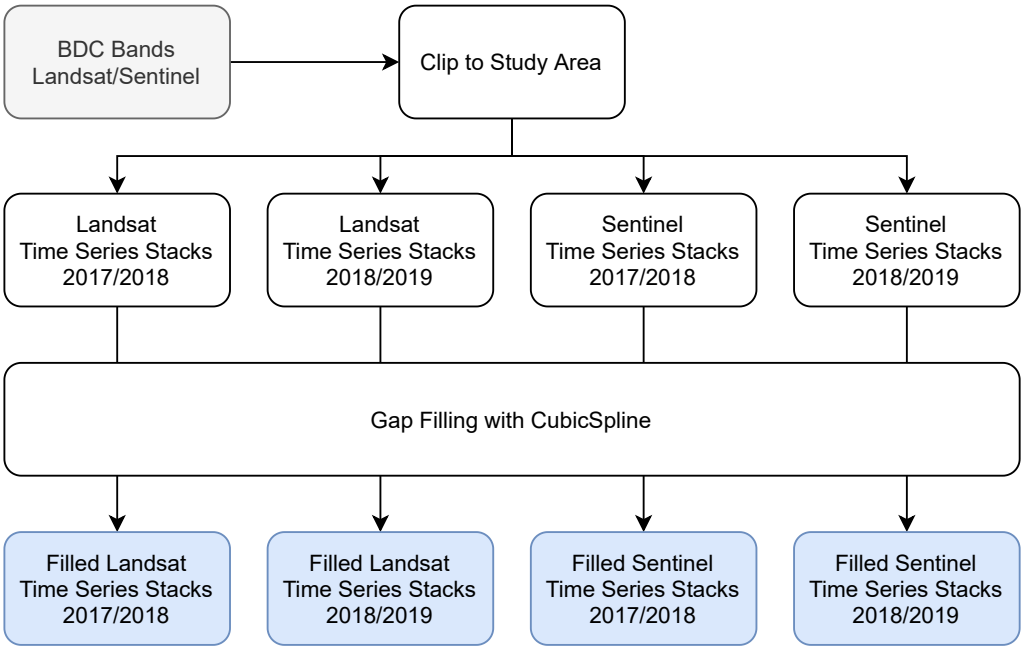

Input data and final image stacks are shown in the colors gray and blue. The gap filling procedure is applied only to pixels that contain clouds, cloud shadows or are missing information.
SOURCE: Author's production.

First, the data (spectral bands and vegetation indices) were clipped using the study area boundaries. Then, stacks were created for each spectral band, for two distinct time intervals: from July 2017 to September 2018, and from July 2018 to September 2019. These time intervals were used to match with the PRODES calendar. After interpolated, the time series were used only until August for the deforestation detection, corresponding with the PRODES years of 2018 and 2019.

There were dates when it was expected to exist Sentinel images, but none was available for download, as it is shown in Figure 3.6b. These missing scenes in Sentinel image time series were flagged completely as clouds/cloud shadows. In the images available for download, the regions where there were clouds or cloud shadows were identified by the Fmask 4.2 method (QIU et al., 2019), applied by BDC and obtained together with the spectral data. In the next processing step, these flagged images and cloudy regions had their values entirely filled according to the spectral behavior of their neighbors in the time axis. In this procedure, a cubic spline algorithm was used to estimate these missing values in the image stacks (DOZIER et al., 2008; HOU et al., 2019). Figure 3.8 shows the reconstruction of a pixel time series made by the gap

filling process. The images download, clip to the study areas, stacks construction and gap filling were all made using custom scripts created using the Python programming language and various freely available libraries.

Figure 3.8 - Cubic spline application to fill gaps in a Landsat-8 NDVI time series.

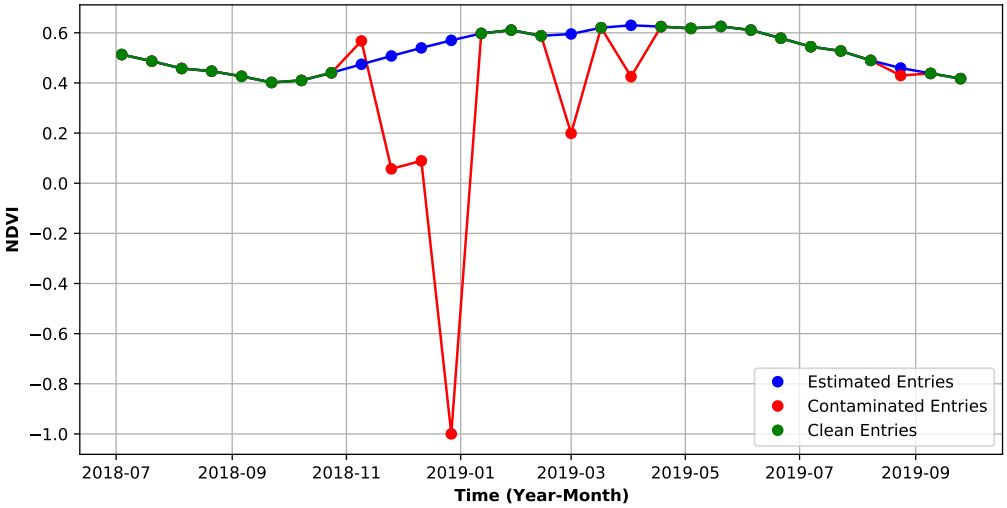

Contamination in the time series is caused by cloud or cloud shadows, which is identified by the mask produced by BDC.

SOURCE: Author's production.

PRODES Cerrado data were acquired in two georreferenced data sets: one with deforestation prior to 2000, and another with deforestation after 2000 separated by year. Using the Quantum Geographic Information System (QGIS), the vectors were merged and used to generate raster datasets, for PRODES 2018 and 2019 to each study area with spatial resolutions according to Landsat and Sentinel data. The terrain slope information was derived from SRTM (FARR et al., 2007), using Google Earth Engine. The original spatial resolution was $30m$, which was used with Landsat data, but for sentinel it was upsampled to $10m$ in order to match the spatial resolution used with this data. Google Earth Engine's standard slope calculation method was used to generate the terrain slope with SRTM data. The data were clipped to the study areas borders and resampled using cubic convolution (KEYS, 1981), to match exactly the pixels of the image time series and make it possible to stack PRODES and slope data with the time series spectral data.

3.3.3 LSTM training and prediction

The LSTM is the first DL step. This architecture was used to evaluate the time series in the time axis, without considering the spatial relations among the pixels. It was implemented specifically for this work in the Python programming language, using the library TensorFlow. The learning rate and number of epochs for this model were optimized for each map, but other general parameters were:

- Model with:
  - One LSTM with 256 output units, *tanh* activation function, and *sigmoid* recurrent activation function;
  - One Batch Normalization Layer;
  - One fully-connected output layer (Dense) with $softmax$ activation function;
- Batch size of 256 samples;
- Adam optimizer; and
- Loss function Categorical Cross-Entropy.

The LSTM model is composed of 3 main layers, as shown in Figure 3.9, where the shape of its output arrays are shown. In the last layer, the model generates an array with the probabilities of a pixel time series being deforestation and natural vegetation, with the sum of both being equal to 1. The deforestation probability is separated, resulting in the model's final output.

Figure 3.9 - The LSTM model layers and their output array shapes.

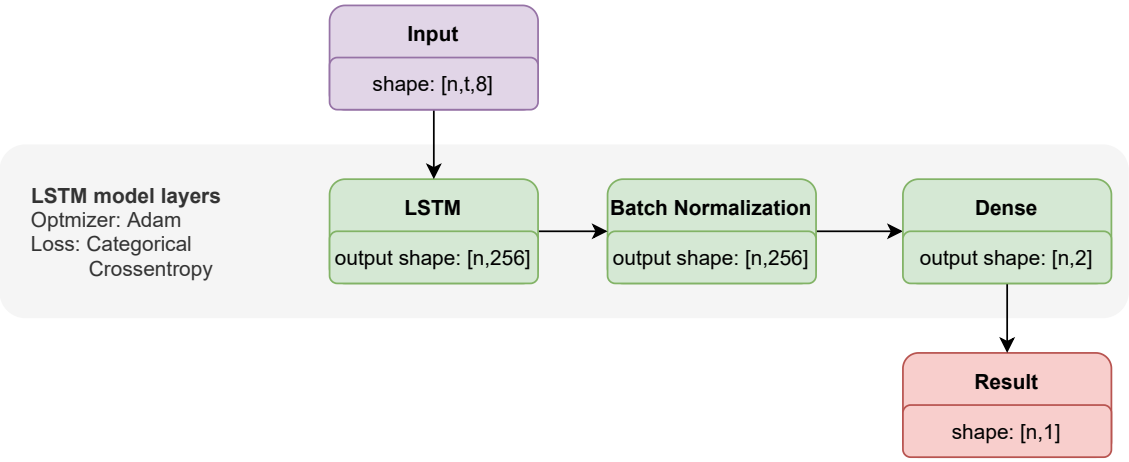

For the shapes, n is the analyzed pixel's number in the batch, t is the number of time entries in the time series (25 for Landsat-8/OLI and 79 for Sentinel-2/MSI). The number 8 in the input shape equals to the number of bands and vegetation indices used (Table 3.3). SOURCE: Author's production.

To train the LSTM, half the training samples are for deforestation and half for natural vegetation. To obtain deforestation samples, pixel time series were selected according to the PRODES deforestation polygons in the analyzed year. The selection of pixel time series respected a maximum number of samples per deforestation polygon, delimited as a maximum of $0.18km^2$ inside each PRODES polygon. Consequently, the maximum number of samples per polygon for Landsat and Sentinel was 200 and 1,800, respectively. This threshold was used in order to avoid the excessive selection of samples in bigger polygons. The natural vegetation samples were selected using PRODES as reference, stratifying them in regions according to the topography slope. Thus, one third of the natural vegetation was selected in regions with terrain slope from 0% to 4%, another third from 4% to 6%, and the last third in regions with slopes higher than 6%.

These proportions were defined in an iterative empirical process, to guarantee an equitable representation in the training phase. Otherwise, the model could favor one class over the other and then affect the results. Table 3.4 shows the number of LSTM samples for the 12 maps created. Since the maximum number of samples by deforestation polygon in Sentinel data is larger than Landsat, the number of training samples in Sentinel is much larger than the amount of samples for Landsat, because of the difference among their spatial resolutions.

Table 3.4 - Number of LSTM training samples for the combinations of time series, study area, and samples approach.

Landsat			
	Approach 1	**Approach 2**	**Approach 3**
Bahia	14,312	18,288	38,840
Mato Grosso	21,536	32,665	42,812
Sentinel			
	Approach 1	**Approach 2**	**Approach 3**
Bahia	310,729	165,025	349,496
Mato Grosso	194,190	293,550	385,734

SOURCE: Author's production.

Every training sample, labeled as natural vegetation or deforestation, is composed of the pixel evolution through time from each spectral band defined in Table 3.3, NDVI, and EVI, as illustrated in Figure 3.10.

Figure 3.10 - LSTM training samples for Sentinel time series.

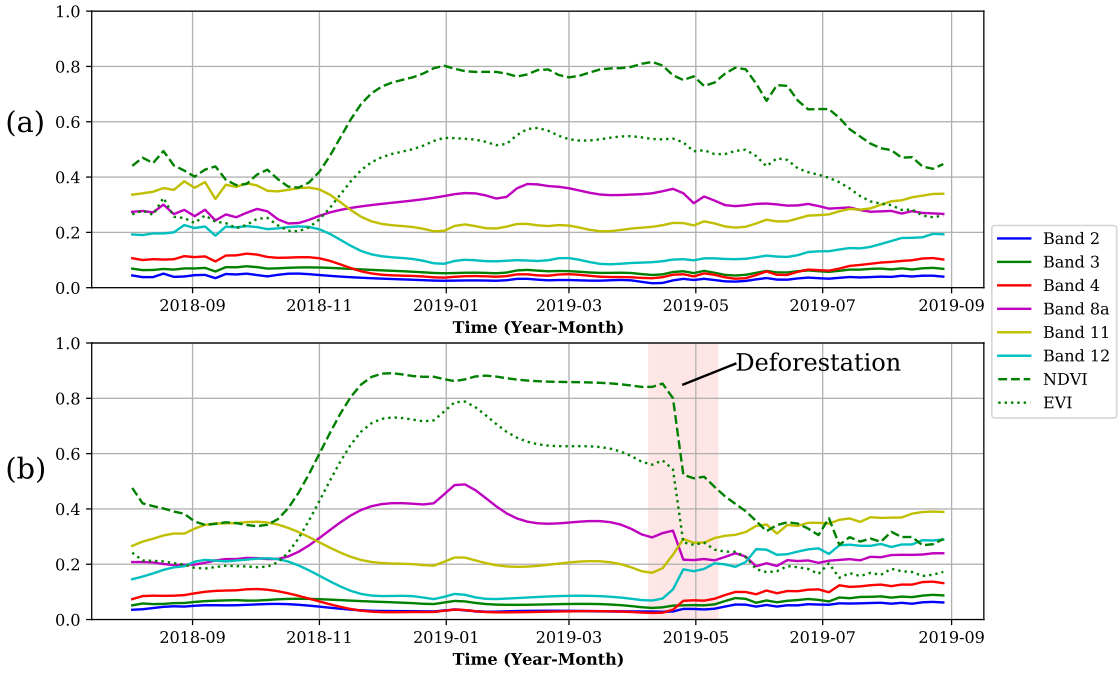

Natural vegetation (a) and deforestation (b).
SOURCE: Author's production.

The LSTM model returns a value between 0 and 1 that corresponds to the probability of the pixel time series belonging to the deforestation class. After training, the model could be used in a prediction procedure for the remaining study area. The LSTM result is a deforestation probability map, which will be used in the next step: U-Net processing.

3.3.4 U-Net training and prediction

In the proposed methodology, U-Net is the second DL architecture. Differently to LSTM, it analyzes the spatial patterns in the data, such as relations of position, shape, texture and values. U-Net was implemented through the DeepGeo python package (MARETTO et al., 2019), which facilitated the application of this DL algorithm.

The input to the U-Net were the deforestation probability map, generated by the LSTM, and the terrain slope. Using this combination, the trained U-Net model can generate the Deforestation map with the classes defined in Table 3.2.

To train the model, training samples composed of probability map, slope, and PRODES reference data were created, as in Figure 3.11. Each sample is called a 'chip' and all chips in the same training have the same dimensions.

Figure 3.11 - Parts of an U-Net chip (sample).

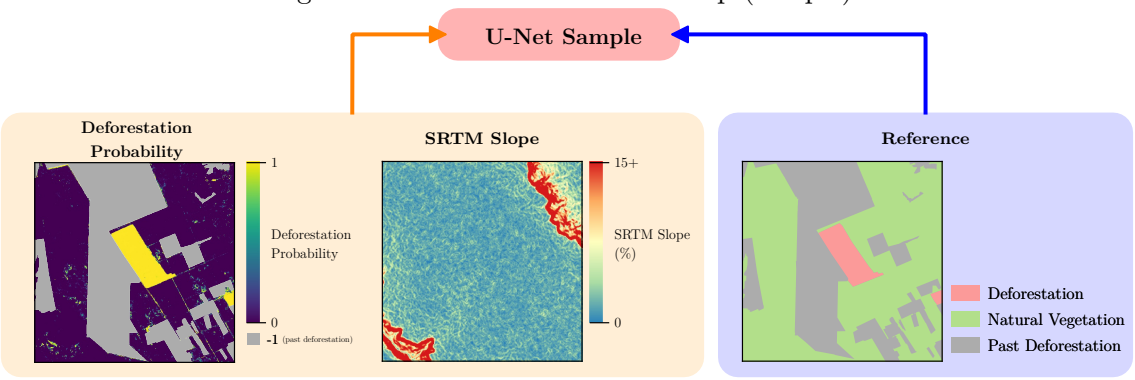

Elements that compose one U-Net training chip. All three elements have the same dimensions (284 x 284 pixels). Classes and data values are converted into real numbers, between -1 and 1 for the Deforestation Probability and SRTM Slope.
SOURCE: Author's production.

Training parameters like epochs, learning rate, and decay rate vary, but common

parameters were defined as:

- Learning rate decay activated;
- L2 regression rate of 0.0005;
- Chip size: 284 pixels;
- Loss function Average Soft Dice (avg_soft_dice); and
- 6 data augmentation operations per sample:
  - 90° rotation;
  - 180° rotation;
  - 270° rotation;
  - Flip horizontally;
  - Flip vertically;
  - Flip transpose.

The chips were manually selected to find optimal sets that have the potential to maximize the classification accuracy. These chips locations were also the same for the same study area and samples approach. For example, for Approach 1 in Bahia, the same location for the training chips were used in the maps created with Landsat-8/OLI and Sentinel-2/MSI time series. However, since the Landsat and Sentinel chips have the same size (284 x 284 pixels), more Sentinel chips could be created inside the area delimited by the Landsat chips, as it is shown in Figure 3.12.

Figure 3.12 - U-Net samples for Approach 2 in Bahia.

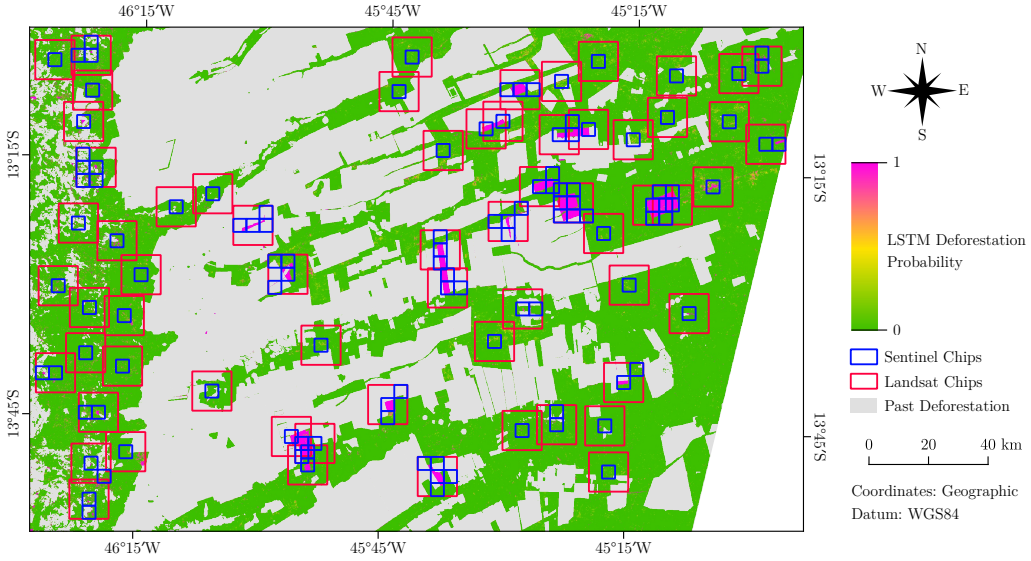

SOURCE: Author's production.

In the chips selection process, the balance between chips with deforestation and without it was maintained as fair as possible, in order to avoid problems due to class imbalance (RENDÓN et al., 2020; YESSOU et al., 2020). Besides, data were included in the chips that represent a wider variety of situations. These aspects were taken into consideration in order to not privilege a class over the other as well as to increase the model's capability to predict accurate results in different regions. Table 3.5 shows the number of U-Net training chips for the 12 maps created. It can be noticed that Approach 1 almost always has less samples than its peers on the same line. This occurred due to the less deforestation area available in this approach as training, since the deforestation occurred in the main study area had to be divided in training and validation. Approaches 2 and 3 had entire adjacent areas or the prior year to use as deforestation reference, leaving all deforestation in the main study area in 2019 as validation.

Table 3.5 - Number of U-Net training samples (chips) after data augmentation for the combinations of time series, study area, and samples approach.

Landsat			
	Approach 1	**Approach 2**	**Approach 3**
Bahia	288	384	450
Mato Grosso	156	210	204
Sentinel			
	Approach 1	**Approach 2**	**Approach 3**
Bahia	468	708	702
Mato Grosso	294	324	336

SOURCE: Author's production.

Afterwards, the classification was generated with a prediction operation. In this operation, the trained model was applied to the whole study area using the LSTM output and the terrain slope, in order to generate the deforestation maps.

3.4 Validation

As classification results, 12 maps were created from 2 different time series (Landsat-8/OLI and Sentinel-2/MSI), 2 study areas (Bahia and Mato Grosso), and 3 training samples approaches. It is recommended to use reference data of better resolution in validation processes (OLOFSSON et al., 2014), and since PRODES deforestation maps are based on Landsat images, they are not suitable to validate deforestation maps obtained from Sentinel-2 time series. Therefore, the validation process for all maps was performed by visual analysis using Sentinel-2 time series.

The validation was acomplished using a stratified random sampling approach in order to create a binary matrix, in which *change* corresponds to "Deforestation" class and *no change* to others. For each deforestation map, the number of validation points was defined by Equation 2.1 (LOHR, 2009), considering a variance of 50% ($\sigma^2 = 0.5$), a standard error of 3% ($e = 0.03$) and a confidence interval of 95% ($z_{\alpha/2} = 1.96$) (PARENTE et al., 2021). This procedure resulted in 1,067 validation points per map.

Since the proportion of area comprised of *change* (Deforestation) is much smaller than the *no change*, it was stipulated that 100 points would be stratified in *change*, as recommended by Olofsson et al. (2014). This would avoid overrepresentation of the *no change* class. consequently, 967 points were stratified in *no change*. The

probability of each stratified point in relation to its category is shown in Table 3.6.

Table 3.6 - Approximated samples probabilities for the validation process.

State	Time Series	Category	Samples Probability (%)
Bahia	Landsat	Change	0.1346
		No Change	0.0100
Bahia	Sentinel	Change	0.0150
		No Change	0.0011
Mato Grosso	Landsat	Change	0.2229
		No Change	0.0139
Mato Grosso	Sentinel	Change	0.0248
		No Change	0.0015

SOURCE: Author's production.

Reference data for every validation point was independently created by visual interpretation over Sentinel-2 time series in the study area. In total, 12,804 reference points were created, representing *change* and *no change* classes.

To facilitate the visual interpretation process, a mask was used to cover the past deforestation areas, which were not included in the validation. Theoretically, all visible areas through the mask were never considered as deforestation, and therefore were analyzed by the DL deforestation detection algorithm. When comparing the visible area with Sentinel-2 reference, it was noticed that some small "Past Deforestation" areas could be observed. This occurred due to the spatial resolution difference between the PRODES product and the Sentinel-2 data. This means that some validation points could be placed in these areas. However, as these points are characterized as "Past Deforestation" they do not fit the "Deforestation" definition, hence being validated as *no change*. After acquiring reference for the validation points, the confusion matrix for each map was obtained to estimate the classification accuracies.

The confidence interval of Overall Accuracy and F1-Score were calculated through $\pm Z_{\alpha/2}(SE)$, where $\alpha = 95\%$, which means a $Z_{\alpha/2}$ value of 1.96. For Overall Accuracy, the SE value was calculated as demonstrated in Section 2.4.1. In the case of the F1-Score, the standard errors Change Producer's Accuracy (P) and Change User's Accuracy (R) were obtained to calculate SE_{F1}. Considering that SE_P and SE_R

are given by Equations 2.10 and 2.9, SE_{F1} can be calculated through these errors propagation since the F1-Score (Equation 2.14) is a function of these 2 variables (P and R), as follows:

$$SE_{F1}^2 = \left(\frac{\partial F1}{\partial P}\right)^2 SE_P^2 + \left(\frac{\partial F1}{\partial R}\right)^2 SE_R^2 \tag{3.1}$$

Thus:

$$SE_{F1} = \sqrt{\left(\frac{2R^2}{(P+R)^2}\right)^2 SE_P^2 + \left(\frac{2P^2}{(P+R)^2}\right)^2 SE_R^2} \tag{3.2}$$

4 RESULTS

Twelve deforestation maps were produced, from the combination of 3 training samples approaches (Approaches 1, 2, and 3), 2 satellite image time series (Landsat-8/OLI or Sentinel-2/MSI), and 2 study areas (Mato Grosso or Bahia). Figure 4.1a shows the LSTM deforestation probability map for the Bahia study area, Approach 1, Sentinel-2/MSI data, and Figure 4.1b shows its deforestation map created with the U-Net.

Figure 4.1 - Result obtained for the Bahia study area using Approach 1 and Sentinel-2/MSI time series.

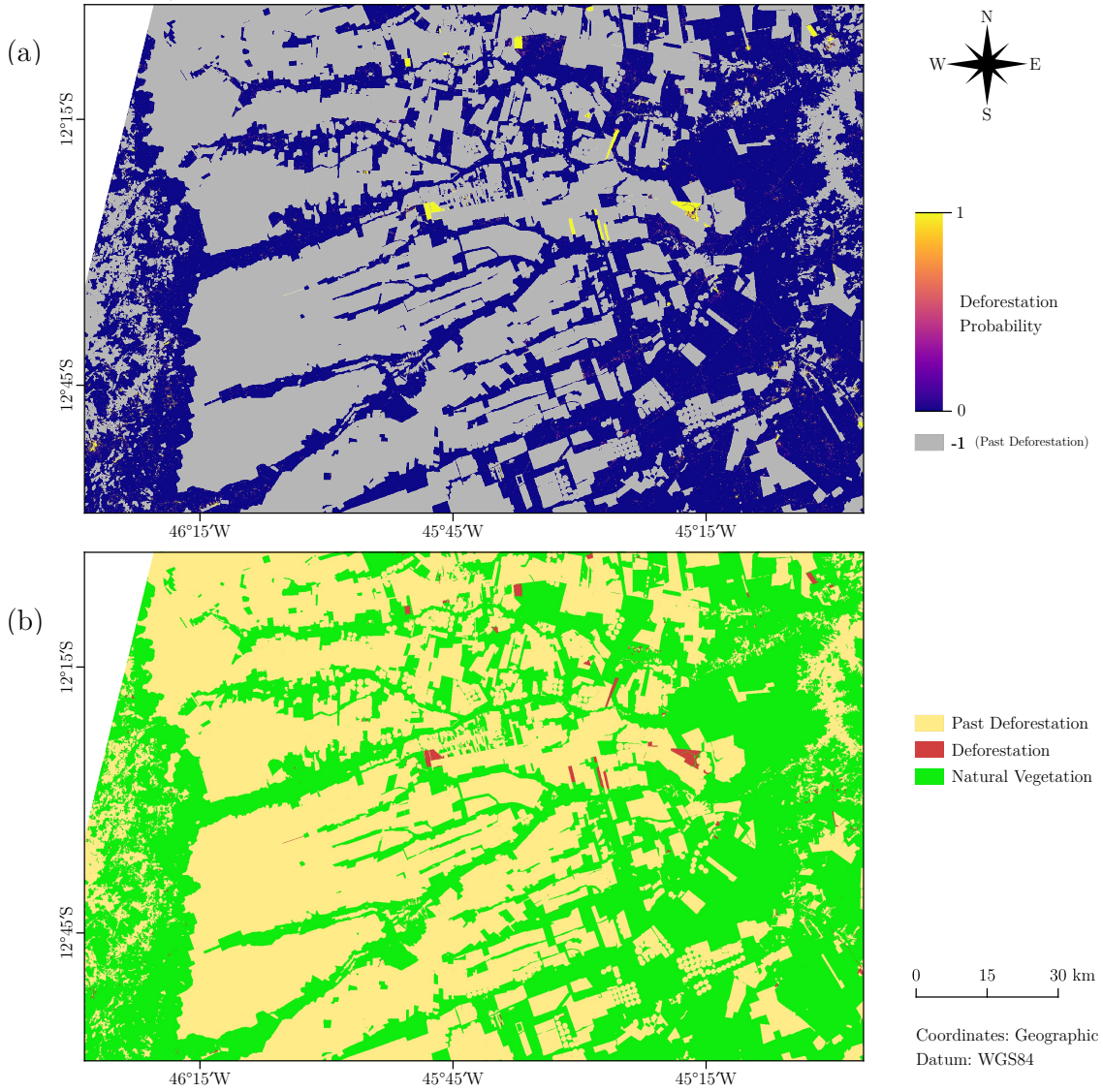

The LSTM deforestation probability map (a) and U-Net deforestation map (b).
SOURCE: Author's production.

Figure 4.2 (c, d, e, f, g, and h) shows part of the 6 deforestation maps for the Mato Grosso study area, corresponding to the largest deforestation occurrence in the region detected by PRODES. Figures 4.2a and 4.2b present RGB (Band 11, Band 8, Band 4) compositions of Sentinel-2/MSI images acquired in August 2018 and 2019, respectively, overlaid by the PRODES deforestation polygon and the past deforestation mask.

Figure 4.2 - Deforestation detection comparison for the Mato Grosso study area.

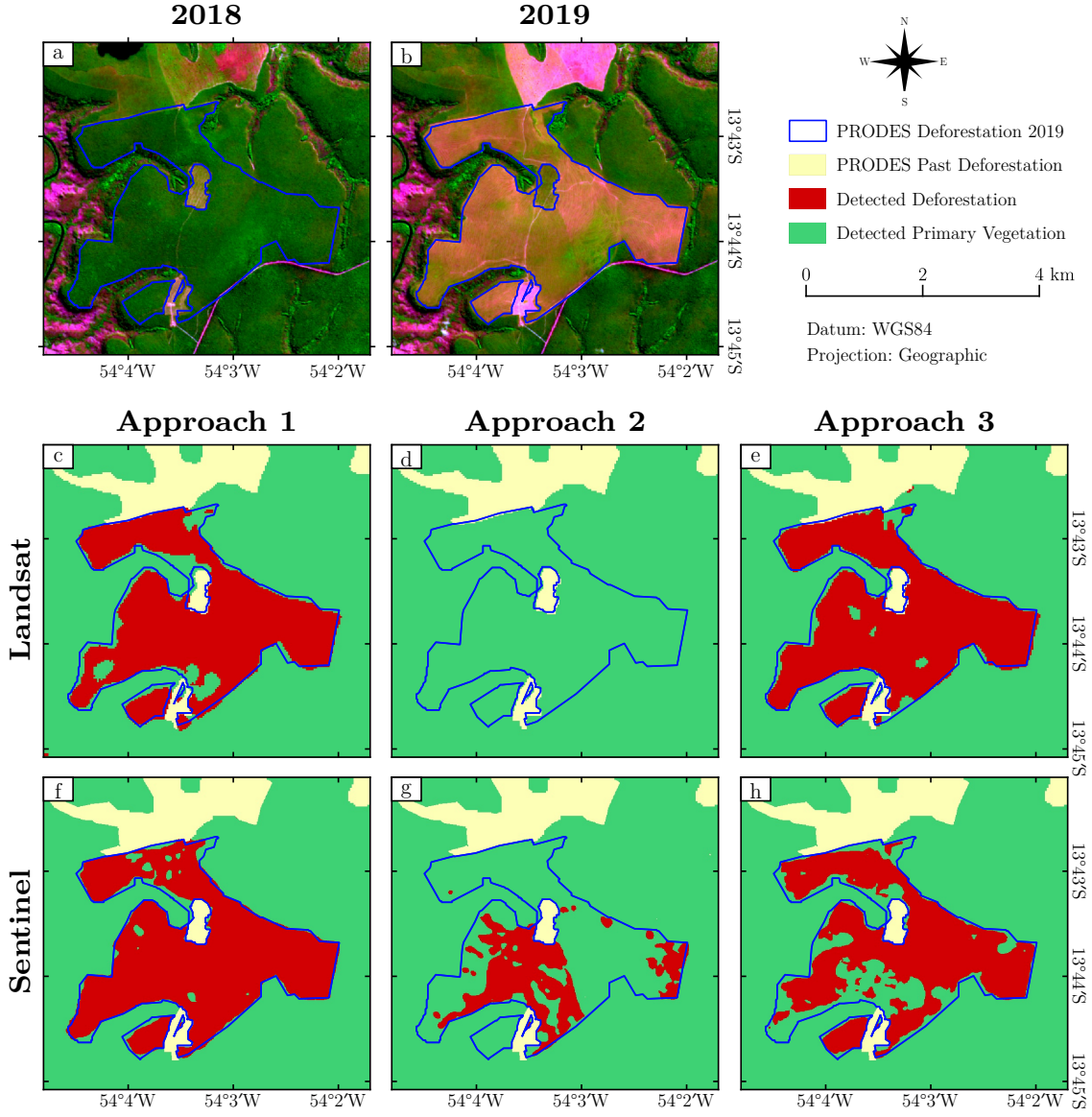

(a) and (b): RGB (Band 11, Band 8, Band 4) Sentinel-2/MSI images for 3 July 2018 and 3 July 2019, respectively, overlaid by the largest PRODES deforestation polygon for the Mato Grosso study area in 2019; (c), (d), and (e): Results using Landsat-8/OLI time series for Approaches 1, 2, and 3, respectively; (f), (g), and (h): Results using Sentinel-2/MSI time series for Approaches 1, 2, and 3, respectively.
SOURCE: Author's production.

Visually, the most accurate deforestation detected corresponds to Approach 1 with Sentinel-2/MSI data (Figure 4.2f). This may be due to the higher spatial and temporal resolutions of Sentinel-2/MSI in relation to Landsat-8/OLI, as well as to the higher correlation degree between training samples and mapped region. In this case they are from the 'main' study area and same year (2019). Although this result is very similar to the PRODES deforestation, it presents some noise not present in PRODES and Sentinel-2 images (Figures 4.2a and 4.2b).

On the other hand, one can notice that results for Approach 2 (Figures 4.2d and 4.2g) are inferior to the others for the deforestation shown. This could be caused by the position of the 'auxiliary' study area, in which the training samples were collected. For the Mato Grosso region, the 'main' area contains parts of Chapada dos Parecis and Depressão Cuiabana ecoregions while 'auxiliary' area contains parts of Depressão Cuiabana and Paraná Guimarães ecoregions (Figure 3.2). In other words, the input data and the training region are not well correlated, demonstrating that maybe differences in vegetation and soil types can influence the results.

The confusion matrices were obtained to create the metrics to evaluate the deforestation maps accuracies. These metrics are presented in Table 4.1, calculated with the confusion matrix weighed according to the proportion of the class areas, as recommended in Olofsson et al. (2014).

Table 4.1 - Validation metrics for the Mato Grosso study area weighed by class areas.

Time Series	**Training Samples**	**OA (%)**	**C-PA (%)**	**NC-PA (%)**	**C-UA (%)**	**NC-UA (%)**
Landsat	Approach 1	99.58 ± 0.35	63.03	99.88	82.00	99.69
	Approach 2	98.96 ± 0.57	33.98	99.78	66.00	99.17
	Approach 3	99.60 ± 0.29	68.27	99.80	69.00	99.79
Sentinel	Approach 1	99.15 ± 0.53	41.34	99.86	79.00	99.28
	Approach 2	98.99 ± 0.60	37.64	99.92	87.00	99.07
	Approach 3	99.09 ± 0.53	38.44	99.81	70.00	99.28

The ± sign represents the confidence interval. Abbreviations: OA = Overall Accuracy; C-PA = Change Producer's Accuracy; NC-PA = No Change Producer's Accuracy; C-UA = Change User's Accuracy; and NC-UA = No Change User's Accuracy.
SOURCE: Author's production.

The Overall Accuracies are very high in Table 4.1, with no significant difference

among them, according to their confidence intervals. For “No Change”, the User’s and Producer’s Accuracies are very high (over 99.07%), indicating that the maps provide very good estimates for this class. In comparison to the other cases, Approach 2 presented the lowest Change Producer’s Accuracy, for both Landsat-8/OLI and Sentinel-2/MSI data. This indicates that the “Change” class has a higher omission error in Approach 2, while the “No Change” class presents a higher commission error. This is clear when observing the maps in Figure 4.2. Overall, for “Change” the User’s Accuracies are higher than the Producer’s Accuracies, which means that the results favor the deforestation reliability over the identification of all deforested areas.

For the Bahia study area another 6 maps were created, with part of them shown in Figure 4.3. The largest deforestation polygon detected by PRODES in 2019 for this study area was chosen to be showcased, as follows.

Figure 4.3 - Comparison for part of the detections made for the Bahia study area.

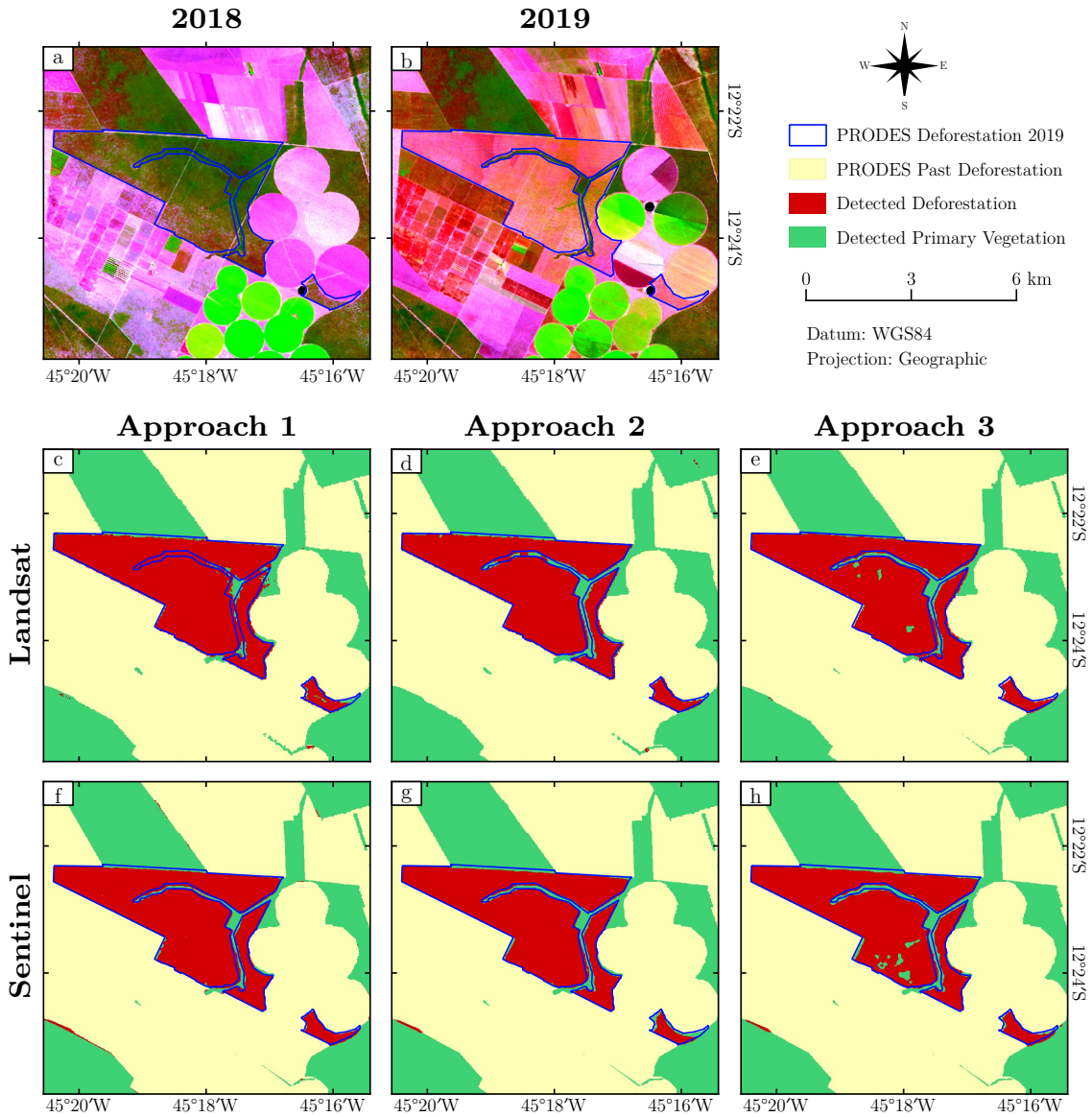

(a) and (b): RGB (Band 11, Band 8, Band 4) Sentinel-2/MSI images for 4 July 2018 and 4 July 2019, respectively, overlaid by the largest PRODES deforestation polygon for the Bahia study area in 2019; (c), (d), and (e): Results using Landsat-8/OLI time series for Approaches 1, 2, and 3, respectively; (f), (g), and (h): Results using Sentinel-2/MSI time series for Approaches 1, 2, and 3, respectively.
SOURCE: Author's production.

Visually, the most accurate deforestation mapping was provided by Sentinel-2/MSI data and Approaches 1 and 2 (Figures 4.3f and 4.3g). In these cases, there were not wrong natural vegetation islands inside the deforestation area as occurred in Approach 3 (Figures 4.3e and 4.3h). Besides, the proposed method correctly detected

thin natural vegetation corridors in the deforestation area, which was not well done in Approaches 1 and 2 using Landsat-8/OLI data (Figures 4.3c and 4.3d). Similar to the Mato Grosso study area, the differences found in the Bahia region may be due to the higher spatial and temporal resolutions of Sentinel-2/MSI data as well as to the higher correlation between the training and mapped data for Approach 1.

For the Bahia study area, Approach 2 is very similar to Approach 1, completely opposite to the Mato Grosso study area. Both 'main' and 'auxiliary' portions are in the same ecoregion, called Chapadão do São Francisco (Figure 3.2).

The validation metrics were estimated from the confusion matrices and are presented in Table 4.2.

Table 4.2 - Validation metrics for the Bahia study area weighed by class areas.

Time Series	**Training Samples**	**OA (%)**	**C-PA (%)**	**NC-PA (%)**	**C-UA (%)**	**NC-UA (%)**
Landsat	Approach 1	99.40 ± 0.45	57.06	99.91	89.00	99.48
	Approach 2	99.81 ± 0.21	86.79	99.91	88.00	99.90
	Approach 3	99.52 ± 0.35	65.71	99.82	77.00	99.69
Sentinel	Approach 1	99.81 ± 0.21	86.93	99.91	89.00	99.90
	Approach 2	99.61 ± 0.35	69.91	99.91	89.00	99.69
	Approach 3	99.77 ± 0.21	86.26	99.88	84.00	99.90

The ± sign represents the confidence interval. Abbreviations: OA = Overall Accuracy; C-PA = Change Producer's Accuracy; NC-PA = No Change Producer's Accuracy; C-UA = Change User's Accuracy; and NC-UA = No Change User's Accuracy.
SOURCE: Author's production.

The Overall Accuracies are very high in Table 4.2, and again their values present no significant difference according to the confidence interval, same as in Table 4.1. By inspecting the Change Producer's and User's Accuracies one observes that the differences among them are not as prominent as they are in the Mato Grosso study area, and they also have higher values, therefore the deforestation in Bahia was more accurately identified.

Another pattern can also be observed in the Change User Accuracy, in which Approaches 1 and 2 perform similarly with values equal to 88% or 89%. Differently, Approach 3 presents lower Change User Accuracy values, such as 77% for Landsat-

8/OLI data and 84% for Sentinel-2/MSI data. This pattern indicates that the commission error is lower in Approaches 1 and 2. In other words, fewer "Natural Vegetation" areas were erroneously classified as "Deforestation".

Another way to evaluate a map is through its F1-Score (Table 4.3) providing other means of interpretation of the maps qualities.

Table 4.3 - F1-Score for the deforestation class.

Time Series	**State**	**Training Samples**	**F1-Score**
Landsat	Mato Grosso	Approach 1	0.713 ± 0.171^{ab}
		Approach 2	0.449 ± 0.140^{b}
		Approach 3	0.686 ± 0.159^{ab}
Landsat	Bahia	Approach 1	0.695 ± 0.161^{ab}
		Approach 2	0.874 ± 0.118^{a}
		Approach 3	0.709 ± 0.153^{ab}
Sentinel	Mato Grosso	Approach 1	0.543 ± 0.157^{b}
		Approach 2	0.526 ± 0.150^{b}
		Approach 3	0.496 ± 0.150^{b}
Sentinel	Bahia	Approach 1	0.880 ± 0.118^{a}
		Approach 2	0.777 ± 0.156^{ab}
		Approach 3	0.851 ± 0.119^{a}

The exponent letters in the F1-Score values represent groups in which it is statistically the same. Group a are the highest values and group b are the lowest values. The $\pm$ sign represents the confidence interval.
SOURCE: Author's production.

The highest F1-Score values belong to group a and were obtained using Landsat-8/OLI time series in Mato Grosso with Approaches 1 and 2, and in Bahia with Approaches 1, 2, and 3, also using Sentinel-2/MSI time series in Bahia with Approaches 1, 2, and 3. On the other hand, the lowest F1-Scores belong to group b and were obtained using Landsat-8/OLI time series in Mato Grosso with Approaches 1, 2, and 3, and in Bahia with Approaches 1 and 3, and also using Sentinel-2/MSI time series in Mato Grosso with Approaches 1, 2, and 3, and in Bahia with Approach 2. These results suggest that the deforestation detection was more successful for the Bahia study area.

The source code for this work is available at `https:`

//github.com/menimato/Deforestation-TimeSeries-DL/tree/db858ad41a7f266a63c20e3879181bf5940b2a92 and is free to use or modify. The repository has jupyter notebooks that contain python code to all steps of the methodology, from downloading the images until making the final deforestation detection.

5 DISCUSSION

5.1 Differences in the study areas

Regarding both study areas, it is clear that the deforestation detection was more accurately achieved in the Bahia study area, according to its higher F1-Scores. By further inspecting the groups defined in Table 4.3, one can notice that group *a* is composed of 6 maps for Bahia and only 2 maps for Mato Grosso, representing the higher F1-Scores. On the other hand, group *b* contains 6 maps for the Mato Grosso study area and only 3 from Bahia, corresponding to lower F1-Scores. This may be explained by the location of the study area as well as the deforestation patterns present in this specific region.

According to Sano et al. (2019), the ecoregions were defined taking into account the geomorphology, vegetation, soil, geology, and flora features, which present considerable differences among ecoregions. Analyzing their location, the study area in Bahia is far from the biome's border and is within one ecoregion. Moreover, the Mato Grosso study area is located in the transition zone between the Cerrado and Amazonia biomes, which contain parts of three different ecoregions (Figures 3.1 and 3.2). Therefore, the Mato Grosso study area is more complex because it presents heterogeneous vegetation patterns, which hinder the deforestation detection task. This agrees with other works, which have been reported that discrimination between natural vegetation and other LULC targets in the Cerrado biome is difficult due to the heterogeneous vegetation structure and canopy (REYNOLDS et al., 2016; ALENCAR et al., 2020).

Other important information is that in the Bahia study area, in 2019, there were fewer deforestation polygons of larger size while the Mato Grosso study area had more polygons, but smaller and with amorphous shapes (Table 3.1). The smaller polygons in Mato Grosso led to the inclusion of many mislabeled deforestation series as LSTM training samples, and as it is shown in Jiang et al. (2017) and in Li et al. (2021), compromised reference data severely degenerate the performance of DL models. This mislabeling occurred because PRODES has small uncertainties in register and polygons borders (MAURANO et al., 2019b; PARENTE et al., 2021), and with smaller areas the chance of selecting series at polygons borders are high, maximizing the influence of these uncertainties. Furthermore, Maurano et al. (2019b) reported the relationship between deforestation patterns and their mapping accuracy. According to the authors, more complex deforestation polygons present higher uncertainties, therefore the Mato Grosso study area could have deforestation refer-

ence less accurate than Bahia.

5.2 Deforestation patterns and time series data

In Figure 3.10, one can observe that there is a clear difference in the natural vegetation and the deforestation samples. The natural vegetation NDVI, for example, starts to rise in November 2018 during the wet season. It reaches a plateau in January 2019 and slowly starts to decrease in June 2019 during the dry season. On the other hand, the deforestation NDVI profile follows a similar pattern as the natural vegetation in the beginning, but shortly thereafter it got an abrupt fall in April 2019. This implies that in this abrupt change there was a natural vegetation suppression. This pattern is accessible through time series, which describe changes over time.

In this work, two types of image time series were used: (1) Image time series from Landsat-8/OLI, with $30m$ spatial resolution and temporal resolution of 16 days (NASA, 2013), and (2) Image time series from Sentinel-2/MSI, with up to $10m$ spatial resolution and temporal resolution of 5 days (ESA, 2021b). The results achieved showed the superiority of Sentinel-2/MSI over Landsat-8/MSI data when comparing the deforestation detections in Figures 4.2 and 4.3.

Alencar et al. (2020) stated that Landsat data have limitations if used to discriminate grasslands, savannas, and forests when the natural vegetation appears as a mosaic of these three vegetation types. Lima et al. (2019) also pointed out better maps created using Sentinel-2 than using Landsat-8 in their study about selective logging in the Amazon. Furthermore, Alencar et al. (2020) and Bueno et al. (2019) indicated that Sentinel-2 data could be used instead to achieve better results in the Cerrado classification. These studies imply that time series with better spatial and temporal resolutions result in better maps, therefore agreeing with our results.

Müller et al. (2015) used Landsat time series to identify cropland, pasture, and natural savanna in Cerrado and they stated that the high accuracy classification was only achieved due to the combination of spectral and temporal information. Vegetation studies have reported that dense time series were helpful to understand variations in phenology (SCHWIEDER et al., 2016; MÜLLER et al., 2015). One explanation for these results, and possibly for the results of this work too, is that more dense time series provide better representation of vegetation cycles or breaks in them, since information is more detailed and data scarcity due to clouds or cloud shadows is improved.

It is important to stress that the image time series provided by the BDC project facilitated the development of this work (FERREIRA et al., 2020b). ARD image time series could be immediately acquired, without waiting for the atmospheric correction algorithm to be processed. The images acquisition through their BDC grid cells also presented advantages, considering that the study areas would occupy multiple scenes in the standard Landsat and Sentinel grids, but occupied only one or two grid cells in BDC.

5.3 Training samples variation in location and time

Training data selection is a challenge in RS applications based on DL techniques (SHI et al., 2020). Three different approaches were evaluated for the training samples selection in this work: (1) samples in the same area and year as the data to be processed (Approach 1), (2) samples in the same year but in an adjacent region (Approach 2), and (3) samples in the same area but in a previous year (Approach 3).

In the Mato Grosso study area, Approach 2 presented the worst results, with its F1-Scores belonging only to group *b* in Table 4.3. This information contrasts with Approach 2 for the Bahia study area, in which the F1-Scores belong to group *a*. In the case of Approach 2, the portions where the training samples and the deforestation map were created belong to different ecoregions in Mato Grosso (Figure 3.2), hinting that their vegetation and deforestation patterns may be different. This difference in patterns would decrease the samples quality, hence the poorer results found, because the quality of reference samples is crucial to obtain accurate results (JIANG et al., 2017; LI et al., 2021; RENDÓN et al., 2020). It can be recommended that the representability of the training data in relation with mapped data should be verified, before using data from different areas or time periods to train a DL model.

Approach 3 did not perform consistently better or worse than Approach 1. In this case, since the training samples were selected in the same area, but using data for the prior year, interannual spectral differences between PRODES years 2018 and 2019 could compromise the results (OLIVEIRA et al., 2010). An strategy to minimize this influence is to use more than just the prior year, what would also considerably increase the number of training samples available. In this case more training samples could improve the results even further, in Adarme et al. (2020), as the quantity of training data increased, better results were achieved.

5.4 Comparisons with other methodologies for deforestation detection

Adarme et al. (2020) compared 3 different DL methods (Early Fusion, Siamese Network, and Convolutional Support Vector Machine), to detect deforestation in a region of Cerrado in the Maranhão State, using two Landsat images from 3 September 2017 and 22 September 2018. Their methodology is less complex than the one proposed in this work and therefore more easily replicated for the entire biome, however, the results obtained by the combination of LSTM and U-net proposed achieved higher accuracies than theirs, which were 98.0% and 0.770, respectively for the Overall Accuracy and F1-Score. The best values obtained in this work for the Overall Accuracy and F1-Score were $99.81\% \pm 0.21$ and 0.880 ± 0.118, respectively. Their training strategy is similar to Approach 1 proposed in this work.

Maretto (2020) used images from two dates to detect deforested areas in the Cerrado, one at the beginning and one at the end of the PRODES year. These two images were employed together in a U-Net with late spatio-temporal fusion, combining the images to detect deforestation. Although their tests were also made for western Bahia, their classes followed different definitions, the "Past Deforestation" was grouped with "Deforestation". As in Adarme et al. (2020), this methodology is easier to scale for large areas, but the accuracy is not as high as the results found for the proposed methodology combining LSTM and U-Net.

Taquary (2019) also used a combination of LSTM and U-Net to detect deforestation in Cerrado, achieving an F1-Score of 0.9035, similar to ours. In their work, an image time series with 13 entries for a portion of the Goiás State was used, where each image was a monthly mosaic made with Planet images, with a spatial resolution of $3m$. In spite of their higher spatial resolution, they used only 4 spectral bands (red, green, blue, and near infrared). Although their F1-Score was high, the use of paid images would not be viable for monitoring the entire biome, also high quality reference data had to be acquired in order to create the training samples.

Parente et al. (2021) performed an assessment of the PRODES Cerrado quality metrics and reported an Overall Accuracy of $93.17\% \pm 0.89$ for the year 2018. As mentioned before, deforestation polygons are identified by analysis through visual interpretation in the PRODES project. Mapping the Cerrado is complex, because of its complexity and variations in vegetation and deforestation, covering a continental area, what highlights the high quality obtained by PRODES in its products. Similar results were obtained in this work, also using freely available images.

Comparing with PRODES, the proposed method needs a larger amount of data, which are also pre-processed by more intensive algorithms. The data preparation and deforestation identification tasks require high performance computing nevertheless it is almost totally automatic and does not need interference from many specialists. Currently, subjective work is only needed in the training samples selection and optimization of training parameters.

Considering the deforestation maps produced by the proposed methodology using Approach 1 and Sentinel-2/MSI image time series, Figure 5.1 shows its agreement with PRODES Cerrado deforestation data.

Figure 5.1 - Agreement comparison between PRODES Cerrado data for 2019 and the detection maps obtained by the proposed method using Sentinel-2/MSI and Approach 1.

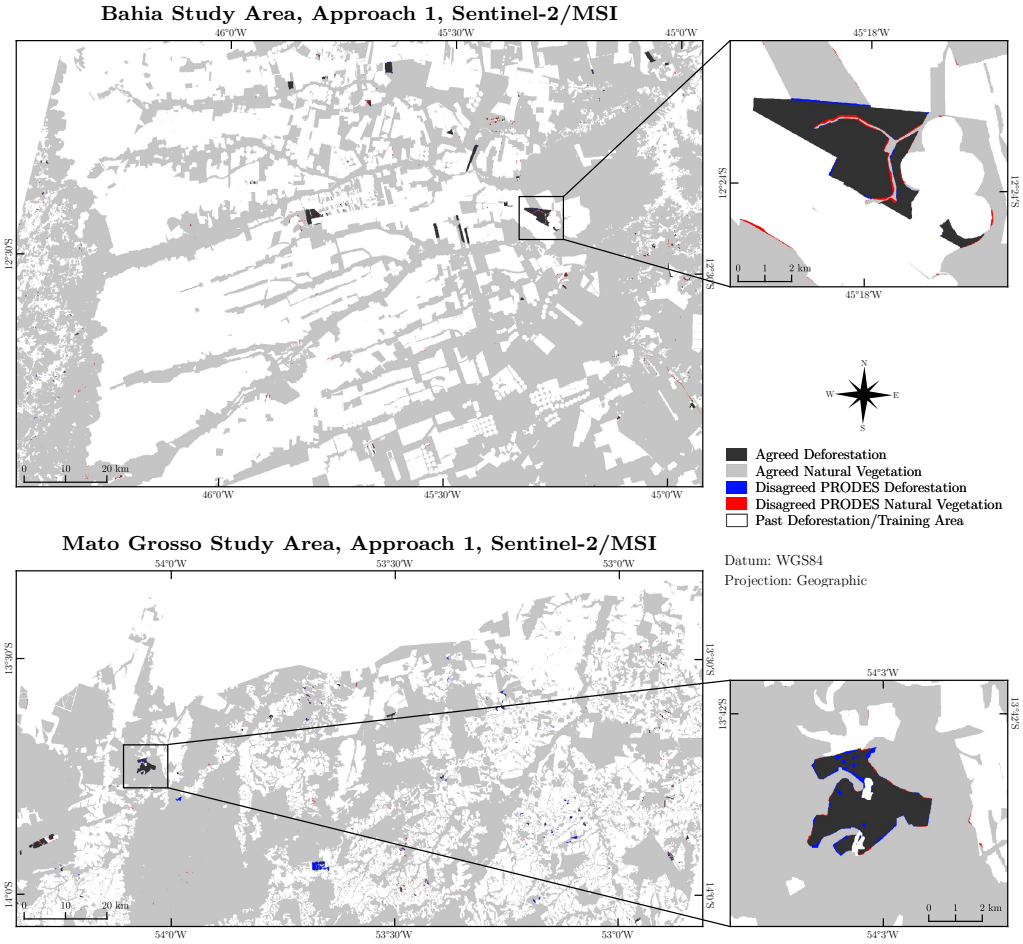

SOURCE: Author's production.

One can observe that PRODES and the maps produced using the proposed methodology present high agreement between the deforestation occurrence and the remaining natural vegetation. There was only one considerable misclassification in the Mato Grosso study area, due to the subtle change in pattern presented in this deforestation. To better understand the reasons for this disagreement, Figure 5.2 shows the LSTM deforestation probability for this polygon.

Figure 5.2 - LSTM deforestation probability for the deforestation polygon in the Mato Grosso study area that disagreed with PRODES.

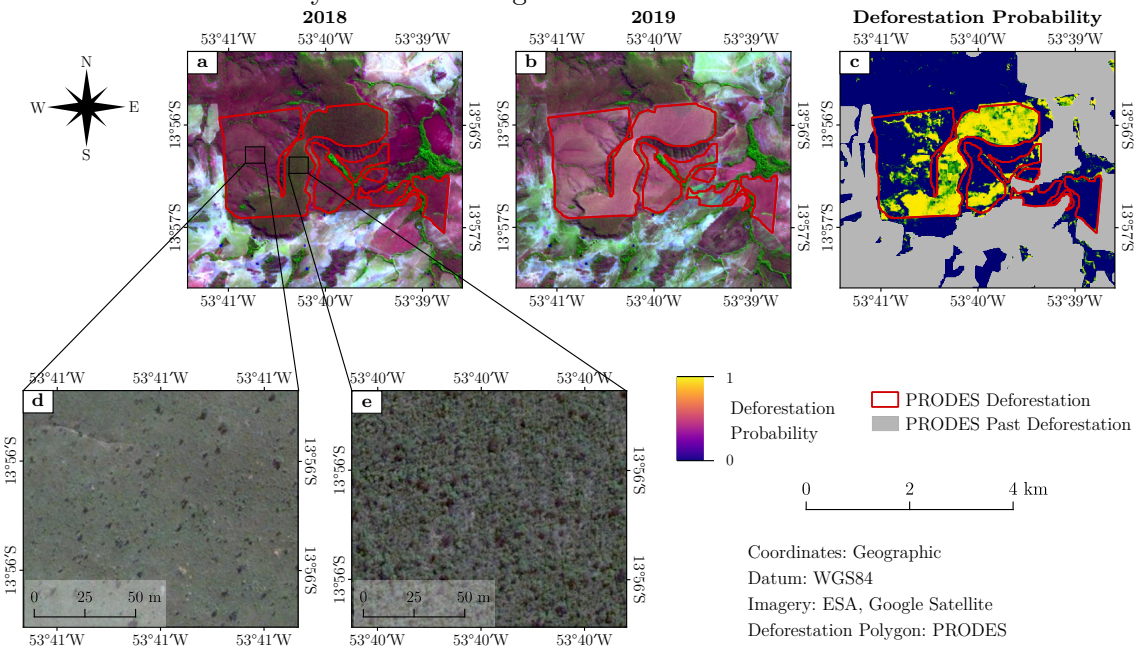

(a) and (b): RGB (Band 11, Band 8, Band 4) Sentinel-2/MSI images for 3 July 2018 and 3 July 2019, respectively, overlaid by a PRODES deforestation polygon for the Mato Grosso study area in 2019. (c) is the LSTM deforestation probability map overlaid by the PRODES deforestation polygon and PRODES past deforestation. (d) and (e) are Google Maps images of natural vegetation that existed before deforestation in 2019, the first is a Grassland Formation and the second is a Savanna Formation. It can be noticed that the LSTM deforestation probability is more accurate for the Savanna Formation.

SOURCE: Author's production.

Figures 5.2a and 5.2b evidence that the PRODES deforestation detection was correct, but in Figure 5.2c only some patches of this polygon had accurate high deforestation probabilities. Comparing the deforestation probabilities with the natural vegetation showed in Figure 5.2a, one can notice that where the natural vegetation was greener, the deforestation probabilities were high, while in the magenta areas

the probabilities were low. By further inspection, it can be verified that the magenta region belongs to Grassland Formations, while the green regions belong to Savanna Formations, as its shown in Figures 5.2d and 5.2e. Therefore, the LSTM model may have less accurate results for deforestation in Grassland Formations for Mato Grosso, hence the disagreement with PRODES. Other RS works also reported difficulties regarding Grassland Formations in mapping procedures (MÜLLER et al., 2015; SANO et al., 2010).

For the Bahia study area and Landsat data, around 1 hour was needed to train the LSTM model, create the deforestation probability map, train the U-Net, and generate the final deforestation map, using a Tesla V100-SXM2-16GB GPU. Considering that the "main" study area in Bahia has $17,949.225km^2$, one can estimate that around 111 hours would be needed to map the entire Cerrado. This estimation considers that the Cerrado would be divided into smaller areas the same size as the "main" study area in Bahia, with one LSTM and U-Net model for each. In case less models were created, i.e. subdividing the biome in larger areas like its ecoregions, the estimated time could be even shorter.

6 CONCLUSIONS

In this work, we proposed a methodology to detect deforestation in the Cerrado biome using Landsat and Sentinel time series through a combination of two DL architectures: LSTM and U-Net. The method uses PRODES deforestation polygons as a reference and image time series generated from Landsat and Sentinel-2 images to train the LSTM model. The probability map resulting from the LSTM is combined with PRODES and SRTM slope data to train the U-Net model, which is used to produce the final deforestation map.

The proposed method showed great potential to be applied to medium spatial resolution images such as Landsat-8 and Sentinel-2 to detect deforestation in Cerrado with a high overall accuracy of $99.81\% \pm 0.21$. The combination of LSTM and U-Net was able to rapidly process image time series for large areas in Cerrado. In addition, the comparison of our deforestation map with PRODES 2019 showed high agreement between them. Hence, these facts reveal the potential of our method to be applied to the entire Cerrado biome and then to automate the PRODES deforestation detection process that is currently performed by visual interpretation.

We also observed that past deforestation maps were used with success to train the algorithm. As PRODES Cerrado provides deforestation data from 2000 onward, more training samples can be selected, taking advantage of the long-term earth observation programs. For future work, we propose to divide the Cerrado biome into ecoregions (SANO et al., 2019) and apply our method for each one of these ecoregions separately in order to successfully detect the deforestation of the entire Cerrado biome using Sentinel-2 imagery.

REFERENCES

ADARME, M. O.; FEITOSA, R. Q.; HAPP, P. N.; ALMEIDA, C. A. d.; GOMES, A. R. Evaluation of deep learning techniques for deforestation detection in the Brazilian Amazon and Cerrado Biomes from remote sensing imagery. **Remote Sensing**, v. 12, n. 6, p. 910, mar 2020. ISSN 2072-4292. 59, 60

AGÊNCIA NACIONAL DE ÁGUAS - ANA. **Regiões hidrográficas**. 2018. Available from: <http://dadosabertos.ana.gov.br/datasets/b78ea64219b9498c8125cdef390715b7_0>. Access in: 10 Apr. 2021. 1

ALBUQUERQUE, A. C. S.; SILVA, A. G. **Agricultura tropical: quatro décadas de inovações tecnológicas, institucionais e políticas**. Brasília: EMBRAPA Informação Tecnológica, 2008. 700 p. ISBN 9788573834321. 5

ALENCAR, A.; SHIMBO, J. Z.; LENTI, F.; MARQUES, C. B.; ZIMBRES, B.; ROSA, M.; ARRUDA, V.; CASTRO, I.; RIBEIRO, J. F. M.; VARELA, V.; ALENCAR, I.; PIONTEKOWSKI, V.; RIBEIRO, V.; BUSTAMANTE, M. M. C.; SANO, E. E.; BARROSO, M. Mapping three decades of changes in the Brazilian Savanna native vegetation using Landsat data processed in the Google Earth Engine platform. **Remote Sensing**, v. 12, n. 6, p. 924, mar 2020. ISSN 2072-4292. 57, 58

ALPAYDIN, E. **Introduction to machine learning**. 3. ed. Cambridge, MA, Estados Unidos da América: MIT Press, 2014. 613 p. ISBN 9780262028189. 19

APPEL, M.; PEBESMA, E. On-demand processing of data cubes from satellite image collections with the gdalcubes library. **Data**, v. 4, n. 3, p. 92, jun 2019. ISSN 2306-5729. 15

BALL, J. E.; ANDERSON, D. T.; CHAN, C. S. Comprehensive survey of deep learning in remote sensing: Theories, tools, and challenges for the community. **Journal of Applied Remote Sensing**, v. 11, n. 04, p. 1, sep 2017. ISSN 1931-3195. 3, 18

BARBOSA, C. C. F.; NOVO, E. M. L. de M.; MARTINS, V. S. **Introdução ao Sensoriamento Remoto de Sistemas Aquáticos: Princípios e Aplicações**. São José dos Campos: Instituto Nacional de Pesquisas Espaciais, 2019. Available from: <http://www.dpi.inpe.br/labisa/livro/>. 11

BELWARD, A. S.; SKØIEN, J. O. Who launched what, when and why; trends in global land-cover observation capacity from civilian earth observation satellites. **ISPRS Journal of Photogrammetry and Remote Sensing**, v. 103, p. 115–128, 2015. ISSN 09242716. 11, 13

BENDINI, H. N.; FONSECA, L. M.; SCHWIEDER, M.; RUFIN, P.; KORTING, T. S.; KOUMROUYAN, A.; HOSTERT, P. Combining environmental and Landsat analysis ready data for vegetation mapping: A case study in the Brazilian Savanna biome. **International Archives of the Photogrammetry, Remote Sensing and Spatial Information Sciences - ISPRS Archives**, v. 43, n. B3, p. 953–960, 2020. ISSN 16821750. 7, 12

BENDINI, H. N.; FONSECA, L. M. G.; SCHWIEDER, M.; KÖRTING, T. S.; RUFIN, P.; SANCHES, I. D. A.; LEITÃO, P. J.; HOSTERT, P. Detailed agricultural land classification in the Brazilian Cerrado based on phenological information from dense satellite image time series. **International Journal of Applied Earth Observation and Geoinformation**, v. 82, n. June, p. 101872, 2019. ISSN 03032434. 12, 15

BOUCHER, D.; ROQUEMORE, S.; FITZHUGH, E. Brazil's success in reducing deforestation. **Tropical Conservation Science**, v. 6, n. 3, p. 426–445, aug 2013. 9

BRASIL. MINISTÉRIO DE CIÊNCIA, TECNOLOGIA E INOVAÇÕES - MCTI. **FIP - monitoramento Cerrado**. 2021. Available from: <https://monitoramentocerrado.mcti.gov.br/>. Access in: 10 Apr. 2021. 2

BRASIL. MINISTÉRIO DO MEIO AMBIENTE - MMA. **Government publicizes deforestation in Cerrado**. 2018. Available from: <http://redd.mma.gov.br/en/component/content/article/160-central-content/top-news/1021-government-publicizes-deforestation-in-cerrado>. Access in: 20 Mar. 2021. 2

_____. **Desenvolvimento de sistemas de prevenção de incêndios florestais e monitoramento da cobertura vegetal no Cerrado brasileiro**. 2021. Available from: <http://fip.mma.gov.br/projeto-fm/>. Access in: 10 Apr. 2021. 2

_____. **Programa de investimento florestal no Brasil**. 2021. Available from: <http://fip.mma.gov.br/>. Access in: 10 Apr. 2021. 2

BRITO, A.; VALERIANO, D. D. M.; FERRI, C.; SCOLASTRICI, A.; SESTINI, M. **Metodologia da detecção do desmatamento no bioma Cerrado: mapeamento de áreas antropizadas com imagens de média resolução espacial**. Sao José dos Campos: Instituto Nacional de Pesquisas Espaciais (INPE), 2018. 18 p. Available from: <http://www.dpi.inpe.br/fipcerrado/report_funcate_metodologia_mapeamento_bioma_cerrado.pdf>. 1, 2, 3, 9, 10, 11, 35

BROOKE, B.; LYMBURNER, L.; LEWIS, A. Coastal dynamics of Northern Australia – insights from the Landsat Data Cube. **Remote Sensing Applications: Society and Environment**, v. 8, p. 94–98, nov 2017. ISSN 23529385. 15

BUENO, I.; ACERBI, F. J.; SILVEIRA, E.; MELLO, J.; CARVALHO, L.; GOMIDE, L.; WITHEY, K.; SCOLFORO, J. Object-based change detection in the Cerrado biome using Landsat time series. **Remote Sensing**, v. 11, n. 5, p. 24–31, 2019. 58

CASTRO FILHO, H. C. d.; CARVALHO JÚNIOR, O. A. d.; CARVALHO, O. L. F. d.; BEM, P. P. d.; MOURA, R. d. S. d.; ALBUQUERQUE, A. O. d.; SILVA, C. R.; FERREIRA, P. H. G.; GUIMARÃES, R. F.; GOMES, R. A. T. Rice crop detection using LSTM, Bi-LSTM, and machine learning models from Sentinel-1 time series. **Remote Sensing**, v. 12, n. 16, p. 2655, aug 2020. ISSN 2072-4292. 22

CHASTAIN, R.; HOUSMAN, I.; GOLDSTEIN, J.; FINCO, M.; TENNESON, K. Empirical cross sensor comparison of Sentinel-2A and 2B MSI, Landsat-8 OLI, and Landsat-7 ETM+ top of atmosphere spectral characteristics over the conterminous United States. **Remote Sensing of Environment**, v. 221, p. 274–285, feb 2019. ISSN 00344257. 15

CHAVES, M. E. D.; PICOLI, M. C. A.; SANCHES, I. D. Recent applications of Landsat 8/OLI and Sentinel-2/MSI for land use and land cover mapping: A systematic review. **Remote Sensing**, v. 12, n. 18, p. 3062, sep 2020. ISSN 2072-4292. 15

DOZIER, J.; PAINTER, T. H.; RITTGER, K.; FREW, J. E. Time–space continuity of daily maps of fractional snow cover and albedo from MODIS. **Advances in Water Resources**, v. 31, n. 11, p. 1515–1526, nov 2008. Available from: <https://doi.org/10.1016/j.advwatres.2008.08.011>. 38

DRUSCH, M.; DEL BELLO, U.; CARLIER, S.; COLIN, O.; FERNANDEZ, V.; GASCON, F.; HOERSCH, B.; ISOLA, C.; LABERINTI, P.; MARTIMORT, P.;

MEYGRET, A.; SPOTO, F.; SY, O.; MARCHESE, F.; BARGELLINI, P. Sentinel-2: ESA's optical high-resolution mission for GMES operational services. **Remote Sensing of Environment**, v. 120, p. 25–36, 2012. ISSN 00344257. 14

DUTTA, D.; CHEN, G.; CHEN, C.; GAGNÉ, S. A.; LI, C.; ROGERS, C.; MATTHEWS, C. Detecting plant invasion in urban parks with aerial image time series and residual neural network. **Remote Sensing**, v. 12, n. 21, p. 3493, oct 2020. ISSN 2072-4292. 3

EHLERS, R. S. **Análise de Séries Temporais**. 2009. Available from: <https://sites.icmc.usp.br/ehlers/stemp/>. Access in: 27 Feb. 2021. 12

EMPRESA BRASILEIRA DE PESQUISA AGROPECUÁRIA - EMBRAPA. **Bioma Cerrado**. 2021. Available from: <https://www.embrapa.br/cerrados/colecao-entomologica/bioma-cerrado>. Access in: 20 Feb. 2021. 6

ESPÍRITO-SANTO, M. M.; LEITE, M. E.; SILVA, J. O.; BARBOSA, R. S.; ROCHA, A. M.; ANAYA, F. C.; DUPIN, M. G. V. Understanding patterns of land-cover change in the Brazilian Cerrado from 2000 to 2015. **Philosophical Transactions of the Royal Society B: Biological Sciences**, v. 371, n. 1703, p. 20150435, 2016. ISSN 0962-8436. 8

EUROPEAN SPACE AGENCY - ESA. **Sentinel-2 – overview**. 2021. Available from: <https://earth.esa.int/web/sentinel/missions/sentinel-2/overview>. Access in: 10 Feb. 2021. 14

_____. **Sentinel-2 radiometric resolutions**. 2021. Available from: <https://earth.esa.int/web/sentinel/user-guides/sentinel-2-msi/resolutions/radiometric>. Access in: 10 Feb. 2021. 14, 15, 34, 36, 58

FARR, T. G.; ROSEN, P. A.; CARO, E.; CRIPPEN, R.; DUREN, R.; HENSLEY, S.; KOBRICK, M.; PALLER, M.; RODRIGUEZ, E.; ROTH, L.; SEAL, D.; SHAFFER, S.; SHIMADA, J.; UMLAND, J.; WERNER, M.; OSKIN, M.; BURBANK, D.; ALSDORF, D. The Shuttle Radar Topography Mission. **Reviews of Geophysics**, v. 45, n. 2, p. RG2004, may 2007. ISSN 8755-1209. 34, 39

FERREIRA, K. R.; QUEIROZ, G. R.; CAMARA, G.; SOUZA, R. C. M.; VINHAS, L.; MARUJO, R. F. B.; SIMOES, R. E. O.; NORONHA, C. A. F.; COSTA, R. W.; ARCANJO, J. S.; GOMES, V. C. F.; ZAGLIA, M. C. Using

remote sensing images and cloud services on AWS to improve land use and cover monitoring. In: IEEE LATIN AMERICAN GRSS ISPRS REMOTE SENSING CONFERENCE (LAGIRS), 2020, Santiago, Chile. **Proceedings...** Santiago, Chile: IEEE, 2020. v. 1, p. 558–562. 17

FERREIRA, K. R.; QUEIROZ, G. R.; VINHAS, L.; MARUJO, R. F. B.; SIMOES, R. E. O.; PICOLI, M. C. A.; CAMARA, G.; CARTAXO, R.; GOMES, V. C. F.; SANTOS, L. A.; SANCHEZ, A. H.; ARCANJO, J. S.; FRONZA, J. G.; NORONHA, C. A.; COSTA, R. W.; ZAGLIA, M. C.; ZIOTI, F.; KORTING, T. S.; SOARES, A. R.; CHAVES, M. E. D.; FONSECA, L. M. G. Earth observation data cubes for Brazil: Requirements, methodology and products. **Remote Sensing**, v. 12, n. 24, p. 4033, dec 2020. ISSN 2072-4292. 15, 16, 17, 18, 36, 59

FERREIRA, L.; YOSHIOKA, H.; HUETE, A.; SANO, E. Seasonal landscape and spectral vegetation index dynamics in the Brazilian Cerrado: an analysis within the Large-Scale Biosphere–Atmosphere Experiment in Amazônia (LBA). **Remote Sensing of Environment**, v. 87, n. 4, p. 534–550, 2003. ISSN 0034-4257. 3, 6

FERREIRA, N. C.; FERREIRA, L. G.; HUETE, A. R.; FERREIRA, M. E. An operational deforestation mapping system using MODIS data and spatial context analysis. **International Journal of Remote Sensing**, Informa UK Limited, v. 28, n. 1, p. 47–62, jan 2007. 1

FONSECA, L. M.; KÖRTING, T. S.; BENDINI, H. d. N.; GIROLAMO-NETO, C. D.; NEVES, A. K.; SOARES, A. R.; TAQUARY, E. C.; MARETTO, R. V. Pattern recognition and remote sensing techniques applied to land use and land cover mapping in the Brazilian Savannah. **Pattern Recognition Letters**, v. 148, p. 54–60, aug 2021. ISSN 01678655. 9

FOODY, G. M. Classification accuracy comparison: hypothesis tests and the use of confidence intervals in evaluations of difference, equivalence and non-inferiority. **Remote Sensing of Environment**, v. 113, n. 8, p. 1658–1663, 2009. ISSN 00344257. 26

_____. Assessing the accuracy of land cover change with imperfect ground reference data. **Remote Sensing of Environment**, v. 114, n. 10, p. 2271–2285, oct 2010. ISSN 00344257. 24, 25, 26, 27

GARCIA, A. S.; BALLESTER, M. V. R. Land cover and land use changes in a Brazilian Cerrado landscape: drivers, processes, and patterns. **Journal of Land Use Science**, v. 11, n. 5, p. 538–559, 2016. ISSN 1747-423X. 8

GIULIANI, G.; CHATENOUX, B.; De Bono, A.; RODILA, D.; RICHARD, J.-P.; ALLENBACH, K.; DAO, H.; PEDUZZI, P. Building an Earth Observations Data Cube: lessons learned from the Swiss Data Cube (SDC) on generating Analysis Ready Data (ARD). **Big Earth Data**, v. 1, n. 1-2, p. 100–117, dec 2017. ISSN 2096-4471. 15, 16

GOODFELLOW, I.; BENGIO, Y.; COURVILLE, A. **Deep Learning**. Cambridge, EUA: MIT Press, 2016. Available from: <http://www.deeplearningbook.org>. 19, 20, 21

GRAVES, A.; LIWICKI, M.; FERNÁNDEZ, S.; BERTOLAMI, R.; BUNKE, H.; SCHMIDHUBER, J. A novel connectionist system for unconstrained handwriting recognition. **IEEE Transactions on Pattern Analysis and Machine Intelligence**, v. 31, n. 5, p. 855–868, 2008. 21

GRAVES, A.; MOHAMED, A.-R.; HINTON, G. Speech recognition with deep recurrent neural networks. In: INTERNATIONAL CONFERENCE ON ACOUSTICS, SPEECH AND SIGNAL PROCESSING, 38., 2013, Vancouver, Canada. **Proceedings...** Vancouver, Canada: IEEE, 2013. p. 6645–6649. 3, 20

HOCHREITER, S.; SCHMIDHUBER, J. Long short-term memory. **Neural computation**, v. 9, n. 8, p. 1735–1780, 1997. 3, 21, 22

HOU, J.; HUANG, C.; ZHANG, Y.; GUO, J.; GU, J. Gap-filling of MODIS fractional snow cover products via non-local spatio-temporal filtering based on machine learning techniques. **Remote Sensing**, v. 11, n. 1, p. 90, jan 2019. Available from: <https://doi.org/10.3390/rs11010090>. 12, 38

INSTITUTO BRASILEIRO DE GEOGRAFIA E ESTATÍSTICA - IBGE. **Brasil em Síntese**. 2021. Available from: <https://brasilemsintese.ibge.gov.br/territorio.html>. Access in: 10 Jan. 2021. 1, 5, 8

INSTITUTO NACIONAL DE PESQUISAS ESPACIAIS - INPE. **PRODES – incremento anual de área desmatada no Cerrado Brasileiro**. 2020. Available from: <http://www.obt.inpe.br/cerrado>. Access in: 26 Mar. 2021. 1, 3, 7, 8, 9, 11, 31, 34

_____. **DETER**. 2021. Available from: <http://www.obt.inpe.br/OBT/assuntos/programas/amazonia/deter/deter>. Access in: 20 Mar. 2021. 2

_____. **PRODES - Amazônia**. 2021. Available from: <http://www.obt.inpe.br/OBT/assuntos/programas/amazonia/prodes>. Access in: 20 Mar. 2021. 9

INTERDONATO, R.; IENCO, D.; GAETANO, R.; OSE, K. DuPLO: A dual view point deep learning architecture for time series classification. **ISPRS Journal of Photogrammetry and Remote Sensing**, v. 149, p. 91–104, 2019. ISSN 0924-2716. 3

ISAIENKOV, K.; YUSHCHUK, M.; KHRAMTSOV, V.; SELIVERSTOV, O. Deep learning for regular change detection in Ukrainian forest ecosystem with Sentinel-2. **IEEE Journal of Selected Topics in Applied Earth Observations and Remote Sensing**, v. 14, p. 364–376, 2021. 15

JIANG, L.; ZHOU, Z.; LEUNG, T.; LI, L.-J.; FEI-FEI, L. MentorNet: Learning data-driven curriculum for very deep neural networks on corrupted labels. **35th International Conference on Machine Learning, ICML 2018**, v. 5, p. 3601–3620, dec 2017. Available from: <http://arxiv.org/abs/1712.05055>. 20, 57, 59

KATTENBORN, T.; LEITLOFF, J.; SCHIEFER, F.; HINZ, S. Review on Convolutional Neural Networks (CNN) in vegetation remote sensing. **ISPRS Journal of Photogrammetry and Remote Sensing**, v. 173, n. November 2020, p. 24–49, mar 2021. ISSN 09242716. 19, 23, 24

KEYS, R. Cubic convolution interpolation for digital image processing. **IEEE Transactions on Acoustics, Speech, and Signal Processing**, v. 29, n. 6, p. 1153–1160, 1981. 39

KUENZER, C.; DECH, S.; WAGNER, W. **Remote Sensing Time Series**. Cham: Springer International Publishing, 2015. 441 p. (Remote Sensing and Digital Image Processing, v. 22). ISSN 22151842. 11

LECUN, Y.; BENGIO, Y.; HINTON, G. Deep learning. **Nature**, v. 521, p. 436–444, may 2015. ISSN 0028-0836. 4, 18, 19

LECUN, Y.; HAFFNER, P.; BOTTOU, L.; BENGIO, Y. Object recognition with gradient-based learning. In: FORSYTH, D. A.; MUNDY, J. L.; GESÚ, V. di; CIPOLLA, R. (Ed.). **Shape, contour and grouping in computer vision**. Berlim, Alemanha: Springer, 1999. p. 319–345. 23

LEWIS, A.; OLIVER, S.; LYMBURNER, L.; EVANS, B.; WYBORN, L.; MUELLER, N.; RAEVKSI, G.; HOOKE, J.; WOODCOCK, R.; SIXSMITH, J.; WU, W.; TAN, P.; LI, F.; KILLOUGH, B.; MINCHIN, S.; ROBERTS, D.; AYERS, D.; BALA, B.; DWYER, J.; DEKKER, A.; DHU, T.; HICKS, A.; IP, A.; PURSS, M.; RICHARDS, C.; SAGAR, S.; TRENHAM, C.; WANG, P.; WANG, L.-W. The Australian geoscience data cube — foundations and lessons learned. **Remote Sensing of Environment**, v. 202, p. 276–292, dec 2017. ISSN 00344257. 12, 15

LI, S. **Simple introduction about hourglass-like model**. 2017. Available from: <https://medium.com/@sunnerli/simple-introduction-about-hourglass-like-model-11ee7c30138>. Access in: 20 Jan. 2021. 24

LI, W.; HSU, C. Automated terrain feature identification from remote sensing imagery: a deep learning approach. **International Journal of Geographical Information Science**, v. 34, n. 4, p. 637–660, 2020. 3

LI, Y.; ZHANG, Y.; ZHU, Z. Error-Tolerant Deep Learning for Remote Sensing Image Scene Classification. **IEEE Transactions on Cybernetics**, v. 51, n. 4, p. 1756–1768, apr 2021. ISSN 2168-2267. Available from: <https://ieeexplore.ieee.org/document/9093113/>. 20, 57, 59

LIMA, T. A.; BEUCHLE, R.; LANGNER, A.; GRECCHI, R. C.; GRIESS, V. C.; ACHARD, F. Comparing Sentinel-2 MSI and Landsat 8 OLI imagery for monitoring selective logging in the Brazilian Amazon. **Remote Sensing**, v. 11, n. 8, p. 961, apr 2019. ISSN 2072-4292. 58

LOHR, S. L. **Sampling: Design and Analysis**. 2.ed. ed. Boston - MA, USA: Brooks/Cole, 2009. 596 p. 25, 46

LOVELAND, T. R.; IRONS, J. R. Landsat 8: The plans, the reality, and the legacy. **Remote Sensing of Environment**, v. 185, p. 1–6, 2016. ISSN 00344257. 13

LUNETTA, R. S.; CONGALTON, R. G.; FENSTERMAKER, L. K.; JENSEN, J. R.; MCGWIRE, K. C.; TINNEY, L. R. Remote sensing and geographic information system data integration: Error sources and research issues. **Photogrammetric Engineering & Remote Sensing**, v. 57, n. 6, p. 677–687, 1991. ISSN 0099-1112. 3

MA, L.; LIU, Y.; ZHANG, X.; YE, Y.; YIN, G.; JOHNSON, B. A. Deep learning in remote sensing applications: A meta-analysis and review. **ISPRS Journal of**

Photogrammetry and Remote Sensing, v. 152, n. 14, p. 166–177, jun 2019. ISSN 09242716. 3, 18, 19, 20

MANDANICI, E.; BITELLI, G. Preliminary comparison of Sentinel-2 and Landsat 8 imagery for a combined use. **Remote Sensing**, v. 8, n. 12, p. 1014, 2016. 15

MAPBIOMAS. **Coleção 4.0 da Série Anual de Mapas de Cobertura e Uso de Solo do Brasil**. 2021. Available from: <http://plataforma.mapbiomas.org>. Access in: 10 Jan. 2021. 3, 9, 30

MARETTO, R. V. **Automating land cover change detection: a deep learning based approach to map deforested areas**. 80 p. PhD Thesis (PhD) — Instituto Nacional de Pesquisas Espaciais (INPE), São José dos Campos, mar 2020. Available from: <http://urlib.net/rep/8JMKD3MGP3W34R/42L55PP>. Access in: 28 Mar. 2021. 60

MARETTO, R. V.; FONSECA, L. M. G.; JACOBS, N.; KORTING, T. S.; BENDINI, H. N.; PARENTE, L. L. Spatio-temporal deep learning approach to map deforestation in Amazon Rainforest. **IEEE Geoscience and Remote Sensing Letters**, v. 18, n. 5, p. 771–775, 2020. ISSN 1545-598X. 3

MARETTO, R. V.; KÖRTING, T. S.; FONSECA, L. M. G. An extensible and easy-to-use toolbox for deep learning based analysis of remote sensing images. In: IEEE INTERNATIONAL GEOSCIENCE AND REMOTE SENSING SYMPOSIUM, 39., 2019, Yokohama, Japan. **Proceedings...** Yokohama, Japan: IEEE, 2019. Available from: <https://github.com/rvmaretto/deepgeo>. 43

MARMANIS, D.; WEGNER, J. D.; GALLIANI, S.; SCHINDLER, K.; DATCU, M.; STILLA, U. Semantic segmentation of aerial images with an ensemble of CNNs. **ISPRS Annals of Photogrammetry, Remote Sensing and Spatial Information Sciences**, III-3, n. July, p. 473–480, 2016. 23

MARTINEZ, J. A. C.; ROSA, L. E. C. L.; FEITOSA, R. Q.; SANCHES, I. D.; HAPP, P. N. Fully convolutional recurrent networks for multidate crop recognition from multitemporal image sequences. **ISPRS Journal of Photogrammetry and Remote Sensing**, Elsevier BV, v. 171, p. 188–201, 2021. Available from: <https://doi.org/10.1016/j.isprsjprs.2020.11.007>. 4

MARUJO, R. F. B.; FONSECA, L. M. G.; KÖRTING, T. S.; BENDINI, H. N. A multi-scale segmentation approach to filling gaps in Landsat ETM+ SLC-off images through pixel weighting. **ISPRS - International Archives of the**

Photogrammetry, Remote Sensing and Spatial Information Sciences, n. 23, p. 79–84, feb 2020. ISSN 2194-9034. Available from: <https://www.int-arch-photogramm-remote-sens-spatial-inf-sci.net/XLII-3-W11/79/2020/>. 12

MATOSAK, B. M.; MARETTO, R. V.; KöRTING, T. S.; ADAMI, M.; FONSECA, L. M. G. Mapping deforested areas in the Cerrado biome through recurrent neural networks. In: IEEE INTERNATIONAL GEOSCIENCE AND REMOTE SENSING SYMPOSIUM, 40., 2020, Waikoloa, HI, USA. **Proceedings...** Waikoloa, HI, USA: IEEE, 2020. v. 1, n. 1389, p. 1389–1392. 12, 17, 22

MAURANO, L. E. P.; ALMEIDA, C. A. d.; MEIRA, M. B. Monitoramento do desmatamento no Cerrado Brasileiro por satélite – projeto monitoramento do Cerrado. In: SIMPÓSIO BRASILEIRO DE SENSORIAMENTO REMOTO, 19., 2019, Santos - SP, Brasil. **Proceedings...** São José dos Campos: INPE, 2019. p. 191–194. 2

MAURANO, L. E. P.; ESCADA, M. I. S.; RENNO, C. D. Padrões espaciais de desmatamento e a estimativa da exatidão dos mapas do PRODES para Amazônia Legal brasileira. **Ciência Florestal**, v. 29, n. 4, p. 1763, dec 2019. 1, 57

MITTERMEIER, R. A.; TURNER, W. R.; LARSEN, F. W.; BROOKS, T. M.; GASCON, C. Global biodiversity conservation: the critical role of hotspots. In: ZACHOS, F. E.; HABEL, J. C. (Ed.). **Biodiversity hotspots**. [S.l.]: Springer, 2011. p. 3–22. 1

MOHAJERANI, S.; KRAMMER, T. A.; SAEEDI, P. A cloud detection algorithm for remote sensing images using fully convolutional neural networks. **CoRR**, abs/1810.05782, 2018. 24

MÜLLER, H.; RUFIN, P.; GRIFFITHS, P.; SIQUEIRA, A. J. B.; HOSTERT, P. Mining dense Landsat time series for separating cropland and pasture in a heterogeneous Brazilian savanna landscape. **Remote Sensing of Environment**, v. 156, p. 490–499, jan 2015. ISSN 00344257. 3, 7, 12, 58, 63

NATIONAL AERONAUTICS AND SPACE ADMINISTRATION - NASA. **Landsat 8 bands**. 2013. Available from: <https://landsat.gsfc.nasa.gov/landsat-8/landsat-8-bands/>. Access in: 10 Feb. 2021. 14, 34, 36, 58

NEVES, A. K.; KÖRTING, T. S.; FONSECA, L. M. G.; GIROLAMO NETO, C. D.; WITTICH, D.; COSTA, G. A. O. P.; HEIPKE, C. Semantic segmentation of Brazilian savanna vegetation using high spatial resolution satellite data and U-Net. **ISPRS Annals of Photogrammetry, Remote Sensing and Spatial Information Sciences**, v. 3, n. 3, p. 505–511, aug 2020. ISSN 2194-9050. 7

NGUYEN, T. H.; JONES, S. D.; SOTO-BERELOV, M.; HAYWOOD, A.; HISLOP, S. A spatial and temporal analysis of forest dynamics using Landsat time-series. **Remote Sensing of Environment**, v. 217, p. 461–475, 2018. ISSN 00344257. 15

OLAH, C. **Understanding LSTM networks**. 2015. Available from: <https://colah.github.io/posts/2015-08-Understanding-LSTMs/>. Access in: 20 Jan. 2021. 20, 21, 22

OLIVEIRA, L. M. T.; FRANÇA, G. B.; NICÁCIO, R. M.; ANTUNES, M. A. H.; COSTA, T. C. C.; TORRES, A. R.; FRANÇA, J. R. A. A study of the El Niño-southern oscillation influence on vegetation indices in Brazil using time series analysis from 1995 to 1999. **International Journal of Remote Sensing**, v. 31, n. 2, p. 423–437, jan. 2010. 59

OLOFSSON, P.; FOODY, G. M.; HEROLD, M.; STEHMAN, S. V.; WOODCOCK, C. E.; WULDER, M. A. Good practices for estimating area and assessing accuracy of land change. **Remote Sensing of Environment**, v. 148, p. 42–57, may 2014. ISSN 00344257. 24, 25, 27, 46, 51

PAGEOT, Y.; BAUP, F.; INGLADA, J.; BAGHDADI, N.; DEMAREZ, V. Detection of irrigated and rainfed crops in temperate areas using Sentinel-1 and Sentinel-2 time series. **Remote Sensing**, v. 12, n. 18, p. 3044, sep 2020. ISSN 20724292. 15

PARENTE, L.; NOGUEIRA, S.; BAUMANN, L.; ALMEIDA, C.; MAURANO, L.; AFFONSO, A. G.; FERREIRA, L. Quality assessment of the PRODES Cerrado deforestation data. **Remote Sensing Applications: Society and Environment**, v. 21, 2021. ISSN 23529385. 3, 46, 57, 60

PARENTE, L.; TAQUARY, E.; SILVA, A. P.; SOUZA, C.; FERREIRA, L. Next generation mapping: Combining deep learning, cloud computing, and big remote sensing data. **Remote Sensing**, v. 11, n. 23, p. 2881, dec 2019. ISSN 2072-4292. 3, 4, 22

PASCANU, R.; MIKOLOV, T.; BENGIO, Y. On the difficulty of training recurrent neural networks. In: INTERNATIONAL CONFERENCE ON MACHINE LEARNING, 30., 2013, Atlanta, EUA. **Proceedings...** Atlanta, EUA: PMLR, 2013. p. 1310–1318. 21

PETITJEAN, F.; INGLADA, J.; GARÇARSKI, P. Satellite image time series analysis under time warping. **IEEE Transactions on Geoscience and Remote Sensing**, v. 50, n. 8, p. 3081–3095, 2012. ISSN 01962892. 12

PETROVSKA, B.; ZDRAVEVSKI, E.; LAMESKI, P.; CORIZZO, R.; ŠTAJDUHAR, I.; LERGA, J. Deep learning for feature extraction in remote sensing: A case-study of aerial scene classification. **Sensors**, v. 20, n. 14, p. 3906, Jul 2020. ISSN 1424-8220. 3

PICOLI, M. C. A.; SIMOES, R.; CHAVES, M.; SANTOS, L. A.; SANCHEZ, A.; SOARES, A.; SANCHES, I. D.; FERREIRA, K. R.; QUEIROZ, G. R. CBERS data cube: a powerful technology for mapping and monitoring Brazilian biomes. **ISPRS Annals of Photogrammetry, Remote Sensing and Spatial Information Sciences**, v. 3, p. 533–539, 2020. 17

QIU, S.; ZHU, Z.; HE, B. Fmask 4.0: improved cloud and cloud shadow detection in Landsats 4–8 and Sentinel-2 imagery. **Remote Sensing of Environment**, v. 231, p. 111205, 2019. ISSN 0034-4257. 17, 38

RADA, N. Assessing Brazil's cerrado agricultural miracle. **Food Policy**, v. 38, p. 146–155, Feb 2013. 1

RAKHLIN, A.; DAVYDOW, A.; NIKOLENKO, S. Land cover classification from satellite imagery with U-Net and Lovász-Softmax loss. In: CVF CONFERENCE ON COMPUTER VISION AND PATTERN RECOGNITION WORKSHOPS, 29., 2018, Salt Lake City, EUA. **Proceedings...** Salt Lake City, EUA: IEEE, 2018. p. 262–266. 24

RENDÓN, E.; ALEJO, R.; CASTORENA, C.; ISIDRO-ORTEGA, F. J.; GRANDA-GUTIÉRREZ, E. E. Data sampling methods to deal with the big data multi-class imbalance problem. **Applied Sciences (Switzerland)**, v. 10, n. 4, 2020. ISSN 20763417. 20, 45, 59

REYNOLDS, J.; WESSON, K.; DESBIEZ, A.; OCHOA-QUINTERO, J.; LEIMGRUBER, P. Using remote sensing and Random Forest to assess the conservation status of critical Cerrado habitats in Mato Grosso do Sul, Brazil. **Land**, v. 5, n. 2, p. 12, may 2016. ISSN 2073-445X. 3, 7, 57

RIBEIRO, J. F.; WALTER, B. M. T. As principais fitofisionomias do bioma Cerrado. In: SANO, S. M.; ALMEIDA, S. P.; RIBEIRO, J. F. (Ed.). **Cerrado: ecologia e flora**. Brasília: EMBRAPA, 2008. p. 152–212. 6, 7

ROCHA, G. F.; FERREIRA, L. G.; FERREIRA, N. C.; FERREIRA, M. E. Detecção de desmatamentos no bioma Cerrado entre 2002 e 2009: Padrões, tendências e impactos. **Revista Brasileira de Cartografia**, v. 63, n. 3, mar 2012. 1, 8, 30

RONNEBERGER, O.; FISCHER, P.; BROX, T. U-Net: Convolutional networks for biomedical image segmentation. In: MEDICAL IMAGE COMPUTING AND COMPUTER-ASSISTED INTERVENTION, 18., 2015, Munich, Germany. **Proceedings...** Munich, Germany: Springer, 2015. p. 234–241. 3, 23

RUSSWURM, M.; KÖRNER, M. Self-attention for raw optical Satellite Time Series Classification. **ISPRS Journal of Photogrammetry and Remote Sensing**, v. 169, p. 421–435, nov 2020. ISSN 09242716. 3

SANO, E. E.; RODRIGUES, A. A.; MARTINS, E. S.; BETTIOL, G. M.; BUSTAMANTE, M. M.; BEZERRA, A. S.; COUTO, A. F.; VASCONCELOS, V.; SCHÜLER, J.; BOLFE, E. L. Cerrado ecoregions: a spatial framework to assess and prioritize Brazilian savanna environmental diversity for conservation. **Journal of Environmental Management**, v. 232, p. 818–828, 2019. ISSN 03014797. xv, 1, 5, 6, 30, 57, 65

SANO, E. E.; ROSA, R.; BRITO, J. L.; FERREIRA, L. G. Land cover mapping of the tropical savanna region in Brazil. **Environmental Monitoring and Assessment**, v. 166, n. 1-4, p. 113–124, 2010. ISSN 01676369. 3, 7, 9, 63

SANO, E. E.; ROSA, R.; BRITO, J. L. S.; FERREIRA, L. G. Mapeamento semidetalhado do uso da terra do bioma Cerrado. **Pesquisa Agropecuária Brasileira**, v. 43, n. 1, p. 153–156, jan 2008. 1

SCARAMUZZA, C. A. d. M.; SANO, E. E.; ADAMI, M.; BOLFE, E. L.; COUTINHO, A. C.; ESQUERDO, J. C. D. M.; MAURANO, L. E. P.; NARVAES, I. S.; OLIVEIRA FILHO, F. J. B.; ROSA, R.; SILVA, E. B.; VALERIANO, D. M.; VICTORIA, D. C.; BAYMA, A. P.; OLIVEIRA, G. H.; GUSTAVO, B.-S. Land-use and land-cover mapping of the Brazilian Cerrado based mainly on Landsat-8 satellite images. **Revista Brasileira de Cartografia**, v. 69, n. 6, p. 1041–1051, 2017. 1, 9

SCHWIEDER, M.; LEITÃO, P. J.; BUSTAMANTE, M. M. d. C.; FERREIRA, L. G.; RABE, A.; HOSTERT, P. Mapping Brazilian savanna vegetation gradients with Landsat time series. **International Journal of Applied Earth Observation and Geoinformation**, v. 52, p. 361–370, oct 2016. ISSN 03032434. 58

SHI, W.; ZHANG, M.; ZHANG, R.; CHEN, S.; ZHAN, Z. Change detection based on artificial intelligence: state-of-the-art and challenges. **Remote Sensing**, v. 12, n. 10, p. 1688, may 2020. ISSN 2072-4292. 18, 59

SHI, X.; CHEN, Z.; WANG, H.; YEUNG, D.-Y.; WONG, W.-K.; WOO, W.-c. Convolutional LSTM network: A machine learning approach for precipitation nowcasting. In: **Advances in neural information processing systems**. [S.l.: s.n.], 2015. p. 802–810. 4

SHIMABUKURO, Y. E.; SANTOS, J. R. dos; FORMAGGIO, A. R.; DUARTE, V.; RUDORFF, B. F. T. The Brazilian Amazon monitoring program: PRODES and DETER projects. In: ACHARD, F.; HANSEN, M. C. (Ed.). **Global forest monitoring from earth observation**. Boca Raton, Florida - USA: CRC Press, 2012. p. 153–170. 2

SILVA, M. A. O. da; ANDRADE, A. C. de. Geração de imagens de reflectância de um ponto de vista geométrico. **Revista Brasileira de Geomática**, v. 1, n. 1, p. 23, mar 2013. ISSN 2317-4285. 17

SIQUEIRA, A.; LEWIS, A.; THANKAPPAN, M.; SZANTOI, Z.; GORYL, P.; LABAHN, S.; ROSS, J.; HOSFORD, S.; MECKLENBURG, S.; TADONO, T.; ROSENQVIST, A.; LACEY, J. CEOS analysis ready data for land – an overview on the current and future work. In: IEEE INTERNATIONAL GEOSCIENCE AND REMOTE SENSING SYMPOSIUM, 39., 2019, Yokohama, Japan. **Proceedings...** Yokohama, Japan: IEEE, 2019. p. 5536–5537. 15

SOARES, A.; KöRTING, T.; FONSECA, L.; BENDINI, H. Simple nonlinear iterative temporal clustering. **IEEE Transactions on Geoscience and Remote Sensing**, p. 1–11, 2020. 17

SOARES-FILHO, B.; RAJÃO, R.; MERRY, F.; RODRIGUES, H.; DAVIS, J.; LIMA, L.; MACEDO, M.; COE, M.; CARNEIRO, A.; SANTIAGO, L. Brazil's market for trading forest certificates. **PLoS One**, v. 11, n. 4, 2016. 1

SOUZA, A.; MONTEIRO, A. M. V.; RENNó, C. D.; ALMEIDA, C. A.; VALERIANO, D. de M.; MORELLI, F.; VINHAS, L.; MAURANO, L. E. P.;

ADAMI, M.; ESCADA, M. I. S.; MOTTA, M. da; AMARAL, S. **Metodologia utilizada nos projetos PRODES e DETER**. Sao José dos Campos: Instituto Nacional de Pesquisas Espaciais (INPE), 2019. 33 p. Available from: <http://www.obt.inpe.br/OBT/assuntos/programas/amazonia/prodes/pdfs/Metodologia_Prodes_Deter_revisada.pdf>. 10

SPERA, S. Agricultural intensification can preserve the Brazilian Cerrado: applying lessons from Mato Grosso and Goiás to Brazil's last agricultural frontier. **Tropical Conservation Science**, v. 10, p. 194008291772066, jan 2017. ISSN 1940-0829. 1

STRASSBURG, B. B. N.; BROOKS, T.; FELTRAN-BARBIERI, R.; IRIBARREM, A.; CROUZEILLES, R.; LOYOLA, R.; LATAWIEC, A. E.; OLIVEIRA FILHO, F. J. B.; SCARAMUZZA, C. A. d. M.; SCARANO, F. R.; SOARES-FILHO, B.; BALMFORD, A. Moment of truth for the Cerrado hotspot. **Nature Ecology & Evolution**, v. 1, n. 4, p. 0099, apr 2017. ISSN 2397-334X. 1, 6, 7

TAQUARY, E. C. **Deep Learning Para Identificação Precisa de Desmatamentos Através do Uso de Imagens Satelitárias de Alta Resolução**. 64 p. Dissertation (Master in Computer Science) — Universidade Federal de Goiás (UFG), Goiânia, 2019. 3, 22, 23, 60

TERRABRASILIS. **Incremento de desmatamento – Cerrado**. 2020. Available from: <http://terrabrasilis.dpi.inpe.br/app/dashboard/deforestation/biomes/cerrado/increments>. Access in: 26 Mar. 2021. 2, 11

TOBLER, W. R. A computer movie simulating urban growth in the detroit region. **Economic Geography**, v. 46, n. sup1, p. 234–240, 1970. 22

TORRES, D. L.; FEITOSA, R. Q.; HAPP, P. N.; ROSA, L. E. C. L.; JUNIOR, J. M.; MARTINS, J.; BRESSAN, P. O.; GONÇALVES, W. N.; LIESENBERG, V. Applying fully convolutional architectures for semantic segmentation of a single tree species in urban environment on high resolution UAV optical imagery. **Sensors**, v. 20, n. 2, p. 563, Jan 2020. ISSN 1424-8220. 4

UNITED STATES GEOLOGICAL SURVEY - USGS. **Landsat 8 data users handbook**. USGS, 2019. 106 p. Available from: <https://prd-wret.s3-us-west-2.amazonaws.com/assets/palladium/production/atoms/files/LSDS-1574_L8_Data_Users_Handbook-v5.0.pdf>. Access in: 10 Mar. 2021. 14

VERMOTE, E.; JUSTICE, C.; CLAVERIE, M.; FRANCH, B. Preliminary analysis of the performance of the Landsat 8/OLI land surface reflectance product. **Remote Sensing of Environment**, 2016. ISSN 00344257. 17

VUOLO, F.; NG, W. T.; ATZBERGER, C. Smoothing and gap-filling of high resolution multi-spectral time series: example of Landsat data. **International Journal of Applied Earth Observation and Geoinformation**, v. 57, p. 202–213, 2017. ISSN 1872826X. Available from: <http://dx.doi.org/10.1016/j.jag.2016.12.012>. 12

WAGNER, F. H.; SANCHEZ, A.; TARABALKA, Y.; LOTTE, R. G.; FERREIRA, M. P.; AIDAR, M. P. M.; GLOOR, E.; PHILLIPS, O. L.; ARAGÃO, L. E. O. C. Using the U-Net convolutional network to map forest types and disturbance in the atlantic rainforest with very high resolution images. **Remote Sensing in Ecology and Conservation**, v. 5, n. 4, p. 360–375, 2019. 24

WIRATAMA, W.; LEE, J.; SIM, D. Change detection on multi-spectral images based on feature-level U-Net. **IEEE Access**, v. 8, p. 12279–12289, 2020. ISSN 2169-3536. 24

XU, D.; MA, Y.; YAN, J.; LIU, P.; CHEN, L. Spatial-feature data cube for spatiotemporal remote sensing data processing and analysis. **Computing**, v. 102, n. 6, p. 1447–1461, jun 2020. ISSN 0010-485X. 15

XU, J.; ZHU, Y.; ZHONG, R.; LIN, Z.; XU, J.; JIANG, H.; HUANG, J.; LI, H.; LIN, T. DeepCropMapping: A multi-temporal deep learning approach with improved spatial generalizability for dynamic corn and soybean mapping. **Remote Sensing of Environment**, v. 247, p. 111946, sep 2020. ISSN 00344257. 3

XU, Y.; WU, L.; XIE, Z.; CHEN, Z. Building extraction in very high resolution remote sensing imagery using deep learning and guided filters. **Remote Sensing**, v. 10, n. 1, 2018. ISSN 2072-4292. 24

YE, S.; ROGAN, J.; ZHU, Z.; EASTMAN, J. R. A near-real-time approach for monitoring forest disturbance using Landsat time series: stochastic continuous change detection. **Remote Sensing of Environment**, v. 252, p. 112167, jan 2021. Available from: <https://doi.org/10.1016/j.rse.2020.112167>. 12

YESSOU, H.; SUMBUL, G.; DEMIR, B. **A Comparative Study of Deep Learning Loss Functions for Multi-Label Remote Sensing Image Classification**. 2020. 45

ZENG, L.; WARDLOW, B. D.; XIANG, D.; HU, S.; LI, D. A review of vegetation phenological metrics extraction using time-series, multispectral satellite data. **Remote Sensing of Environment**, v. 237, p. 111511, 2020. ISSN 00344257. 3, 12

ZHANG, L.; ZHANG, L.; DU, B. Deep learning for remote sensing data: a technical tutorial on the state of the art. **IEEE Geoscience and Remote Sensing Magazine**, v. 4, n. 2, p. 22–40, jun 2016. ISSN 2168-6831. 23

PUBLICAÇÕES TÉCNICO-CIENTÍFICAS EDITADAS PELO INPE

Teses e Dissertações (TDI)

Teses e Dissertações apresentadas nos Cursos de Pós-Graduação do INPE.

Notas Técnico-Científicas (NTC)

Incluem resultados preliminares de pesquisa, descrição de equipamentos, descrição e ou documentação de programas de computador, descrição de sistemas e experimentos, apresentação de testes, dados, atlas, e documentação de projetos de engenharia.

Propostas e Relatórios de Projetos (PRP)

São propostas de projetos técnico-científicos e relatórios de acompanhamento de projetos, atividades e convênios.

Publicações Seriadas

São os seriados técnico-científicos: boletins, periódicos, anuários e anais de eventos (simpósios e congressos). Constam destas publicações o Internacional Standard Serial Number (ISSN), que é um código único e definitivo para identificação de títulos de seriados.

Pré-publicações (PRE)

Todos os artigos publicados em periódicos, anais e como capítulos de livros.

Manuais Técnicos (MAN)

São publicações de caráter técnico que incluem normas, procedimentos, instruções e orientações.

Relatórios de Pesquisa (RPQ)

Reportam resultados ou progressos de pesquisas tanto de natureza técnica quanto científica, cujo nível seja compatível com o de uma publicação em periódico nacional ou internacional.

Publicações Didáticas (PUD)

Incluem apostilas, notas de aula e manuais didáticos.

Programas de Computador (PDC)

São a seqüência de instruções ou códigos, expressos em uma linguagem de programação compilada ou interpretada, a ser executada por um computador para alcançar um determinado objetivo. Aceitam-se tanto programas fonte quanto os executáveis.